

Die approbierte Originalversion dieser Dissertation ist an der Hauptbibliothek der Technischen Universität Wien aufgestellt (<http://www.ub.tuwien.ac.at>).

The approved original version of this thesis is available at the main library of the Vienna University of Technology (<http://www.ub.tuwien.ac.at/englweb/>).

Diese Dissertation haben begutachtet:

.....



DISSERTATION

Millimeter wave spectroscopy on metamaterials

ausgeführt zum Zwecke der Erlangung des akademischen Grades eines
Doktors der Naturwissenschaften unter der Leitung von

Univ.Prof. Dr.-rer.nat. Andrei Pimenov

E138

Institut für Festkörperphysik

eingereicht an der Technischen Universität Wien
Fakultät für Physik

von

Dipl.-Phys. Sebastian Engelbrecht

Matrikelnummer: 1028773

Greinergasse 22-24/3/4, 1190 Wien

Wien, am 03. Mai 2013

Kurzfassung

In der vorliegenden Arbeit werden die physikalischen Eigenschaften von Metamaterialien untersucht. Die Untersuchungen erfolgen anhand von spektroskopischen Methoden im submillimeter Frequenzbereich. Metamaterialien sind künstlich hergestellte Strukturen, deren elektrodynamischen Eigenschaften nur von ihren geometrischen Eigenschaften bestimmt sind und welche ungewöhnliche Werte annehmen können. Die Untersuchungen erfolgen an Split-Ring Resonatoren (SRR), deren Eigenschaften anhand eines einfachen LC-Schwingkreis Modells verstanden werden können. Die charakteristischen Größen von Metamaterialien sind viel kleiner als die Wellenlänge der verwendeten Strahlung, weswegen ihre Eigenschaften als homogen betrachtet werden können. Für Einschichtsysteme gilt diese Verallgemeinerung jedoch nicht mehr vollständig. In diesem Fall widerspricht die Volumenbeschreibung den experimentellen Ergebnissen. Ein Schichtmodell wird präsentiert, welches sowohl die Transmissions-, als auch die Reflektionsexperimente erklären kann, solange auch die effektive Dicke der Schicht mitberücksichtigt wird.

Um die Gütefaktoren der SRR zu erhöhen, werden Proben aus supraleitendem Niob untersucht. Diese zeigen in der Tat eine signifikant bessere Leistung. Zusätzlich eröffnet die Verwendung von Supraleitern weitere Möglichkeiten für die Abstimmbarkeit der Metamaterialien. So können über externe Parameter, wie magnetische Felder oder die Temperatur, die Resonanzeigenschaften beeinflusst werden. Eine modifizierte Einheitszelle des SRR-Metamaterials wird präsentiert, in welcher die Strahlungsverluste verringert sind. Hierdurch kann der Gütefaktor weiter erhöht werden.

Die Bianisotropie der SRR eröffnet weiterhin die Möglichkeit für neue Anwendungen. Über diese lassen sich zwei Lagen von gegenseitig gedrehten SRR zu chiralen Quasimolekülen koppeln. Diese weisen eine starke optische Aktivität auf, welche die Werte in natürlichen Materialien bei weitem übertrifft. Weiterhin kann die Bianisotropie auch dazu genutzt werden die Elektronen-Spin Resonanz (ESR) in einem Paramagneten über die elektrische Komponente des Lichts anzuregen. Wenn die ESR Frequenz mit der Resonanzfrequenz der Ringe zusammenfällt kann ein starkes Signal gemessen werden, welches über ein einfaches Modell von gekoppelten Oszillatoren erklärt werden kann.

Abstract

In the present work the physical properties of metamaterials are studied by means of phase-sensitive millimeter and submillimeter wave spectroscopy. Metamaterials are artificial materials, whose electrodynamic properties are determined only by design and they can show effects not obtainable in natural materials. A typical realization of a metamaterial is given by the split-ring resonator, whose properties can be understood using a simple LC-circuit model. The characteristic sizes of metamaterials are much smaller than the wavelength of the light, in the range where their interesting properties occur. Therefore they can be treated as a homogeneous material which can be described by the conventional optical parameters, like dielectric permittivity or magnetic permeability. However, for single layers of metamaterials, so called metafilms, the bulk description of metamaterials strongly contradicts the experimental spectra. In contrast, the description within the concept of a layered metamaterial well reproduces the transmittance and reflectance data, as long as the thickness of the metamaterial layer is also considered.

In order to increase the performance of the split-ring structures, samples made of superconducting niobium are studied. It is shown, that using superconductors indeed increase the loss performance of the metamaterial significantly. Furthermore it is shown that this superconducting metamaterials can be tuned by external parameters like magnetic field or temperature. A modified unit cell is presented, in which the radiation losses of the structure are suppressed, which leads to an additional increase in the quality factor of the structure.

The bianisotropy is another property of split-rings that can be used for novel applications. It is shown, that the bianisotropy couples two layers of mutually twisted split-rings to form chiral quasi-molecules. These molecules show an optical activity far exceeding the one obtainable in natural materials. Furthermore, the bianisotropy can also be used to excite the electron-spin resonance (ESR) in a paramagnet using the electric field component of light. When the resonance frequency of the split-rings coincides with the frequency of the ESR a large signal can be observed. A simple model of coupled oscillators can qualitatively explain the observed behaviour.

Acknowledgement

I would like to thank the following people:

Prof. Dr. Andrei Pimenov for giving me the opportunity of doing my PhD in this interesting scientific field and his guidance throughout the years.

Prof. Dr. Jin Biao Bing for the kind production of the superconducting samples and the providing of the simulation data in chapter 4.

Thomas Demarczyk and the electronics workshop in Würzburg for the production of the copper samples.

Andreas Schneider and Max Wunderlich for their contributions to this work.

Alexey Shuvaev for bringing insight in some advanced physical topics, as well as correcting the manuscript of this thesis.

Markus Schiebl and Wlad Dziom for proofreading of the manuscript.

The whole group here in Vienna and also the people from the EP4 in Würzburg for the great atmosphere.

Dr. Christian Kant for various meaningful and meaningless discussions in the office.

Dr. Martin Kriegisch for his tremendous help at building up the lab here in Vienna.

Iris Haßlauer for proofreading the manuscript of this thesis and for her constant friendship throughout the years.

A special thanks goes to my brother Christian Engelbrecht, Michael Wirth and Kristin Wiltschko for their great moral support at a special occasion.

All my friends and my family for their support during the last years.

Contents

1	Introduction	1
2	Experimental Techniques	5
2.1	Sub-mm wave spectroscopy	5
2.2	Theoretical analysis	13
2.3	Numerical simulations	20
3	Basic properties of SRRs	23
3.1	Split-ring resonators	25
3.2	Description of SRR as LC-resonator	27
3.3	Homogenization problem of single layered metamaterials	33
3.4	Influence of geometry on the electrodynamics of SRRs	46
3.5	Summary	59
4	Optical properties of superconducting metamaterials	61
4.1	Quality factor in the superconducting state	61
4.2	Tunability of the resonance properties by external parameters	68
4.3	Asymmetric SRRs	72
4.4	Summary	76

5	Optical activity in chiral metamaterials	77
5.1	Chiral Metamolecules	77
5.2	Analysis by transmission matrix formalism	79
5.3	A Lagrangian viewpoint on split-ring coupling	81
5.4	Experimental characterization of coupled SRRs	84
5.5	Optical activity of inductively coupled metamaterials	91
5.6	Summary	96
6	Electric excitation of the paramagnetic resonance in GGG	97
7	Conclusion	105
A	Retrieval of boundary matrix	109
B	4×4 formalism	113
	Bibliography	117

Chapter 1

Introduction

In 1968 Victor Veselago studied a theoretical material, in which both the real parts of the dielectric permittivity and the magnetic permeability are negative [1]. Surprisingly he found, that in such a system the electric field, magnetic field and wavevector form a left-handed system, which means that in this case the index of refraction becomes negative. The negative index of refraction leads to some unusual effects, like inversed refraction, a negative radiation pressure or an inversed Doppler effect. However, at that time such properties were not realizable since no material showing negative permeability was known. It took over 30 years until the first artificial material was proposed, showing the described behaviour. In 1999 Pendry *et al.* proposed the split-ring resonator structure, which revealed negative magnetic permeability [2]. A negative electric permittivity can be obtained by an artificial medium consisting of cut-metallic wires, whose plasma frequency can be tuned by the separation of the wires [3]. In combination, both materials can lead to a material showing a negative index of refraction. This was soon realized experimentally [4]. However, beside this metamaterial realization of a negative index of refraction, today also other ways of reaching a negative index are known, for example based on chirality [5], photonic crystals [6] or ferromagnetic metals [7, 8].

The discovery of the split-ring structure was also the beginning of the metamaterial era. Metamaterials are man-made (periodic) structures, whose un-

usual optical properties are not determined by the constituent materials, but by the geometrical tailoring. The characteristic sizes in these structures are much smaller than the wavelength of the light, therefore these structures can be treated as a homogeneous material. In the following years a huge research effort took place, revealing novel and surprising possible applications, like cloaking devices [9, 10] and "superlenses", which overcome the diffraction limit of light [11, 12]. Beside these most prominent examples, metamaterials can also be used in a vast field of other applications. They can be used, amongst others, in antenna systems, as band-pass filters or in sensor applications. The huge field of possible applications, as well as the extraordinary optical properties motivated the large research effort done in the last few years. A lot of different metamaterial structures have been studied, ranging from planar structures, like split-ring resonators [2], electric-field-coupled resonators (ELC) [13] or rosette-like structures [14] to more complicated three dimensional structures like the fishnet structure [15]. This work focusses on the study of different split-ring designs. These are easy producible structures suited for a large frequency range. Their basic design can be understood by simple models, yet split-ring metamaterials shows very interesting properties leading to unexpected effects.

This work is organized as follows. In chapter 2 the measurement technique as well as the theoretical framework of the data analysis will be presented. The basic physical properties of split-ring resonators, the homogenization of single layers and the influence of their different geometrical parameters will be discussed in chapter 3. Chapter 4 is dedicated to the improvement of the quality factor of the split-rings. Structures made from superconducting niobium will be studied, leading to a significant increase in the performance of the resonances. Furthermore, the superconductivity of the metal opens up another possibility of tuning the resonance parameters. Also a modified unit cell will be presented, which decreases the radiation losses leading to a further increase of the metamaterials performance. In chapters 5 and 6 two examples will be given, how the bianisotropy of the rings can be used to build novel structures, showing unexpected effects. In chapter 5 chiral metamolecules formed by two layers of mutually twisted split-ring resonators will be studied. These quasi-molecules show a huge optical activity, which

exceeds the one in natural materials by far. In chapter 6 the split-rings will be coupled to a paramagnetic material. Hereby it will be possible to excite the electron-spin resonance in a conventional paramagnetic material using the electric component of the radiation, leading to a series of interesting effects. Finally, in chapter 7 the results of this thesis will be summarized and a conclusion is given.

Chapter 2

Experimental Techniques

2.1 Sub-mm wave spectroscopy

Experiments presented in this work have been carried out using a quasi-optical Mach-Zehnder interferometer setup, which allows an independent measurement of both, the transmitted intensity and phase shift of the radiation over a broad frequency range from 40 GHz up to 1000 GHz ($1.3 - 33 \text{ cm}^{-1}$). Since both the intensity and phase shift is measured using this setup, the optical constants of a sample of interest can be directly retrieved and a Kramers-Kronig transformation is not necessary. In addition, using slight modifications of this setup, also the determination of the reflectance and reflected phase shift is possible.

Before the measurement setup is explained in detail, first two important parts of the spectrometer, namely the radiation source and the used detectors, will be discussed briefly.

Backward wave oscillator

In all experiments backward wave oscillators (BWO) are used as light sources. BWOs are vacuum tube-based radiation sources. They deliver highly monochromatic ($\Delta\nu/\nu \approx 10^{-5}$), linear polarized radiation [16]. A heated cathode emits electrons which become accelerated by a high voltage (up to

6 kV) travelling towards the anode in vacuum. An external magnetic field collimates the electrons into a narrow beam. The electron beam travels along a comb-like fine-structure electrode, which creates a periodic potential in which the electrons are slowed down. Due to this potential the electrons become grouped in bunches and emit electromagnetic waves which are travelling in opposite direction to the electron beam (therefore the name BWO). The electromagnetic wave then gets guided using a waveguide and coupled out using a horn antenna. The energy transfer from the electrons to the radiation becomes maximal when the velocity of electrons equals the phase velocity of the radiation. Therefore the emitted frequency is directly dependent on the electrons velocity. The velocity of the electrons v_e is directly proportional to the square root of the applied high voltage U , $v_e \propto \sqrt{U}$. Thus the frequency of the emitted radiation can be tuned by the applied voltage U . However, the tuning range of one BWO source is limited to approximately $\pm 30\%$ from the center frequency. In order to cover the whole frequency range a total number of nine BWOs is available. The output power of the BWOs typically lies in the mW range (0.5 – 100 mW), with decreasing values for higher frequency generators.

Detectors

Two different kind of detectors were used in this work. Both types of detectors have certain advantages/disadvantages and will be discussed here. In order to reduce the influence of stray radiation and to increase the signal-to-noise ratio the detectors are using the lock-in technique for both the intensity as well as the phase shift measurements.

The first kind of detector is the goly cell, which is an opto-acoustic detector. It consists of a gas-filled volume which on the one side has an infrared absorbing material and on the other side a flexible membrane. When radiation is incident on the infrared absorbing window, the gas is heated. Therefore the pressure in the cell rises which leads to a deformation of the membrane. This deformation can be optically detected. For this purpose a LED is focused on the membrane and the reflected light detected using a photo-diode. The intensity on the photo-diode is a function of the curvature of the membrane.

The sensitivity of the golay cell is typically around $10^{-10} - 10^{-11} \text{ WHz}^{-1/2}$ [16], which is high enough for measurements with low frequency generators (which have a high output power) and for transparent samples (transmission $> 10^{-3}$). An advantage of the golay cells is the fact that they are uncooled, *i.e.* they work at room temperature.

For measurements at higher frequencies and/or samples with low transmission a liquid helium cooled bolometer is used for the signal detection. In this case the signal detection is based on the heating of a sensor due to the electromagnetic radiation. A semiconductor with a very large temperature coefficient at 4K is used as a sensor. Due to the incident radiation the temperature of the semiconductor rises, which can be directly measured by the change in the resistivity. Since the absorbed heat is measured directly, there is almost no dependence over a large frequency range. The sensitivity of the bolometer is approximately two magnitudes higher than that of a golay cell ($10^{-11} - 10^{-13} \text{ WHz}^{-1/2}$) [16].

Mach-Zehnder interferometer

In this paragraph the principal constituents and working principle of a Mach-Zehnder interferometer will be discussed in the framework of the transmittance setup first. Afterwards the modified setup for reflectance measurements under normal and oblique incidence will be shown and discussed. Further information about the setup can be found for example in Ref. [16].

A typical setup for transmittance experiments is shown in Fig. 2.1. The BWO (1) is a point-like source which emits a diverging beam of radiation. A lens (2) made of polyethylene ($n = 1.41 + i0.0006$ [16]) transforms the beam in a parallel one. The chopper (3) modulates the beam in the case of intensity measurements. Since the output power of the BWOs cannot be changed, two absorber blocks (4) in front of the source and the detector can be used to prevent the detector from overloading. The absorber consists of Mylar foils (polyethylene terephthalate = PET) on which thin metal films are deposited. Several absorbers with frequency independent transmission coefficients of 1%, 3%, 10% and 30% are available. The beam splitter (6a) consists of a wire grid polarizer, which transmits the radiation with the electric field polarization

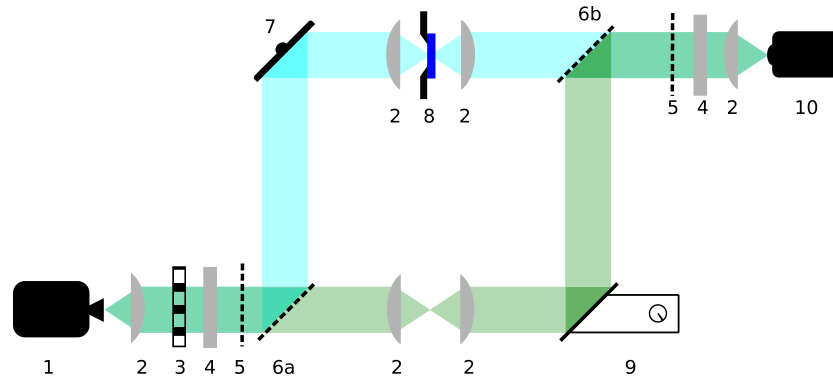


Figure 2.1: Setup for transmittance measurements: 1 - backward wave oscillator, 2 - lenses, 3 - chopper, 4 - absorber, 5 - wire grid polarizer, 6a,b - beam splitter, 7 - phase modulator mirror, 8 - sample holder, 9 - phase shift mirror and 10 - detector.

perpendicular to the wires, while the one with polarization along the wires is almost perfectly reflected. Hence the beam is divided in a reference beam (green) and a measurement one (blue) with orthogonal polarizations. In front of the beam splitter another wire grid polarizer (5) can be used to adjust the intensities in both arms of the spectrometer. The beam becomes reflected in the measurement arm by the phase modulation mirror (7), which can oscillate at low frequencies (20 – 30 Hz). For the phase shift measurement this oscillation is used to modulate the signal, while in the intensity mode the oscillation is turned off. The beam becomes focussed on the sample (8) using two lenses. A cryomagnet system can be installed in place of the sample holder, too. For this purpose a commercial available Spectromag system from Oxford Instruments is used. This allows measurements in magnetic fields up to 8 T and in the temperature range between 2 – 300 K. In the reference arm two additional lenses are used to compensate the additional optical thickness of the two lenses in the measurement arm. The phase shift mirror (9) can be moved within a range of 10 mm and is used for the phase shift measurement. Another beam splitter (6b) is used to join both beams of the spectrometer. However, since their polarizations are still orthogonal, they cannot interfere. Therefore a wire grid analyser is placed in front of the detector (10) to bring the polarizations of both rays to a common direction.

In order to conduct transmittance experiments the reference arm is closed

using a beam stopper and just the measurement arm is used. The necessary modulation for the lock-in principle is obtained by the chopper, which periodically interrupts the beam. In a first step the spectrum is measured without a sample as a function of the frequency, yielding a calibration spectrum $I_{cal}(\omega)$, where $\omega = 2\pi\nu$ is the angular frequency of the radiation. This calibration is needed to get rid of the output characteristic of the sources and to normalize the transmittance spectrum. In the second step the sample is measured and $I_{sam}(\omega)$ is obtained. The intensity transmission coefficient of the sample is calculated via $T(\omega) = I_{sam}(\omega)/I_{cal}(\omega)$.

For the phase shift measurement mode both arms of the interferometer are used. In opposite to the intensity mode the chopper is turned off and the modulation is generated by the oscillating mirror (7). Due to the wire grid analyzer both rays have the same polarization at the detector and therefore can interfere. The length of the reference arm can be changed by the moveable mirror (9). Depending on the position of the moveable mirror the both rays either interfere constructively or destructively at the position of the detector. When the frequency of the source is changed, an electronic block changes the position of the mirror in such a way that at each frequency a minimum of the signal is obtained at the detector. The absolute position Δs of the mirror is recorded as a function of the frequency ω . Analogous to the intensity measurements, two measurements are conducted, one with sample, yielding $\Delta s_{sam}(\omega)$, and one without, yielding $\Delta s_{cal}(\omega)$. The phase shift of the sample $\varphi(\omega)$ then results as

$$\varphi(\omega) = (\Delta s_{sam}(\omega) - \Delta s_{cal}(\omega) + d)\omega/c, \quad (2.1)$$

where d is the geometrical thickness of the sample and c the speed of light.

Due to the wire grid polarizers the measurements are made in distinct polarization geometries. Thus it is also possible to detect the crossed polarization signal, *i.e.* the signal with a polarization orthogonal to the incident one. This is important for optical active samples, in which the polarization direction becomes rotated. For conventional measurements the wires of the beam splitters (6a) and (6b) are orientated in perpendicular direction. When the

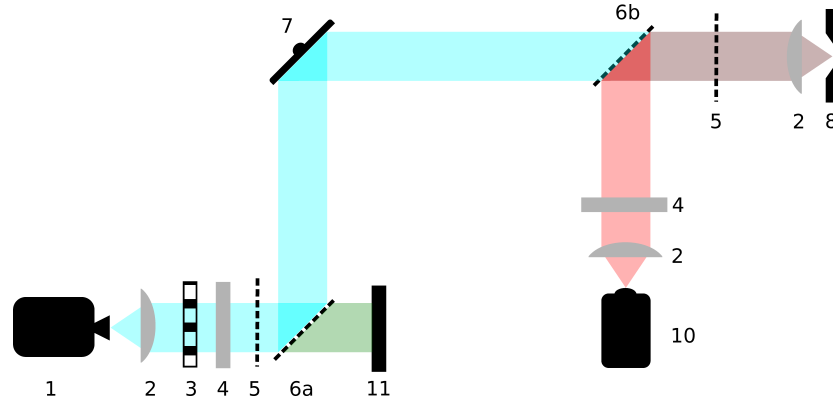


Figure 2.2: Setup for reflectance measurements under normal incidence: 1 - backward wave oscillator, 2 - lenses, 3 - chopper, 4 - absorber, 5 - wire grid polarizer, 6a,b - beam splitter, 7 - phase modulator mirror, 8 - sample holder, 10 - detector and 11 - beam stopper.

orientation of the beam splitter (6b) is changed to be parallel to (6a) just radiation with a polarization orthogonal to the incident one can reach the detector. However, this also means that no radiation in the reference beam can reach the detector. Therefore, in order to do phase shift measurements in the crossed geometry, an additional wire grid polarizer, with an orientation of 45° in reference to the first beam splitter, in the reference arm is necessary. This will ensure that some intensity in the reference arm can reach the detector. The same argumentation holds also for the calibration measurement in the main arm. Here an additional 45° wire grid polarizer will be introduced, when the measurement without the sample is conducted. However, in the measurement with sample this polarizer will be removed. Obviously a meaningful measurement of the crossed phase shift is just possible in the frequency ranges in which a crossed intensity signal can be observed.

Now, the working principle of the transmittance mode can be easily transferred to the reflectance setup. For normal incidence measurements a suitable setup is shown in Fig. 2.2. However, this setup is just suited for measurements of the reflected intensity. A setup which also can measure the phase shift under normal incidence can be found in Ref. [17]. Since just the intensity is measured, only the main arm of the spectrometer is used, while the reference arm is closed using a beam stopper (11). The reflected beam is shown in red in Fig. 2.2. In order to get the reflected beam to the de-

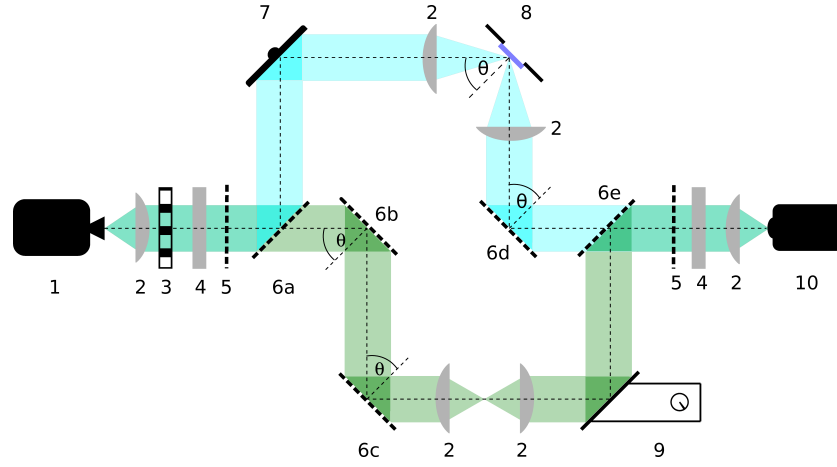


Figure 2.3: Setup for reflectance measurements under oblique incidence: 1 - backward wave oscillator, 2 - lenses, 3 - chopper, 4 - absorber, 5 - wire grid polarizer, 6a-e - beam splitters/mirrors, 7 - phase modulator mirror, 8 - sample holder, 9 - phase shift mirror and 10 - detector.

tector the beam splitter (6b) is oriented at 45° . Since this work deals with highly anisotropic samples, the measurements have to be done in well defined polarization states. Hence an additional wire grid polarizer in front of the sample is used to create the necessary polarization. Like in the transmittance experiments, the measurement consists again of two steps. In the first step the sample is measured, yielding $I_{sam}^R(\omega)$. The calibration is done using a gold mirror as a sample, which almost perfectly reflects all the incident radiation in the sub-millimetre frequency range, yielding $I_{cal}^R(\omega)$. The reflectance is then determined by $R(\omega) = I_{sam}^R(\omega)/I_{cal}^R(\omega)$. It should be noted here, that the beamsplitter (6a) and the mirror (7) are in fact unnecessary for the reflectance measurements. However, if built this way, a fast switch between reflectance and transmittance setup is possible.

Transmittance experiments under oblique incidence can be easily done, since the sample can just be tilted and no changes at the setup are necessary. However, the situation changes drastically if the reflectance should be measured in the tilted geometry. Figure 2.3 shows an appropriate setup, which also allows the determination of the reflected phase shift. In principle the determination of the phase shift in reflectance works similarly as in the transmittance mode. This setup allows the measurement under different angles of incidence

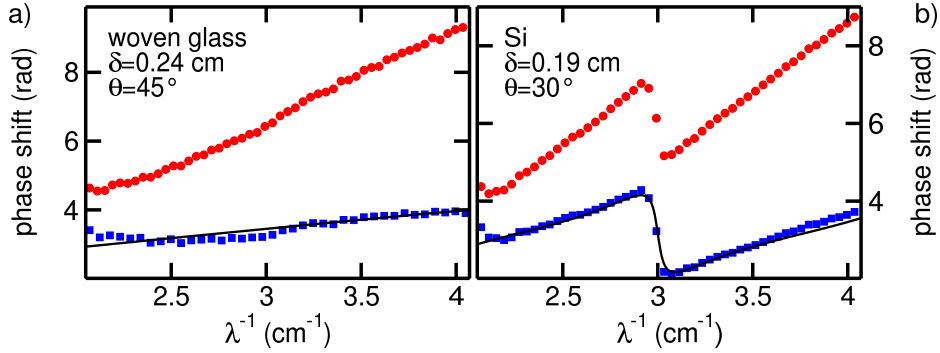


Figure 2.4: Reflected phase shift for (a) the woven glass substrate under $\theta = 45^\circ$ and (b) Si substrate under $\theta = 30^\circ$. Red circles show the original measurement, blue squares the corrected spectra after Eq. 2.3. Solid black lines show the theoretical expected spectra.

θ , whereas the angles of all the mirrors (6b)-(6d) have to be changed. When the angle of incidence is changed, also the positions of the mirrors (6b) and (6d) have to be adapted, in order to ensure the beam hitting the mirrors. The calibration of the spectra again is conducted using a gold mirror as a perfect reflecting sample. The shift of the mirror (9) is measured as a function of the frequency, one time for the sample (Δs_{sam}) and one time for the mirror (Δs_{cal}). The phase shift of the sample surface φ_r compared to the phase shift of the mirror, which is ideally π , is then related to the shift of the mirror via

$$\varphi_r - \pi = (\Delta s_{sam} - \Delta s_{cal})\omega/c. \quad (2.2)$$

For the phase shift measurement it is crucial that both the sample and the gold mirror are in the exact same position. Otherwise one will have an additional phase shift in either the calibration or measurement which will distort the results. Unfortunately the available equipment did not allow to ensure the same positions in calibration and measurement. Therefore the resulting spectra have to be corrected, to take account for the difference of the sample positions. In order to do this, two reference samples with known optical constants and thickness have been measured. The resulting phase shift spectra have been compared to theoretical calculations and a correction factor could be retrieved. How to obtain the theoretical spectra will be the topic of the next section and is therefore omitted here. As reference samples an actual

substrate of the samples investigated later (woven glass substrate) and a Si substrate have been used. The woven glass substrate has the same thickness as the actual investigated samples, and therefore the correction factor obtained here could be used for the actual experiments. The Si sample differs in thickness and thus is just used to verify the correction method. The difference in the positions lead to an error in Δs_{cal} which, for geometrical reasons, can be expressed as $2\delta \cos(\theta)$, where δ is the difference in the positions of mirror and sample. The actual phase shift resulting from the sample surface can be calculated as

$$\varphi_r = \varphi_{meas} - 2\delta \cos(\theta) \frac{\omega}{c} + \pi. \quad (2.3)$$

Figure 2.4 shows the phase shift measurements of (a) the woven glass substrate under $\theta = 45^\circ$ and (b) the Si substrate under $\theta = 30^\circ$. The red circles represent the original measurements, while the solid black lines show the theoretical expected spectra. As can be clearly seen in Fig. 2.4 a large difference between experiment and theory is observed which arises solely due to the difference of the position of the sample and the mirror. Using Eq. 2.3 this difference can be corrected which leads to the curves shown in blue squares. The corrected spectra coincide almost perfectly with the theoretical expected values. The difference in the correction factors of the woven glass substrate and the Si substrate arise due to the difference in their respective thicknesses. The correction factor of the woven glass substrate has been applied to the actual measurements of the metamaterial in Sec. 3.3.

2.2 Theoretical analysis

2.2.1 Fresnel analysis

In order to describe the transmission experiments one can obtain a 2×2 matrix formalism from the Maxwell equations and the boundary conditions for the electromagnetic field. Details of this calculations can be found in the literature, for example in [18, 19], and just the important steps are mentioned

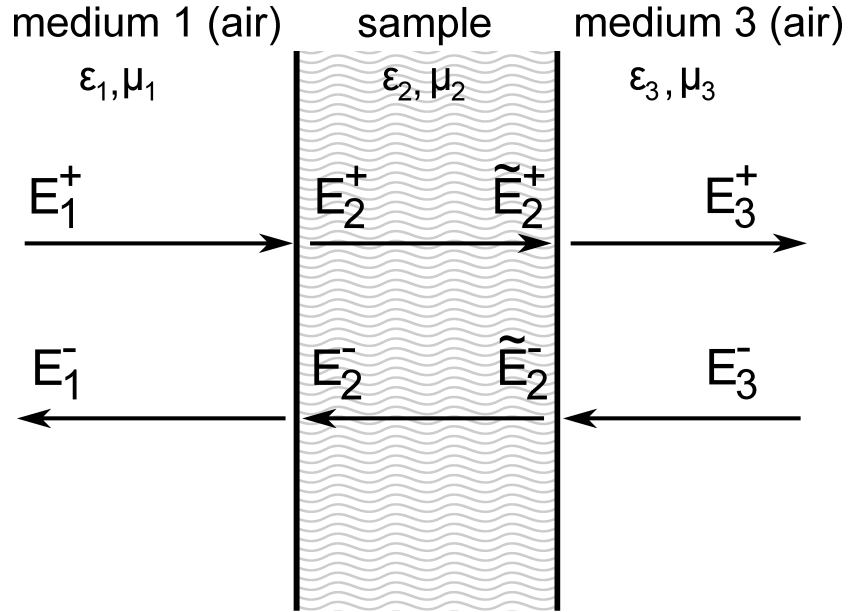


Figure 2.5: Geometry of typical transmission experiment.

here.

Consider the typical transmission experiment as shown in Fig. 2.5. The transmission of a single slab (a linear medium which can be characterized by its (complex) dielectric permittivity ϵ_2 and magnetic permeability μ_2) is measured and should be calculated. The sample is embedded in medium 1 (3) on the left (right) side. In the actual experiments the media 1 and 3 are in most cases the same (namely air/vacuum). To simplify the generalisation to the multilayer case, first the case with two different media on both sides of the sample should be considered. Following the superposition principle the electromagnetic wave in each layer could be separated in a wave travelling in the right and the left direction, respectively. Throughout this work a time-harmonic dependence $e^{-i\omega t}$ is assumed, where $\omega = 2\pi\nu$ gives the angular frequency of the wave.

The boundary conditions of the electromagnetic field determine the behaviour of the wave when travelling from one medium to another. This results

in a functional relationship in the form of:

$$\begin{pmatrix} E_2^+ \\ E_2^- \end{pmatrix} = \hat{D}_{21} \begin{pmatrix} E_1^+ \\ E_1^- \end{pmatrix}, \quad (2.4)$$

where \hat{D}_{nm} is the 2×2 boundary matrix for a transition from medium m to n . For isotropic, linear media under normal incidence, \hat{D}_{nm} is given by

$$\hat{D}_{nm} = \frac{1}{2} \begin{pmatrix} 1 + \sqrt{\frac{\varepsilon_m \mu_n}{\varepsilon_n \mu_m}} & 1 - \sqrt{\frac{\varepsilon_m \mu_n}{\varepsilon_n \mu_m}} \\ 1 - \sqrt{\frac{\varepsilon_m \mu_n}{\varepsilon_n \mu_m}} & 1 + \sqrt{\frac{\varepsilon_m \mu_n}{\varepsilon_n \mu_m}} \end{pmatrix}. \quad (2.5)$$

A detailed derivation of this boundary matrix can be found in the appendix A. For $\mu_n = \mu_m = 1$ this simplifies to

$$\hat{D}_{nm} = \frac{1}{\tilde{t}} \begin{pmatrix} 1 & \tilde{r} \\ \tilde{r} & 1 \end{pmatrix}, \quad (2.6)$$

with $\tilde{r} = \frac{n_n - n_m}{n_n + n_m}$ and $\tilde{t} = \frac{2n_n}{n_n + n_m}$ being the well known Fresnel coefficients for reflection and transmission, respectively. Within the layer the wave obtains an additional phase shift, which is dependent on the refractive index $n_2 = \sqrt{\varepsilon_2 \mu_2}$ and the thickness d of the layer. Hence, one obtains the propagation matrix \hat{P}_2 in the layer

$$\hat{P}_2 = \begin{pmatrix} e^{in_2 \omega d} & 0 \\ 0 & e^{-in_2 \omega d} \end{pmatrix}, \quad (2.7)$$

which links the fields at the left and right boundary of the sample:

$$\begin{pmatrix} \tilde{E}_2^+ \\ \tilde{E}_2^- \end{pmatrix} = \hat{P}_2 \begin{pmatrix} E_2^+ \\ E_2^- \end{pmatrix}. \quad (2.8)$$

At the right boundary again Eq. 2.5 is applied. Overall one gets a relationship between the left and the right side of the sample in the form

$$\begin{pmatrix} E_3^+ \\ E_3^- \end{pmatrix} = \hat{D}_{32} \hat{P}_2 \hat{D}_{21} \begin{pmatrix} E_1^+ \\ E_1^- \end{pmatrix} = \hat{M} \begin{pmatrix} E_1^+ \\ E_1^- \end{pmatrix}, \quad (2.9)$$

with \hat{M} being the full transmission matrix of the system. It is important

to note, that the order of the matrix multiplication in Eq. 2.9 must not be interchanged. From equation 2.9 one could already see, that this formalism can be easily extended to describe multilayer systems. In order to do this just additional propagation matrices \hat{P}_i and the according boundary matrices \hat{D}_{nm} have to be multiplied from the left side to Eq. 2.9. Throughout this work often a system consisting of a film on a substrate is studied, therefore the equation for the two-layer system is explicitly given:

$$\begin{pmatrix} E_4^+ \\ E_4^- \end{pmatrix} = \hat{D}_{13} \hat{P}_3 \hat{D}_{32} \hat{P}_2 \hat{D}_{21} \begin{pmatrix} E_1^+ \\ E_2^- \end{pmatrix} \quad (2.10)$$

\hat{D}_{21} , \hat{D}_{32} and \hat{D}_{13} are the boundary matrices at the air-film, film-substrate and substrate-air interfaces, respectively. \hat{P}_2 and \hat{P}_3 are the propagation matrices in the film and in the substrate, respectively.

Using Eq. 2.9, one is able to calculate the complex transmission and reflection coefficient. In order to do this E_3^- is set to zero, which resembles the experimental situation in which the light is irradiated from the left side. Then both the complex transmission t and reflection r can be calculated by:

$$t = \frac{E_3^+}{E_1^+} = \frac{\det(M)}{M(1,1)}, \quad (2.11)$$

$$r = \frac{E_1^-}{E_1^+} = -\frac{M(1,0)}{M(1,1)}. \quad (2.12)$$

Here $M(i,j)$ denotes the (i,j) element of the transmission matrix \hat{M} . For the two-layer system (Eq. 2.10) t and r can be constructed in the same way. In most cases the initial medium and the transmitted one are the same, *i.e.* $\varepsilon_1 = \varepsilon_3$ and $\mu_1 = \mu_3$. It is easily shown that in this case $\det(\hat{M}) = 1$ and therefore Eq. 2.11 simplifies to $t = 1/M(1,1)$. Since the intensity is measured in the experiment, the experimental transmittance (T) and reflectance (R) spectra can be obtained from Eqs. 2.11 and 2.12 via $T = |t|^2$ and $R = |r|^2$. The experimental phases result as $\Phi_t = \text{Arg}(t)$ and $\Phi_r = \text{Arg}(r)$, respectively.

The presented formalism is a powerful method of calculating transmission/reflectance spectra. However, there exist some situations in which this Fresnel formalism has some drawbacks which lead to complications when the

experimental spectra are analysed. For example, when spectra are measured under oblique incidence, the definition of the boundary matrices depends strongly on the direction of the incoming polarization (also for isotropic samples). So one has to do the calculation for the *s*-polarization (where the electric field vector is perpendicular to the plane of incidence) and *p*-polarization (electric field vector lies in the plane of incidence) separately, whereas in the general case of elliptical polarization an appropriate linear combination of a *p*-wave and a *s*-wave has to be used. The separation in two polarization directions directly leads to another problem of the Fresnel formalism. There exists some more exotic optical effects in which the polarization direction of the radiation is rotated upon passing the sample. Since the two perpendicular polarizations are calculated independent from each other, such effects cannot be accounted for in this formalism. Furthermore, also the analysis of anisotropic samples can get quite challenging in this formalism. In order to avoid this obstacles, it is advantageous to use another formalism which is the topic of the next section.

2.2.2 4x4 matrix formalism

Teitler and Henvis presented a very powerful theoretical framework in 1970 which can be used to calculate the transmission and reflection properties of (bi-)anisotropic samples [20]. This formalism also includes the description of unusual effects like Faraday rotation or optical activity. For the following considerations a sample lying in the *xy*-plane is assumed on which an electromagnetic wave with wavevector $(k_x, k_y, k_z)^T$ is incident. The presented formalism is suited for normal incidence ($k_x = k_y = 0$) as well as for oblique incidence in which the angle of incidence is given by the values of k_x and k_y . Just the important steps of the calculation are given here. The details can be found in the appendix B or in Ref. [21]. The sample is characterized by the constitutive relations

$$\begin{pmatrix} \vec{D} \\ \vec{B} \end{pmatrix} = \begin{pmatrix} \varepsilon_0 \hat{\varepsilon} & \hat{\xi}_{em} \\ \hat{\xi}_{me} & \mu_0 \hat{\mu} \end{pmatrix} \begin{pmatrix} \vec{E} \\ \vec{H} \end{pmatrix} = \hat{M} \begin{pmatrix} \vec{E} \\ \vec{H} \end{pmatrix}. \quad (2.13)$$

Here $\hat{\varepsilon}$, $\hat{\mu}$, $\hat{\xi}_{em}$ and $\hat{\xi}_{me}$ are the (complex) dielectric permittivity, the magnetic permeability and the bianisotropy parameters, which describe the magneto-electrical effect, respectively. All magnitudes are 3×3 matrices. ε_0 is the vacuum permittivity and μ_0 the vacuum permeability. Thus the material can be characterized by a 6×6 matrix \hat{M} . The Maxwell equations may also be written in matrix form:

$$\hat{R}\vec{\Gamma} = -i\omega\hat{M}\vec{\Gamma}, \quad (2.14)$$

with $\vec{\Gamma} = \vec{\Gamma}_0 e^{i\vec{k}\vec{x}}$ being the spatial part of the electromagnetic field and $\vec{\Gamma}_0 = (E_x^0, E_y^0, E_z^0, H_x^0, H_y^0, H_z^0)^T$ the amplitude of the electromagnetic field. Here, both Eq. 2.13 and the time-dependence $e^{-i\omega t}$ have already been used. \hat{R} is a 6×6 matrix, whose first and third quadrant is the rot-operator, while the second and fourth quadrant are zero. Now it is assumed, that inside the sample, \hat{M} is dependent of z only. Therefore the spatial derivatives with respect to x and y in Eq. 2.14 can be done and \hat{R} can be written in terms of the wavevector components (k_x and k_y). Equation 2.14 then is a system of two algebraic equations and four first order differential equations. The two algebraic ones can be used to eliminate two of the components and express them in terms of the other four. For the given geometry it is convenient to eliminate the normal components of the electromagnetic field, namely $\Gamma_3 = E_z$ and $\Gamma_6 = H_z$. Overall this leads to a 4×4 representation of Eq. 2.14

$$\frac{\partial}{\partial z}\vec{\psi} = i\omega\hat{S}\vec{\psi}, \quad (2.15)$$

where $\vec{\psi} = (E_x, E_y, H_x, H_y)^T$ and \hat{S} being the 4×4 representation of the material matrix \hat{M} . If \hat{S} is independent of z , Eq. 2.15 can be integrated over the whole thickness d of the sample, leading to

$$\psi(d) = \hat{P}(d)\psi(0), \quad (2.16)$$

which interconnects the electromagnetic fields at the right boundary of the sample $\psi(d)$ with the ones at the left boundary $\psi(0)$. \hat{P} is therefore the propagation matrix of the system and is to be found. In addition Eq. 2.15 simplifies to

$$k_z\vec{\psi} = \omega\hat{S}\vec{\psi} \quad (2.17)$$

which is an eigenvalue equation. The four eigenvalues k_z^i and eigenvectors $\vec{\psi}_i$ can now be determined. In simple cases this can be done analytically, but in the more interesting, *i.e.* more complex, cases this has to be done numerically. With the so obtained eigenvectors a matrix $\hat{\Psi} = \begin{pmatrix} \vec{\psi}_1 & \vec{\psi}_2 & \vec{\psi}_3 & \vec{\psi}_4 \end{pmatrix}$ can be build. $\hat{\Psi}$ can now be applied to Eq. 2.16 leading to

$$\hat{\Psi}\hat{K}(d) = \hat{P}(d)\hat{\Psi}, \quad (2.18)$$

where $\hat{K}(d)$ is a diagonal matrix with elements $K_{jj} = e^{ik_z^j d}$. Equation 2.18 can then be solved for \hat{P} giving

$$\hat{P}(d) = \hat{\Psi}\hat{K}(d)\hat{\Psi}^{-1}, \quad (2.19)$$

where $\hat{\Psi}^{-1}$ denotes the inverse of $\hat{\Psi}$. Since the normal components of the fields were eliminated the boundary matrix is just the identity matrix. Therefore just the propagation matrix $\hat{P}(d)$ is needed for calculating the transmission/reflectance spectra. In addition, the matrix formulation easily allows the extension to multilayer systems. In a multilayer system first the propagation matrix $\hat{P}(d_l)$ for each layer l is built in the way shown above. Finally the propagation matrix for the whole system is built by matrix multiplication of all layers. For a two layer system, like a thin film on a substrate, the overall propagation matrix is

$$\hat{P} = \hat{P}_{film}(d_{film})\hat{P}_{sub}(d_{sub}). \quad (2.20)$$

The order of the matrix multiplication in Eq. 2.20 gives the direction in which the wave travels through the system and must not be interchanged for a given geometry.

In order to calculate the transmission/reflectance spectra it is convenient to change the basis from $\vec{\psi} = (E_x, E_y, H_x, H_y)^T$ to $\vec{\psi}' = (E_x^+, E_x^-, E_y^+, E_y^-)^T$, where the superscript $+(-)$ denotes the part of the wave travelling in positive (negative) z -direction. The propagation matrix in the new basis is then given by $\hat{P}' = \hat{V}^{-1}\hat{P}\hat{V}$, with \hat{V} being the basis transformation matrix, which is given by the eigenmatrix of the vacuum and is explicitly shown in the

appendix B. The complex transmission and reflection coefficients can now be easily obtained by the equation

$$\begin{pmatrix} t_{xx}E_x^i + t_{xy}E_y^i \\ 0 \\ t_{yx}E_x^i + t_{yy}E_y^i \\ 0 \end{pmatrix} = \hat{P}' \begin{pmatrix} E_x^i \\ r_{xx}E_x^i + r_{xy}E_y^i \\ E_y^i \\ r_{yx}E_x^i + r_{yy}E_y^i \end{pmatrix}. \quad (2.21)$$

Here $E_{x,y}^i$ denotes the incoming electric field in x and y polarization, respectively. The r_{mn} and t_{mn} give the complex reflection and transmission amplitudes, while the indices with $m = n$ denote the parallel components, the indices with $m \neq n$ give the transmission/reflection with crossed polarization. This cross polarization components arise in samples with optical activity which rotate the polarization of light. The physical reason thereof can be due to the bianisotropic/magneto-electric components of the constitutive relations. Therefore this 4×4 formalism is a very powerful tool to calculate transmission/reflectance spectra for complex and anisotropic systems.

2.3 Numerical simulations

Simulations throughout this work have been done using the open-source finite difference time domain (FDTD) software package MEEP [22] unless otherwise noted. In the FDTD method the space is divided into a finite rectangular grid and the Maxwell equations are evolved in time using discrete time steps. The electric/magnetic fields as well as the power flux can then be calculated for any point of the simulated unit cell. MEEP therefore is very well suited to simulate the field patterns of a given structure, as well as calculating transmission and reflectance spectra. Information on the FDTD method can be found for example in Ref. [23].

This work studies the electrodynamic properties of split ring resonators. In order to resemble the experimental situation, a single split ring, made of a perfect metal, on a dielectric substrate is simulated. The dielectric properties of the substrate are chosen in a way to resemble the experimentally obtained

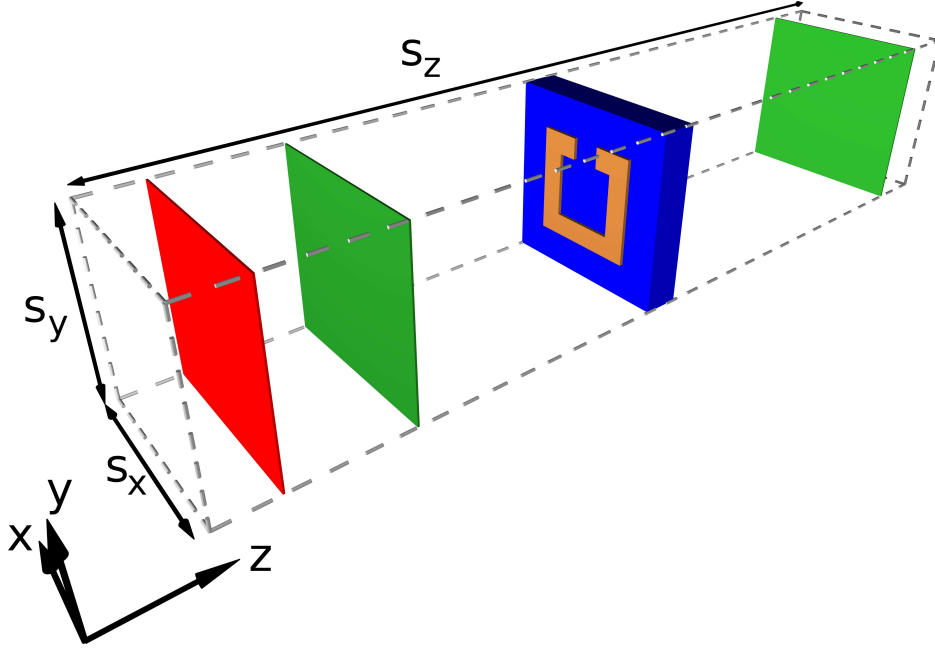


Figure 2.6: Geometry of the simulation. A single split ring on a substrate (blue) is simulated. The light is originating from a source layer with the same size (s_x, s_y) as the unit cell (red). The power flux is detected at two detector layers (green), with again the same size of the unit cell. The first detector measures the incoming/reflected flux, while the second one measures the transmitted power.

values. The simulation geometry is shown in Fig. 2.6. The size of the simulated cell is given by s_x , s_y and s_z . In the x - and y -direction the periodic boundary conditions are applied in order to account for the periodicity of the structure. The sizes s_x and s_y therefore correspond to the unit cell size of the metamaterial. With changing this sizes one changes the distance between neighbouring rings and thus their mutual interaction. Since just the far field response of the structure is studied throughout this work, the size s_z is chosen so that the source/detector are several wavelengths apart from the actual sample. In the z -direction the simulated unit cell is limited by perfectly matched layers. These layers are an artificial material, which absorbs all the incoming radiation, and are used in order to prevent unwanted back reflections from the zone boundaries.

The light is coming from a source layer at the left end of the simulated cell

(shown in red in Fig. 2.6). The size of the layer is the same as the lateral cell size in order to ensure a plane wave excitation of the structure. To calculate the transmission/reflection spectra two detector layers are used to measure the power flux in front and behind the structure (shown as green layers). In order to obtain the frequency dependent spectra it is more efficient to work in time space rather than simulate each frequency independently. Hence the excitation is given by a Gaussian pulse. In the plane of the detector the Fourier transforms of the electric and magnetic field are then accumulated and the frequency dependent power flux is calculated. Since the power flux itself is not normalized, a second simulation without a sample is needed to calibrate the spectra. This is similar to the experimental situation and therefore each simulation has to be done twice, first with the sample and then with the empty simulation cell. By dividing both spectra the transmission/reflection spectra can be obtained.

Chapter 3

Basic properties of SRRs

In the last decade a vast variety of possible metamaterial structures has been proposed. One of the most investigated structures is built of split-ring resonators (SRRs). The name "split-ring resonator" was first used in 1981 by Hardy and Whitehead who proposed a similar structure as a high Q-resonator in magnetic resonances [24]. The structure itself was discussed even earlier in the context of nuclear magnetic resonance (NMR) experiments under the names "slotted-tube resonator" in 1977 [25] and "loop-gap resonator" in 1996 [26]. Today's most common design used in the metamaterials community has been proposed by Pendry in 1999 [2]. Such structures can be easily produced by standard lithographic techniques and are largely scalable over a broad frequency range. However, they are not suited for frequencies in the near-infrared and above this range for two reasons: first, the structures become so small, that current production techniques fail and second, the conductivity of all metals decreases significantly, leading to a saturation of the response of the rings [27].

Originally split-ring resonators were proposed as an artificial material showing a negative magnetic permeability. Although composed of non-magnetic material, the structure shows a magnetic response which is large enough to obtain a negative magnetic permeability, which is a key property of reaching a negative index of refraction. Shortly after its introduction, the first theoretical and experimental realization of a medium with a negative index of

refraction took place, using SRRs as negative permeability medium [4, 28]. In this case the negative permittivity was obtained using a wire medium. However, besides the magnetic response, split rings have also an electric response [29]. Therefore a negative index material consisting of SRRs only could be realized due to an appropriate orientation of the rings [30, 31].

Beside the negative permeability and permittivity the rings have an additional interesting property. The SRRs are bianisotropic materials, which means that their constitutive relations show a cross-coupling between the electric and magnetic field, *i.e.* an electric field can create a magnetisation of the material and vice versa. Therefore the constitutive relations of the SRRs have the form:

$$\begin{aligned}\vec{D} &= \varepsilon_0 \hat{\varepsilon} \vec{E} + \hat{\xi}_{em} \vec{H} \\ \vec{B} &= \mu_0 \hat{\mu} \vec{H} + \hat{\xi}_{me} \vec{E},\end{aligned}\tag{3.1}$$

where $\hat{\varepsilon}$, $\hat{\mu}$, $\hat{\xi}_{em}$ and $\hat{\xi}_{me}$ are all tensors of second order and describe the electric permittivity, magnetic permeability and magneto-electric cross-coupling, respectively. Hence SRRs can be viewed as a special kind of magneto-electrical media. The bianisotropy of the rings opens up another degree of freedom in controlling the properties of light passing through this material.

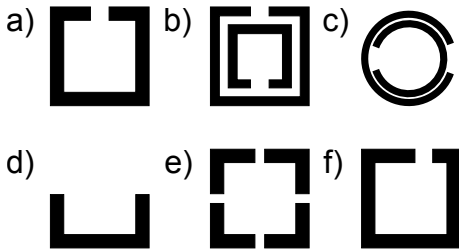


Figure 3.1: Different designs for split ring resonators.

Although there are many different appearances of the SRRs today, their basic properties are very similar. Some of the most common designs are summarized in Fig. 3.1. They range from single or double rings, with (a,b) quadratic [32, 33] or (c) circular [2] base area to (d) rectangular [34] design. Also (e) rings with more than one slit [35] or (f) asymmetric slit design [36] have been investigated. Most

of the experiments throughout this work have been done using the single split-ring design (Fig. 3.1 (a)). In addition, also some experiments have been conducted on the double split rings (Fig. 3.1 (b)).

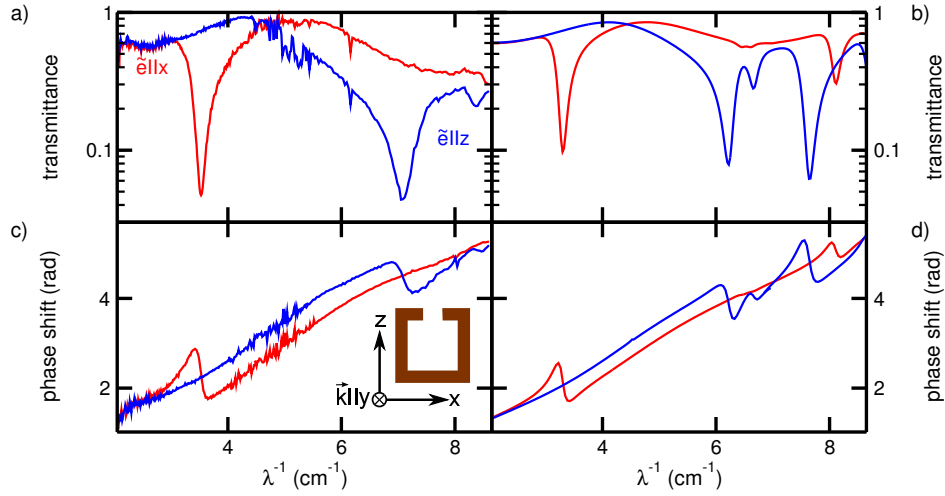


Figure 3.2: Experimental (a,c) and simulated (b,d) millimeter wave spectra of a split ring resonator in two excitation geometries. (a),(b) Transmittance and (c),(d) phase shift of transmittance. The inset in (c) shows the excitation geometry.

In this chapter the basic properties of the SRRs are studied. Section 3.1 first gives a brief introduction into the characteristics of the split rings. A simple theoretical model to understand this properties will be given in Sec. 3.2. Section 3.3 then will discuss the problem of material homogenization in metamaterials from an experimental point of view. Finally Sec. 3.4 summarizes the influence of the different geometrical parameters of the SRRs on their electrodynamic parameters.

3.1 Split-ring resonators

In Fig. 3.2 typical transmittance (a,b) and phase shift spectra (c,d) of SRRs are presented, obtained in experiment (a,c) and by simulation (b,d). The geometrical parameters for this particular sample (definitions are given in Fig. 3.3 (a)) are: $l = 0.35$ mm, $g = 0.13$ mm, $w = 20$ μm and $t = 20$ μm . The unit cell size is $s = 0.9$ mm. All investigated samples in this chapter have been produced by chemical etching of a copper-laminated board using an optical mask. As dielectric substrate the woven glass with thickness of $d_{sub} = 0.48$ mm has been used. The complex refractive index of the substrate was

determined in a separate experiment as $n_{sub} = 1.90 + 0.07i$ (not shown). Due to the anisotropic appearance of the SRRs, their electromagnetic response highly depends on the incoming polarization of the radiation.

Two typical excitation geometries (with the wavevector perpendicular to the plane of the ring) are shown in Fig. 3.2, indicated by the inset of (c). In the first geometry the incoming electric field is polarized along the gap (red lines), while in the other one the electric field is perpendicular to the gap (blue lines). Here it has to be noted, that both shown excitation geometries are purely electrical, which at first glance contradicts the original idea of using the SRR to obtain a negative permeability. But, as will be discussed in more detail later, the first electric and magnetic mode coincide, which is why this excitation is often referenced by the term electric excitation of the magnetic resonance [29].

One clearly observes multiple resonances in Fig. 3.2 (a,c). The fundamental mode lies around 3.5 cm^{-1} and can be excited with the electrical field parallel to the gap. Higher modes can be experimentally found at around 7.1 cm^{-1} and 8.4 cm^{-1} in the perpendicular polarization. It has to be noted that the high noise below 3 cm^{-1} and between 4 and 6 cm^{-1} arises due to the small output power of the BWO sources at these particular frequencies. The simulated spectra agree qualitatively very well with the experimental data, whereas some differences are visible. Overall the resonance frequencies of the different modes are slightly red-shifted in the simulation ($\lambda_0^{-1} = 3.3, 6.2$ and 6.7 cm^{-1} for the first three modes). Even higher modes are visible in the simulation due to this frequency shift. Also the strength of the resonances is slightly smaller in the simulation than in experiment. This slight disagreement between experiment and simulation arises due to different reasons. First of all the actual samples are subjected to production errors (the production process has an accuracy of about $20 \mu\text{m}$), which alone could be an explanation of the observed resonance shift. Also a small difference in the refractive index of the substrate between experiment and simulation could be the reason for both the frequency shift and the difference in intensity. Although the finite ohmic resistance of the copper is neglected in the simulations (for simulation details see Ch. 2.3), this can be ruled out as a reason

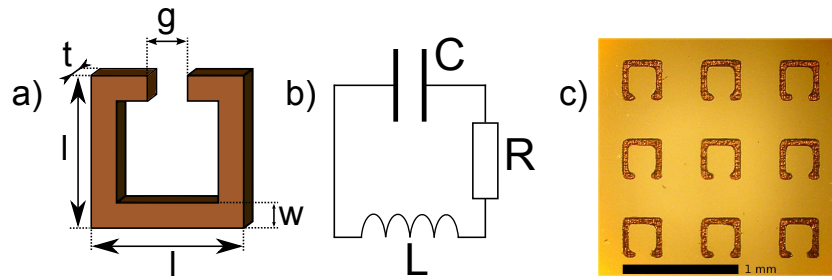


Figure 3.3: (a) schematic view (including the geometrical parameters), (b) equivalent circuit model and (c) actual picture of split ring resonators.

for the observed differences, since good metals (as copper or silver) behave almost perfectly at the used frequencies [37].

The fundamental mode is the most interesting one, since it is the mode which shows a magnetic response. In opposite to that, the higher modes cannot be excited using a magnetic field. Nevertheless, the first higher mode has been extensively investigated in the literature [32, 38, 39]. There, it has been shown that in these mode the currents are induced parallel to the polarization of the exciting electric field. This resonance therefore is related to the plasmon resonance in a thin continuous wire which is shifted to nonzero frequencies due to the additional depolarization field arising from the finite side length of the SRR. The even higher modes were discussed in the literature, too, where it has been found that they also show the characteristics of plasmonic resonances [40]. The characteristics of the fundamental mode are discussed in more detail in the following.

3.2 Description of SRR as LC-resonator

The modes, shown in Fig. 3.2, arise due to different reasons. The fundamental mode can be understood in terms of a simple (R)LC-circuit model [32]. An equivalent circuit model is shown in Fig. 3.3 (b). In this picture the gap of the ring acts as a capacitance (C), while the whole area of the ring could be understood as a single loop of a coil, which leads to an inductance (L). It could also be necessary to consider an ohmic resistance (R) to account for

losses, depending on the conductivity of the used metal. This simple model allows the determination of the resonance frequency by using the Kirchhoff's circuit laws. This directly leads to an homogeneous differential equation for the (time-dependent) charge q accumulated in the gap of the rings:

$$L \frac{d^2 q}{dt^2} + \frac{q}{C} + R \frac{dq}{dt} = 0, \quad (3.2)$$

which could be easily solved using an harmonic time-dependent ansatz for the charge $q = q_0 e^{-i\omega t}$. This leads to

$$\omega_{1/2} = \frac{i}{2}\gamma \pm \omega_R, \quad (3.3)$$

where $\gamma = R/L$ describes the damping of the circuit and

$$\omega_R = \sqrt{\frac{1}{LC} - \frac{R^2}{4L^2}} \quad (3.4)$$

the resonance frequency. In case of a negligible resistance of the metal, this simplifies to the well known resonance frequency of a LC-circuit [41]

$$\omega_0 = \sqrt{\frac{1}{LC}}. \quad (3.5)$$

An important magnitude for resonators is the quality factor (Q-factor), which gives the ratio of the energy stored in the resonator to the energy supplied by a generator. For a series RLC-circuit the Q-factor is given by [41]:

$$Q = \sqrt{\frac{L}{CR^2}} = \frac{\omega_0}{\gamma}. \quad (3.6)$$

In addition the LC-circuit model enables the determination of the resonance strength and form. Therefore in Eq. 3.2 an additional external excitation has to be included. This leads directly to

$$U = I \left(R + i\omega L - \frac{1}{i\omega C} \right), \quad (3.7)$$

with U being the external excitation. Therefore the wave impedance equals

to $Z = (R + i\omega L - \frac{1}{i\omega C})$. The further proceeding depends on the kind of excitation.

First the excitation by an external electrical field E along the gap should be considered. Since the wavelength of the radiation is considerably larger than the gap distance, we can assume a constant electric field over the whole gap distance yielding $U = Eg$. To obtain the electric response χ_e of the ring, it is necessary to know the rings polarisation $P = \varepsilon_0\chi_e E$, which is defined as $P = \frac{dp}{dV}$, where p is the microscopic dipole moment of the ring and V the volume. Since the induced charge is localised at and constant over the gap, one gets $P = \frac{qg}{V_{uc}}$, with V_{uc} being the volume of the unit cell. Using $I = \frac{dq}{dt}$ it follows

$$I = i\omega \frac{PV_{uc}}{g} \Rightarrow \chi_e = \frac{P}{\varepsilon_0 E} = \frac{g^2}{\varepsilon_0 V_{uc} Z} = \frac{\Delta\epsilon\omega_0^2}{\omega_0^2 - \omega^2 - i\gamma\omega}. \quad (3.8)$$

The last step in Eq. 3.8 uses the definitions $\Delta\epsilon = \frac{Cg^2}{\varepsilon_0 V_{uc}}$, $\gamma = \frac{R}{L}$ and Eq. 3.5.

Since the split-rings are bianisotropic (see Eq. 3.1), a magnetic response to an external electric field is expected, too. The magnetic dipole moment m of a conducting loop is given by $m = IS$, where S is the area of the ring and I the current in the loop. The current I is implicitly given in Eq. 3.7 with the same excitation U as in the pure electric case. For the magnetization M the same considerations as for the polarization are valid. Therefore $M = \frac{dm}{dV} = \frac{m}{V_{uc}} = \sqrt{\frac{\varepsilon_0}{\mu_0}}\chi_{me}E$, where the last step uses Eq. 3.1. Overall it follows

$$\chi_{me} = -\sqrt{\frac{\mu_0}{\varepsilon_0}} \frac{i\omega g S}{V_{uc} Z} = -i \frac{\Delta\xi\omega\omega_0}{\omega_0^2 - \omega^2 - i\gamma\omega} = -i\xi_{SRR} = \sqrt{\varepsilon_0\mu_0}\xi_{me}, \quad (3.9)$$

with $\Delta\xi = \sqrt{\frac{\mu_0}{\varepsilon_0}} \sqrt{\frac{C}{L}} \frac{gS}{V_{uc}}$.

The same considerations as above can be made for an excitation by an external magnetic field H . This field will induce a voltage U at the inductance for which $U = -\dot{\Phi} = -i\omega\mu_0 SH$ holds, where Φ is the magnetic flux through the inductance. Repeating the above approach then lead to

$$\chi_m = \frac{\mu_0 S^2 \omega^2}{V_{uc} Z} = \frac{\Delta\mu\omega^2}{\omega_0^2 - \omega^2 - i\gamma\omega}, \quad (3.10)$$

with $\Delta\mu = \frac{\mu_0 S^2}{V_{uc} L}$.

In addition the external magnetic field also induces an electric polarization $P = \sqrt{\varepsilon_0 \mu_0} \chi_{em} H$. Using the above equation for the induced current one gets

$$\chi_{em} = \sqrt{\frac{\mu_0}{\varepsilon_0}} \frac{i\omega S g}{V_{uc} Z} = i \frac{\Delta\xi \omega \omega_0}{\omega_0^2 - \omega^2 - i\gamma\omega} = i\xi_{SRR} = \sqrt{\varepsilon_0 \mu_0} \xi_{em}. \quad (3.11)$$

As can be seen at Eq. 3.9 and 3.11 the cross-coupling parameters are the same except for the sign. Furthermore it can be seen from Eq. 3.8 - 3.11 that the susceptibilities fulfil the relation $\chi_{em} \chi_{me} = \chi_e \chi_m$, which is the theoretical maximum of the electromagnetic cross-coupling and much larger than in any natural material [42]. It has to be noted that in SRRs the electric polarization appears across the gap and the magnetic moments are perpendicular to the plane of the rings. This has to be considered when using Eq. 3.8 - 3.11 to calculate the spectra. In addition all coupling effects between different rings are omitted. But changing to the effective fitting parameters, $\Delta\varepsilon$, $\Delta\mu$ and $\Delta\xi$ nevertheless allows to take account for these coupling effects, at least to a certain amount, as will be shown later.

Fig. 3.4 compares the excitation of the rings by the electric (blue) and the magnetic field (red). The insets illustrate the respective geometries. Obviously in both geometries the fundamental mode of the rings can be excited. In addition, the first plasmonic mode can be observed around 5.9 cm^{-1} in the magnetic geometry. If the external magnetic field \tilde{h} has a component normal to the plane of the rings, an oscillating current in the rings will be induced, which, analogous to an atomic orbital current, will create a magnetic field, which counteracts the driving magnetic field and therefore can lead to a negative permeability. On the other hand the asymmetry in the rings, induced due to the gap, leads to a nonzero average polarization of the SRR relative to the external electric field \tilde{e} , which also allows the creation of the circulating current at the same frequency as in the magnetic excitation. This was first shown by Gay-Balmaz and Martin [43] in the microwave regime, Katsarakis *et al.* [29, 44] in the microwave and far-infrared regime and up to 100 THz by Linden *et al.* [32]. The difference in the strength of the resonance which can be seen in Fig. 3.4 does not allow the conclusion that the electric excitation

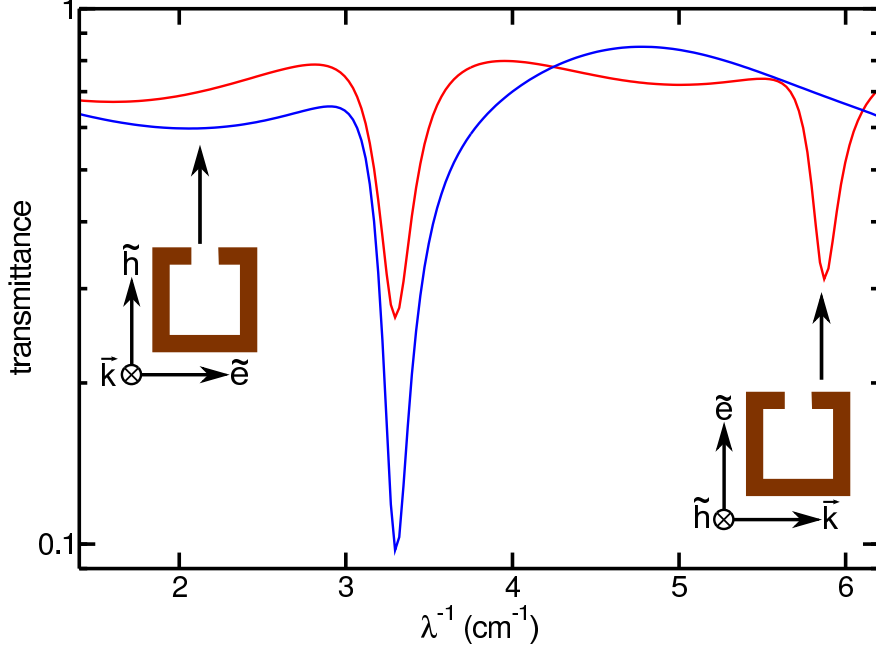


Figure 3.4: Simulated transmittance of SRR in pure electric (blue) and magnetic (red) excitation geometry. The insets illustrate the respective geometries.

is stronger than the magnetic. This effect just results due to the different geometries in the simulation. On the one hand the light passes through a substrate with thickness $d_{sub}^{el} = 0.48$ mm in the pure electric geometry. On the other hand the thickness of the substrate d_{sub}^{mag} which the light has to travel through in the magnetic geometry is 0.9 mm. Since the substrate is lossy, more energy is lost in the substrate, which leads to the weaker resonance in Fig. 3.4. It has been shown in measurements of single rings in the microwave region, that the magnetic excitation is in fact stronger than the pure electric one [43].

The equivalence of the electric and magnetic excitation allows the usage of the electric geometry for characterization of the SRR. This is experimental much easier to realize since the experiments can be done under normal incidence with the SRR-samples produced as simple films (see Fig. 3.3 (c)). Otherwise

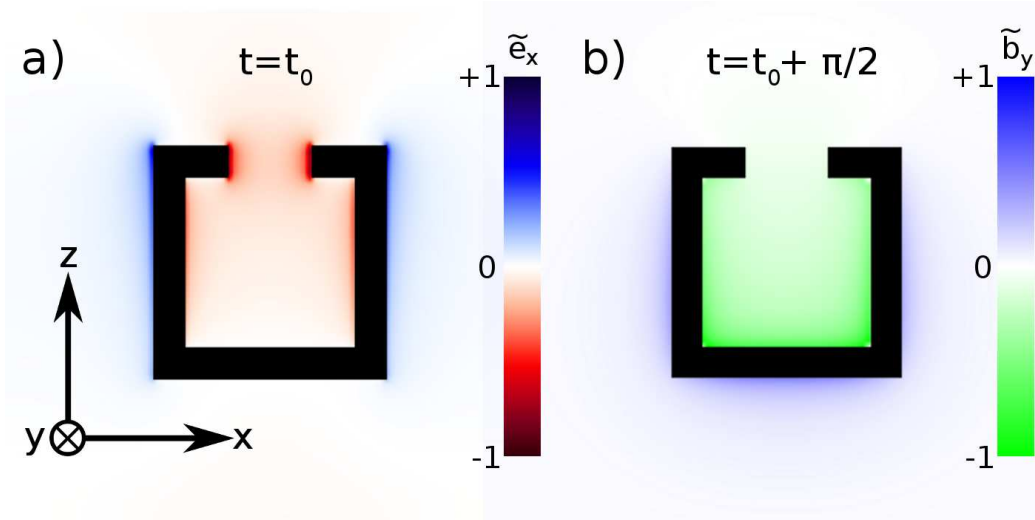


Figure 3.5: Simulated (a) electric field (x component) and (b) magnetic field (y component) distribution at a frequency of $\lambda^{-1} = 3.3 \text{ cm}^{-1}$.

the production process will be much more complicated since the propagation of the light has to be in the plane of the rings. It just has to be considered that the oscillation of the circular current influences the behaviour of the permittivity $\varepsilon(\omega)$ instead of the permeability $\mu(\omega)$.

To conclude the description of the rings fundamental resonance Fig. 3.5 shows the simulated field distribution at the resonance frequency of 3.3 cm^{-1} . The incident wave propagates along the y-direction with the electric field \tilde{e} oriented along the x- and the magnetic field \tilde{h} along the z-direction. Fig. 3.5 (a) shows the resulting electric field distribution along the x-direction, while (b) shows the resulting magnetic flux density along the y-direction. Since under normal incidence there is no optical activity of the SRR, the other components have no interesting features and therefore are not shown. In Fig. 3.5 (a) it can be clearly seen, that the resulting electric field is mainly focused in the gap of the ring, which legitimates the assumption of the gap being the main capacitance in the derivation of the LC-circuit model. Fig. 3.5 (b) is a nice proof of the bianisotropic character of the SRR, since it shows that a magnetic response occurs although just an electric excitation is present. It can also be seen that the magnetic field is mainly created inside the ring, like it is typical for a coil. As expected there is also a time-delay between the

maximal electric and magnetic response of $\pi/2$.

3.3 Homogenization problem of single layered metamaterials

An important discussion in the field of metamaterials is devoted to the homogenization of their effective electrodynamic properties. In general, the homogenization of a system is possible as long as the condition $a \ll \lambda$ holds, where a is the characteristic size of the system and λ the wavelength of light. In this case the variation of the electromagnetic field over the distance a could be neglected and the system could be seen as a "quasistatic lattice". For natural materials this condition is easily fulfilled up to the UV-range of the electromagnetic radiation since the atomic sizes and inter-atomic distances are a thousand times smaller than the wavelength of light. In this case the radiation does not see the particular constituents and the system acts as a continuous media which can be described by effective optical properties, like dielectric permittivity (ε) and magnetic permeability (μ). For metamaterials however the characteristic sizes typically lie within the band $0.01 < \frac{a}{\lambda} < 0.2$ [45]. Therefore, a proper homogenization has to be carried out with caution, since especially close to resonances, the effective optical parameters of metamaterials often lead to physically incorrect descriptions of the electrodynamic response, like a negative imaginary part of the permittivity/permeability [46]. Much theoretical work has been done in this field recently [47–56]. Typical reasons for these problems are nonlocality and spatial dispersion, which cannot be neglected [52, 54]. Other effects making the homogenization more complicated are bianisotropy [56–58] and internal coupling [59]. In order to be still able to control and predict the electrodynamic properties of metamaterials, various concepts have been suggested including field averaging [48], Bloch mode analysis [55, 59] and new parametric concepts [60].

One possible approach to the parametrization of the electrodynamic parameters utilizes the concept of multilayer metamaterials. Such metamaterials are often referred to as metafilms or metasurfaces [58, 61–63]. Application of

the standard bulk homogenization procedures to metafilms leads to substantial drawbacks or even fails completely. To overcome this problem various approaches have been presented in the literature (see, *e.g.* Refs. [49, 52, 62]). All approaches have in common that they introduce some kind of averaged (electric or magnetic) field at the metasurface. The averaged fields are then used to define new parameters which reproduce the response of the metafilms. One possible approach to this problem is presented in Refs. [58, 62, 63] and describes the metafilms utilizing the concept of surface polarizabilities. Although this ansatz is analytically correct, it contains difficulties concerning the experimental realization. To extract the surface polarizabilities from experimental data both the complex transmission and reflection coefficients are needed, which makes it difficult to retrieve these parameters. Here especially the phase shift of the reflectivity is hard to obtain experimentally [17]. Furthermore all presented theories do not cover the bianisotropy term at the moment and therefore are not suited to describe the split ring resonators studied in this work.

In this section the concept of a metafilm is used to describe the experimental electrodynamic response using effective values for ε and μ . In order to do this, a two layer model and the classical Fresnel equations are used. Three different samples with varying gap sizes were produced. The size of the rings in all samples is $0.4 \times 0.4 \text{ mm}^2$ with a gap width of 0.15, 0.25 and 0.3 mm and a copper thickness of $20 \mu\text{m}$. The lattice constant of the metamaterial is 0.9 mm for all the samples. As a dielectric substrate the woven glass with thickness of $d_{sub} = 0.48 \text{ mm}$ has been used. The complex refractive index of the substrate was determined in a separate experiment as $n_{sub} = 1.90 + 0.07i$. At first the experiments were done under normal incidence to avoid cross-polarization effects [64]. To support the experimental findings also simulations have been conducted (see Sec. 2.3 for details). The experimental/simulated spectra are analysed using the classical Fresnel formulas for the complex transmission and reflection coefficients of the substrate-ring system as introduced in Sec. 2.2.1.

The excitation geometry of the split ring metafilm, used in the present experiments, is shown in the inset of Fig. 3.6. The electrical field is chosen parallel

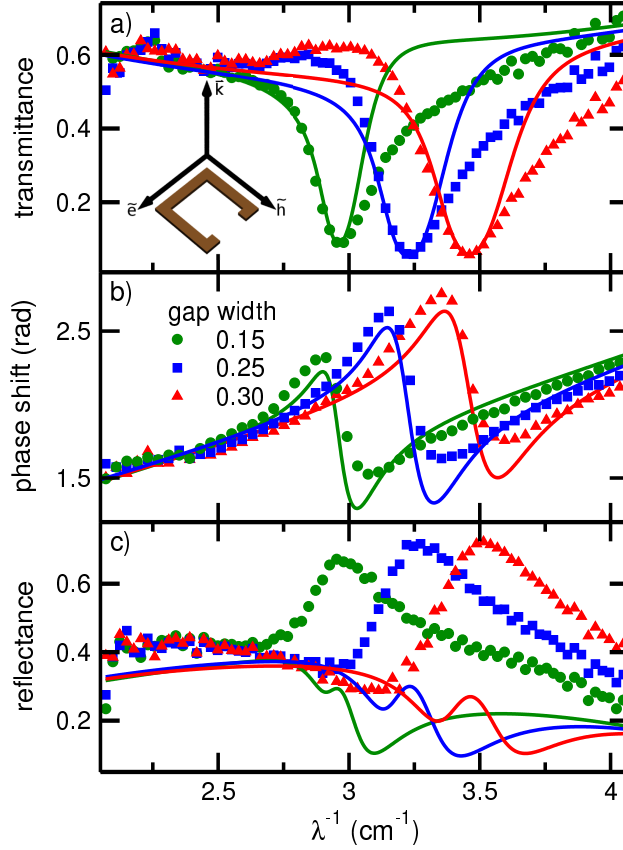


Figure 3.6: Experimental millimeter wave transmittance (a), phase-shift (b), and reflectance (c) spectra of SRR structures with different gap sizes. Gap width is given in millimeters. Symbols denote the experimental data, while solid lines show a single layer fit assuming bulk properties of the metamaterial, Eqs. (2.9,3.12). Inset: excitation geometry, where \tilde{e} denotes the electrical field and \tilde{h} denotes the magnetic field of the incident radiation.

to the gap of the rings, so the rings are excited electrically. Therefore, the response of the rings is described by the dielectric permittivity, while the permeability can be taken as $\mu = 1$. To describe the resonance the Lorentz shape as derived in Sec. 3.2 is used.

Figure 3.6 shows the transmittance (a), phase shift (b), and reflectance (c) of the three samples investigated. A blue shift of the resonance frequency is observed while increasing the width of the gap. This effect will be discussed in more detail later and therefore is neglected here. In addition, it has to be noted, that in opposite to transmittance experiments, the reflectance

measurements depends on the direction in which the light passes through the ring-substrate-system [19]. Although all measurements have been done in both directions (first layer rings, second layer substrate and vice versa) just the measurements of the rings-substrate system are shown. However also for the substrate-ring system all presented results stay valid as long as the propagation direction is also considered in the theory.

In a first step the experimental data is fitted using a simple single layer model. The metafilm in this case is treated as a bulk sample. To obtain the properties of the homogenized layer the frequency-independent permittivity of the substrate is added to Eq. 3.8. Therefore the permittivity ε of the homogenized layer is:

$$\varepsilon = \varepsilon_{sub} + \chi_e, \quad (3.12)$$

where ε_{sub} is the permittivity of the substrate ($\varepsilon_{sub} = n_{sub}^2$) and χ_e is given in Eq. 3.8. Strictly speaking, ε_{sub} is an additional free parameter of the model, which is fully determined by the values of the phase shift far from the resonance. Equation 2.9 is then used to fit the experimental transmittance and phase shift. The fits are shown with solid lines in Fig. 3.6. The fits for the complex transmittance (Figs. 3.6(a) and 3.6(b)) show a reasonably good agreement between experiment and theory, although remarkable systematic deviations at the high-frequency side of the resonance can be clearly seen. In contrast to the transmittance, the fits show no agreement at all for the reflectance data (Fig. 3.6(c)). In agreement with the discussion in the literature [49, 53, 55, 62] this behaviour could be well expected and clearly demonstrates the collapse of the bulk model for this metafilm. Therefore, it has been shown that the single layer homogenization is inadequate in this case.

Now it will be shown that the situation changes drastically if a two layer model is used to describe the metafilm. The first layer is taken as an "effective" layer describing the response of the metafilm, and the second layer represents the properties of the substrate. Thus the permittivity of the split ring layer is taken as $\varepsilon_{SRR} = 1 + \chi_e$ with the susceptibility χ_e again given by a single Lorentzian, Eq. 3.8. For the thickness d_{SRR} in the first run just the nominal value of $20 \mu\text{m}$ is used. The result of this approach is shown in Fig.

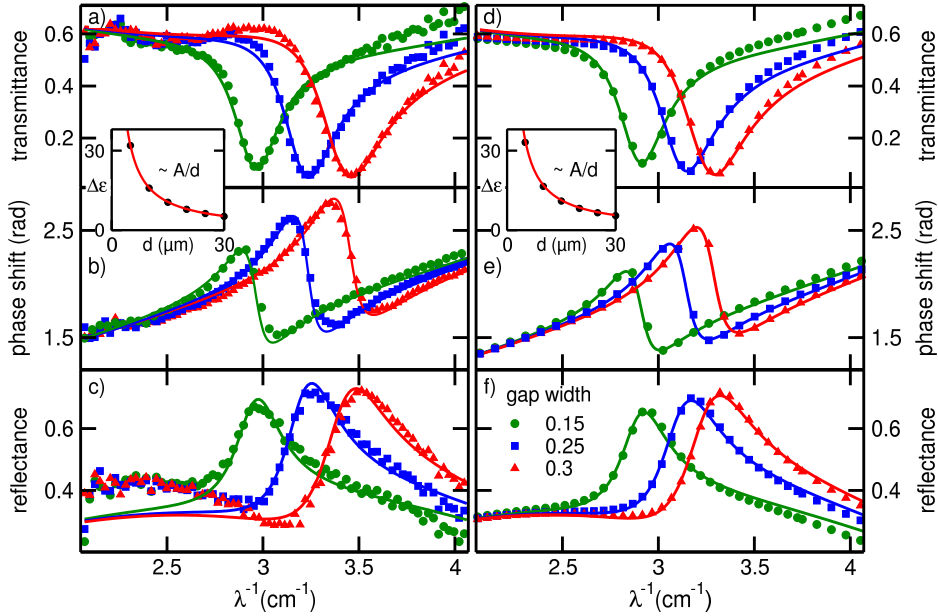


Figure 3.7: Measured (a-c) and simulated (d-f) millimeter wave spectra of SRR structures with different gap sizes. Gap width are given in millimeter. (a,d) - transmittance, (b,e) - phase shift of the transmittance, (c,f) - reflectance. Symbols denote the experimental/simulated data, solid lines show the fits using a two layer model. Inset in a,d shows the thickness dependence of the resonance strength for the sample with the gap width $g = 0.25$ mm.

3.7. The solid lines show the fit with the two layer model. As can be clearly seen in Fig. 3.7(a) now also the high-frequency wing of the transmittance data is reproduced very well by the model. Figure 3.7(b) shows in addition the phase spectra of the transmitted light, which are also very accurately described by the two layer model. And in contrast to the single layer approach now also the reflectance data is almost perfectly reproduced (Fig. 3.7(c)). To support these results the same procedure has been applied to simulated data, shown in Figs. 3.7(d)-3.7(f). The simulated spectra show a closely similar behaviour as the experimental data, and they can be almost perfectly described using the expression for the two layer structure. It has to be noted that weak discrepancies in reflectance at low frequencies (Fig. 3.7(c)) are absent in simulation data and are most probably due to diffraction effects. As expected, the fit parameters for the experiment (Fig. 3.7, left panels) and for the simulation (Fig. 3.7, right panels) closely coincide.

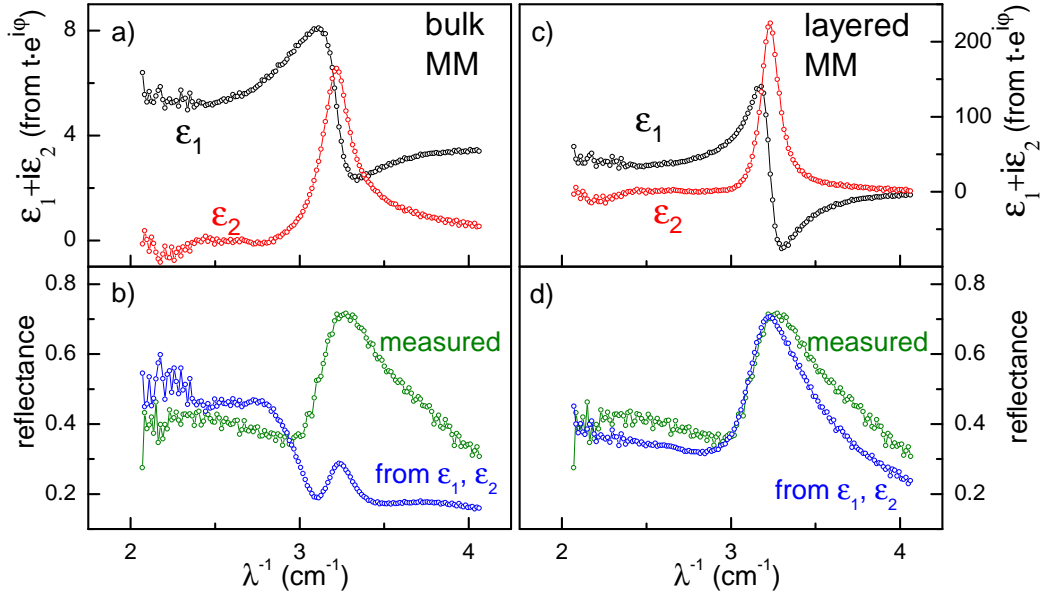


Figure 3.8: Complex dielectric permittivity extracted from experimental transmittance and phase shift data using the single layer model (a) and the two layer model (c). The results are shown for the sample with the gap width 0.25 mm. Bottom panels represent the reflectance calculated with experimental permittivity (top panels) using bulk metamaterial (b) and layered metamaterial (d), respectively.

As a next step the measurement of the transmittance and phase-shift spectra of the metamaterial allows the extraction of the complex values of the dielectric permittivity by numerical inversion of the Fresnel equation using either the bulk or the multilayer approach. The extracted permittivity spectra are shown in Fig. 3.8(a) for the bulk metamaterial and in Fig. 3.8(c) for the layered model. At first glance, the extracted values seem reasonable for both models. The permittivity shows a Lorentz-like behaviour in both cases, which supports our approach based on Eq. 3.8. This extracted ϵ can now be used to calculate the expected reflectance directly. The result is shown in Fig. 3.8(b) for the bulk and in Fig. 3.8(d) for the layered metamaterial. For comparison again the experimentally obtained reflectance is shown. In Fig. 3.8(b) a large deviation from the experimental data is observed, while the layered model (Fig. 3.8(d)) shows a fairly good agreement between the calculation and the measured data, which supports the previous argumentation.

It may now be concluded that the two layer approach could be used to de-

scribe the response of the SRR metafilm on a substrate, at least in a geometry with electric excitation of the resonance. But since the metafilm layer is not infinitely thin, the question about the correct choice of the metafilm thickness d_{SRR} remains open. Depending on the choice of the "effective" thickness of the layer, one gets different results for the permittivity. This problem was previously discussed in the literature [62, 63], and the conclusion has been drawn that the effective optical parameters, like permittivity, are ambiguous to describe metafilms. The suggested solution is based on the concept of the effective surface polarizability that replaces the bulk permittivity.

In present experiments, although the thickness of the SRR film is finite, it still can be neglected compared to the wavelength. In this approximation the Fresnel equations do not depend explicitly on the thickness d_{SRR} but instead on the product $d_{SRR} \cdot \varepsilon_{SRR}$. In fact, this product is physically the same as the surface polarizability.

A similar effect is known for thin metal films on a substrate for which the transmission coefficient t is given by

$$t = \frac{4n_s}{1 + n_s} \frac{1}{\sigma d Z_0 + n_s + 1}, \quad (3.13)$$

where n_s is the refractive index of the substrate, $\sigma = \varepsilon_0 \varepsilon \omega / i$ is the complex conductivity of the metal film, d is the thickness of the metal layer, and Z_0 is the impedance of free space [18, 65]. For a free-standing metallic film without a substrate Eq. 3.13 is transformed to

$$t = \frac{1}{\sigma d Z_0 / 2 + 1}. \quad (3.14)$$

The last equation is a limiting value of Eq. 2.10 for the film thickness much smaller than the skin depth of the metal. Equations 3.13 and 3.14 clearly demonstrate that in the thin-film limit the film conductivity cannot be obtained independently. Instead the product of $\sigma \cdot d$ determines the electrodynamic properties and could be extracted from experiment. This description works well as long as the film thickness is smaller than both the penetration depth and the wavelength of the radiation.

To demonstrate the ambiguity of the effective SRR thickness for the present metamaterial, the two layer fits have been repeated for various values of the effective thicknesses d_{SRR} . The results of this approach are shown in the insets of Fig. 3.7(a) for the experimental data and Fig. 3.7(d) for the simulation data. The strength of the resonance is shown as a function of the thickness of the metafilm layer (symbols). The other free parameters, like the position and width of the resonance, are nearly independent of the choice of d_{SRR} . As expected from the previous discussion, the development of the resonance strength with the layer thickness shows an inverse proportionality, i.e., $\Delta\varepsilon = A/d_{SRR}$, with A being a constant. This behaviour is demonstrated in the insets of Figs. 3.7(a) and 3.7(d) by solid lines. The values retrieved for the investigated structures are $A = 0.16$ mm for the experiment and $A = 0.17$ mm for the simulations. This proves that for a given metafilm the permittivity alone is not a good parameter for the description, but the product $\chi_e \cdot d_{SRR}$ indeed is. This product remains constant in a large range of parameters and therefore, could be used to characterize the structure.

Since it had been shown now that the normal incidence spectra of the SRR could be well explained using a two-layer model, the behaviour of this model under oblique incidence should be investigated. In this geometry the electromagnetic response of the rings is not only dependent on the dielectric permittivity, but also on the permeability and the bianisotropy. To fully characterize the sample and check the validity of the two-layer model, measurements under two different angles of incidence ($\theta = 30^\circ, 40^\circ$) have been done for the same three samples as above. In addition, also the phase shift of the reflectance has been measured. Therefore, a slightly modified setup of the Mach-Zehnder interferometer has been used (see Fig. 2.3). Due to the anisotropy of the SRRs, there are four measurement geometries for each structure (neglecting the geometries in which the wave vector lies in the plane of the rings). These are indicated in the insets of Fig. 3.9 (a,d). In addition, the bianisotropy of the SRR leads to a field component polarized perpendicular to the incident radiation, *i.e.* the polarization direction of the light becomes rotated. In order to determine this component measurements with crossed polarizers have been made. Since the crossed signal in the reflectance measurements is below the stray signal, only the transmittance measure-

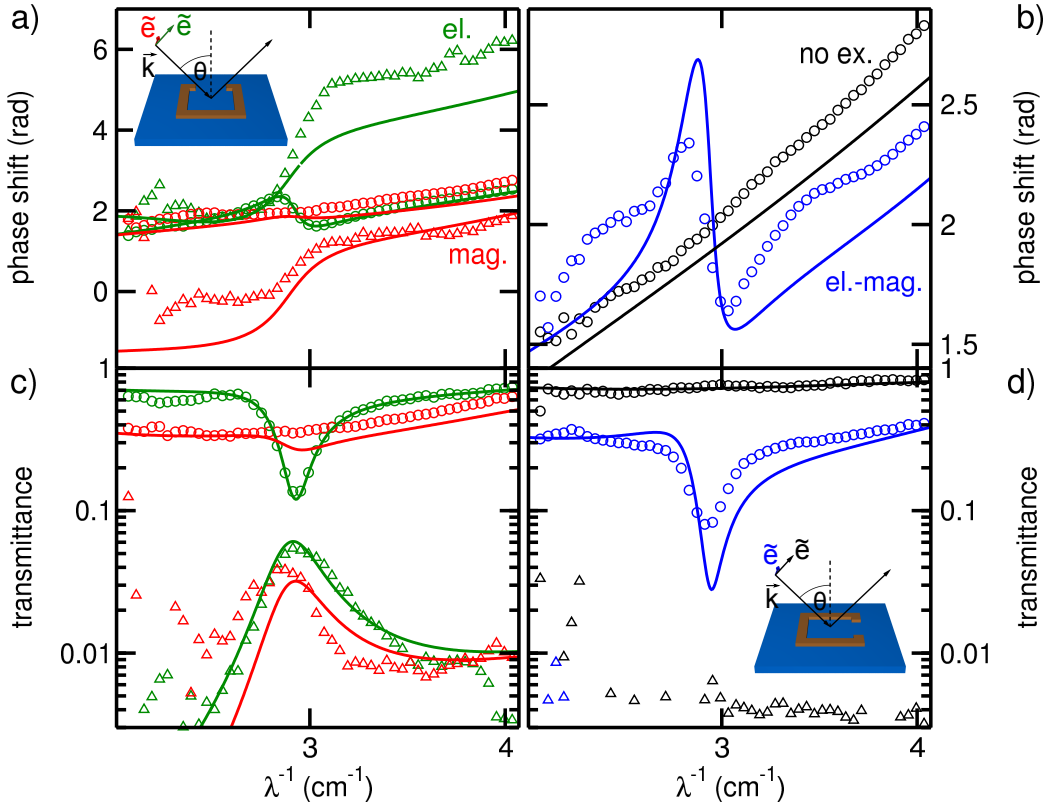


Figure 3.9: Measured phase shift (a,b) and transmittance (c,d) spectra of SRR structures with a gap size of 0.15 mm in the four possible excitation geometries under an angle of incidence $\theta = 45^\circ$. The insets in (a,d) show the respective geometry. Symbols give the experimental data, where the circles correspond to measurements with parallel polarisers and triangles to crossed polarisers (see text for details). The solid lines show fits according to the two layer model. The text denotes the main excitation mechanism.

ments have been done in crossed polarizers. The rotation of the polarization direction is called optical activity and arises normally due to a chirality of the structure. However, the split rings alone are not chiral. The observed effects arise due to an extrinsic chirality resulting from the mutual orientation of the split rings and the incident electromagnetic wave. Previous reports in the literature have studied these effects in more detail [66, 67].

Figure 3.9 presents the phase shift (a,b) and transmittance (c,d) measurements of a sample with a gap width of 0.15 mm at an angle of incidence of 45° . The circles denote the measurements with parallel polarizers, while the

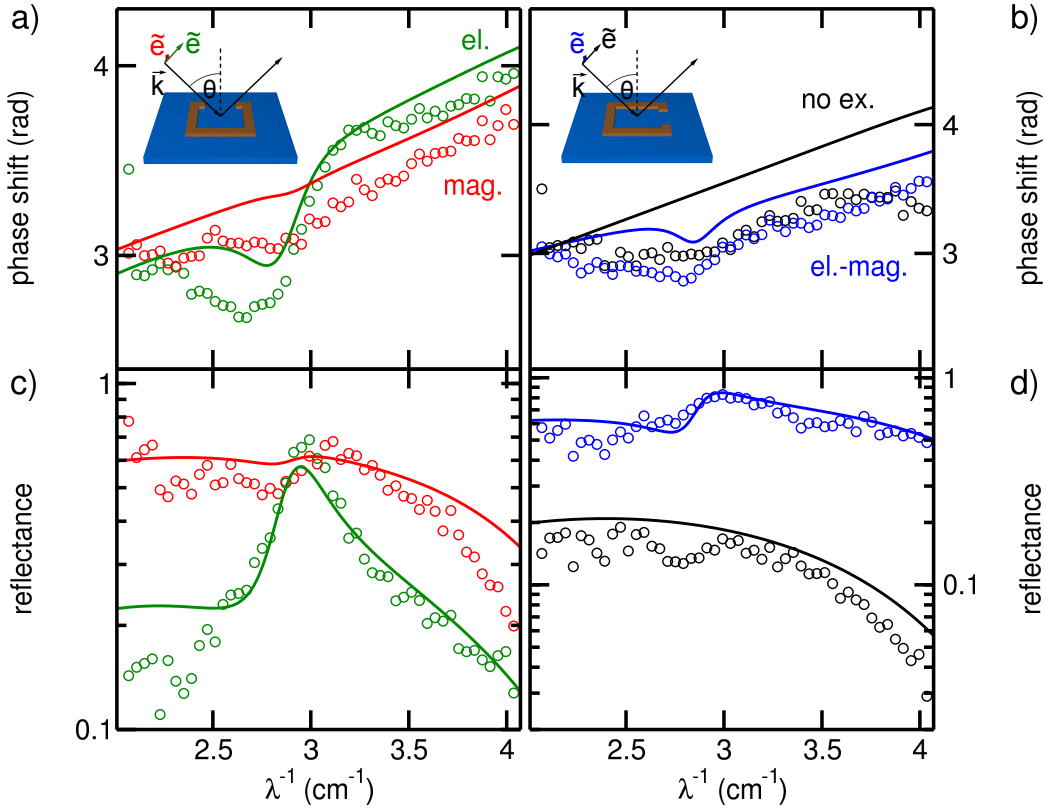


Figure 3.10: Measured phase shift of reflectance (a,b) and reflectance (c,d) spectra of SRR structures with a gap size of 0.15 mm in the four possible excitation geometries under an angle of incidence $\theta = 45^\circ$. The insets in (a,b) show the respective geometry. Symbols - experiment, solid lines - two layer fit. The text denotes the main excitation mechanism.

triangles give the crossed signal. The left panel in Fig. 3.9 shows the measurements in which the SRR are excited only by the electric field (green) or the magnetic field (red), respectively. The right panel demonstrates the excitation of the rings by both the electric and magnetic field component (blue) or the case in which no excitation at all occurs (black).

As can be clearly seen in the left panel of Fig. 3.9 a very well detectable crossed signal occurs in both the electric and magnetic excitation geometries around the resonance frequency of the rings (red and green triangles). The nonzero signal below about 2.5 cm^{-1} is due to a radiation leakage around the sample and can be neglected. Another interesting feature could be seen in the right panel of Fig. 3.9. In the geometry in which the rings are excited

by both the electrical and magnetical field (blue circles) the resonance could be clearly seen in parallel polarizers. However, in this geometry, no crossed signal could be observed (blue triangles). The measured signal is solely a stray signal. Therefore also no phase shift data is shown in Fig. 3.9 (b). Obviously, in the geometry in which the rings are not excited at all, neither a resonance nor a crossed signal could be observed and only the substrate response is measured (black symbols).

Figure 3.10 shows the corresponding reflectance measurements, again for the ring-substrate-system. In Fig. 3.10 (a,b) the reflected phase shifts are given, while (c,d) show the reflectance in the different geometries. Due to the weak crossed signal, which is below the stray signal level, only measurements in parallel polarisers are shown.

The presented experiments in Fig. 3.9 and Fig. 3.10 are fitted using the 4×4 formalism described in Sec. 2.2.2. This formalism allows the calculation of the complex transmittance and reflectance in the tilted geometry as well as in crossed polarizers. Again a two-layer model is used for the description of the spectra, but in opposite to the normal incidence spectra, the full anisotropic parameterset of $\hat{\epsilon}$, $\hat{\mu}$, $\hat{\xi}_{em}$ and $\hat{\xi}_{me}$ has to be used in Eq. 3.1. The matrix form of the effective metamaterial layer is taken as:

$$\hat{\epsilon} = \begin{pmatrix} \epsilon_{SRR} & 0 & 0 \\ 0 & 1 & 0 \\ 0 & 0 & 1 \end{pmatrix}, \hat{\mu} = \begin{pmatrix} 1 & 0 & 0 \\ 0 & 1 & 0 \\ 0 & 0 & \mu_{SRR} \end{pmatrix},$$

$$\hat{\xi}_{em} = \begin{pmatrix} 0 & 0 & -i\xi_{SRR} \\ 0 & 0 & 0 \\ 0 & 0 & 0 \end{pmatrix} \text{ and } \hat{\xi}_{me} = \begin{pmatrix} 0 & 0 & 0 \\ 0 & 0 & 0 \\ i\xi_{SRR} & 0 & 0 \end{pmatrix}, \quad (3.15)$$

for a wave propagating in the z-direction, while the gap of the SRR is orientated along the x-direction. Here again the simple Lorentzian is taken for the permittivity $\epsilon_{SRR} = 1 + \chi_e$ (Eq. 3.8), the permeability $\mu_{SRR} = 1 + \chi_m$ (Eq. 3.10) and for the bianisotropy ξ_{SRR} (Eq. 3.11). The second layer again has been treated as an isotropic frequency-independent substrate with refractive index n_{sub} . Therefore, there are six parameters to fit the experimental spectra

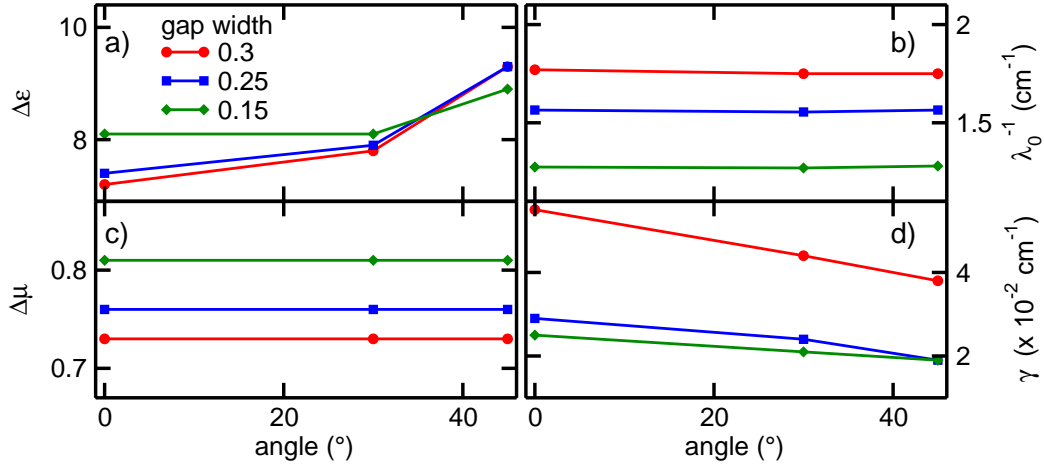


Figure 3.11: Angular dependence of the fit parameters of the two-layer model for SRR with varying gap sizes. (a) shows the dielectric strength, (b) the resonance frequency, (c) the magnetic strength and (d) the width of the resonance. Gap sizes are given in mm.

($\Delta\varepsilon, \Delta\mu, \Delta\xi, \gamma, \omega_0$ and n_{sub}). The results are shown as solid lines in Fig. 3.9 and Fig. 3.10. Due to the different measurement geometries the sensitivity of the theory to the optical parameters differ. In parallel polarizers in the electric geometry (green circles) the response of the rings is mainly determined by the dielectric permittivity. Similarly, the magnetic geometry (red circles) is mostly sensitive to the permeability. The cross-polarised response of the rings (green/red triangles) is mainly given by the bianisotropy of the rings. The right panels of Fig. 3.9 and Fig. 3.10 are now additional measurements which can give further proof of the validity of the proposed model. The best results for the fits were retrieved if the strength of the bianisotropy is coupled to the strength of the permittivity and permeability in the form $\Delta\xi = \sqrt{\Delta\varepsilon\Delta\mu}$. This shows that the SRR is indeed a perfect magnetoelectric and the simple LC-circuit model (Sec. 3.2) holds.

The qualitative agreement between experiment and theory is reasonable good for both the transmittance and reflectance measurements. The two-layer model correctly describes the occurrence of a cross-polarization signal for the electric/magnetic geometry and its absence in the electro-magnetic geometry. But nevertheless some problems remain. While the measurement in the electric geometry in parallel polarizers could be almost perfectly reproduced,

except for some minor deviations in the reflectance, the situation changes for the magnetic geometry. In parallel polarizers the resonance seems to be too strong. But due to the coupling between the resonance strengths, the too high values of $\Delta\mu$ are needed to correctly describe the cross-polarization response of the rings (red triangles in Fig. 3.9 (c)). In addition, the phase jump in crossed polarizers seems to be too small for the electric and too large for the magnetic geometry. But this is just a minor problem and could be explained by experimental difficulties, since the crossed polarizer measurements of the phase shift is rather difficult and sensitive to external errors. The electro-magnetic geometry (Fig. 3.9 (b,c)) again shows a resonance which is too strong, which is caused by the value of $\Delta\mu$ which is too high. Interestingly, in this geometry the agreement between experiment and theory is almost perfect for the reflectance data (blue line/circles in Fig. 3.10). The phase shift in the inactive geometry also shows a slight disagreement between experiment and theory. This effect most probably arises due to the existence of the metallic structures on the substrate, which slightly modifies the refractive index of the substrate and is not covered by the theory. For the phase shifts of the reflectance a slight offset between experiment and theory could be observed in all geometries. This problem arises due to a slightly inaccurate calibration of the spectrometer. But the qualitative agreement between theory and experiment is reasonable. In addition it should be noted that the reflectance measurements were also carried out in the geometry in which the samples were turned by 180° , so the substrate-ring-system has been investigated. The theory also reproduces these spectra within the same accuracy as the shown spectra, which, in addition, points to a validity of the proposed model.

The retrieved fitting parameters for all three samples investigated are summarized in Fig. 3.11 in dependence of the angle of incidence. The retrieved parameters seem to be quite reasonable and consistent between all samples. For all three samples the dielectric strength (Fig. 3.11 (a)) is roughly 10 times stronger than the magnetic response (Fig. 3.11 (c)). But while $\Delta\mu$ stays constant under different angles of incidence for all samples, an angular dependence of $\Delta\varepsilon$ could be well observed. The increase in strength reaches from $\sim 10\%$ for the 0.15 mm sample up to $\sim 30\%$ for the 0.3 mm sample.

Interestingly the growth in the resonance strength seem to get stronger with rising the gap width. The width of resonance (Fig. 3.11 (d)) in opposite decreases for all the samples with increasing angle of incidence. For all samples the width of the resonance reduces about 25% by going to large angles. The resonance frequency (Fig. 3.11 (b)) again remains constant under different angles.

The angular dependence of the retrieved parameters is a drawback for the presented two-layer model, since in a strict physical meaning the effective parameters of a material must be, amongst other things, valid for arbitrary angles of incidence [52]. Hence, the spatial dispersion of the metamaterial can not be neglected and has to be included in theory in order to obtain a better description of the response of the rings.

3.4 Influence of geometry on the electro-dynamics of SRRs

The electromagnetic response of split-ring resonators is determined by its geometrical parameters only, besides the dielectric environment given by the substrate. Although the influence of different sizes has in part already been discussed in literature [68, 69], this section gives a brief overview of the effects the various magnitudes have on the response of the SRR and can serve as a design guideline for building SRR samples with desired properties. Figure 3.12 recalls the various definitions necessary for the description of the SRR's response. Important sizes are the arm length (l_x, l_y), which determines the overall size of the rings, the gap width (g), the metal thickness (t) and the arm width (w). In addition, the unit cell size (s_x, s_y) has a big influence on the properties of the rings. It has to be noted, that this work only focusses on SRRs with quadratic shape ($l_x = l_y = l$) and

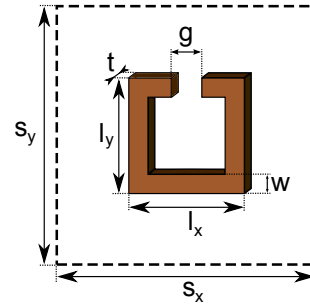


Figure 3.12: Schematic view of a SRR unit cell with definitions of the geometrical parameters.

quadratic unit cell ($s_x = s_y = s$). Studies of SRRs with rectangular shape [34] and rectangular unit cells [70] can be found in literature.

In this section the influence of the different parameters is studied systematically. Therefore, in the following paragraphs one parameter will be varied, while all the others are kept constant. The resulting spectra are analysed using the two-layer formalism presented in the previous section. This section mainly focusses on simulated data and, if available, also experimental data will be shown. All data presented in this section is obtained under normal incidence, so the SRRs are excited electrically. The analysis is limited to the fundamental LC-mode of the SRRs since this mode is most interesting for possible applications. The starting point for the sizes of the SRRs investigated are (unless otherwise noted): $l = 0.4$ mm, $g = 0.15$ mm, $w = 0.05$ mm, $t = 0.02$ mm and $s = 0.9$ mm. For the substrate a frequency independent refractive index of $n_{sub} = 1.90 + 0.07i$ has been assumed. The thickness of the substrate in all cases is 0.48 mm.

In order to understand the behaviour of the SRR with changing parameters one can again fall back on the simple LC-circuit model (Eq. 3.2). Therefore, one needs some analytical model for the capacitance and inductance of the rings. The capacitance is mainly determined by the gap g of the ring. In order to model this capacitance different possible approaches are thinkable, like plates, tips or cylinders. However, the best agreement to the experimental data was achieved using a model of two metallic spheres separated by the distance g . Hence, for the capacitance the following equation can be used:

$$C = 2\pi\epsilon_0\epsilon_r D \left(1 + \frac{D}{g}\right), \quad (3.16)$$

where $D = (t + w)/2$ is the diameter of the spheres and ϵ_r the relative dielectric permittivity arising due to the substrate. For the inductance, the inductance of a quadratic conductance loop with circular cross section has been assumed [71]:

$$L = 2l\mu_0 \left(\ln \left(\frac{4l^2}{Dl(1 + \sqrt{2})} \right) + \frac{D}{2l} - 2 + \sqrt{2} \right), \quad (3.17)$$

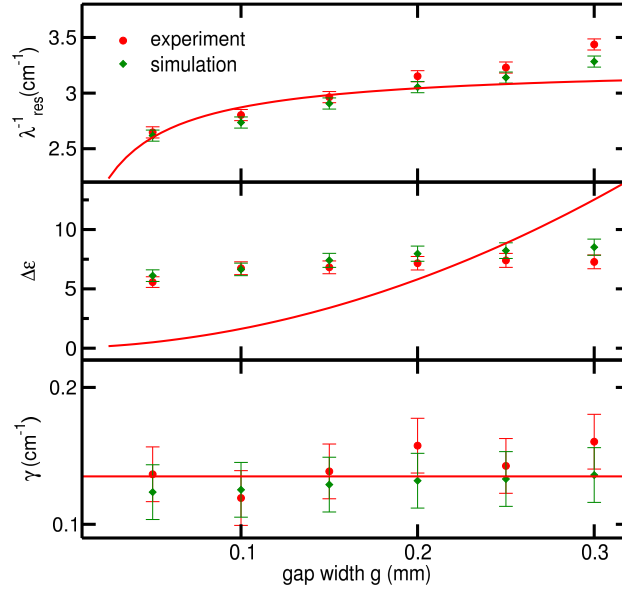


Figure 3.13: Fitparameter from the two-layer model for different gap widths for experimental (red) and simulated (green) SRRs. (a) resonance frequency, (b) resonance strength and (c) resonance width. Solid lines in (a) follow the analytical model presented in the text.

using the definitions from Fig. 3.12 and $D = (t + w)/2$ again the diameter of the metal. From this analytical expressions the resonance position, strength and width can be calculated using Eq. 3.5 and 3.8.

Gap width (g)

The first varied parameter is the size of the gap. Some example spectra of SRR with varying gap sizes have already been shown in Fig. 3.7 for experiment (a-c) and simulation (d-f). Figure 3.13 shows the resonance frequency (a), resonance strength (b) and resonance width (c) obtained from a two-layer fit. It can be clearly seen that with rising gap the resonance frequency blue shifts. This can be easily understood using Eq. 3.16. With increasing distance the overall capacitance of the SRR decreases. Therefore, the resonance frequency increases. The solid lines in Fig. 3.13 give the expected behaviour from the analytical model. In order to get an as good as possible agreement between the analytical model and the experiment, the diameter of the spheres in Eq. 3.16 had to be reduced about 20%. As can be clearly seen in Fig. 3.13

(a) the analytical model then reasonably reproduces the experimental and simulated data. Just for high values of the gap the analytical expressions underestimate the resonance frequency slightly. However for the resonance strength (Fig. 3.13 (b)) the prediction of the analytical model does not reflect the experimental/simulated data well. Although the order of magnitude and basic behaviour (increasing strength of resonance with increasing gap width) of the model are correct, the characteristics strongly differ in detail. In principle the increase in strength could be understood, since the coupling of the electromagnetic field to the rings increases with increasing gap size. But the difference between the model and the experiment shows that the model is too simple and just can predict the behaviour qualitatively. The resonance width (Fig. 3.13 (c)) is independent of the gap size. Following Eq. 3.8 the resonance width is given by $\gamma = R/L$. The resistive losses of the SRRs are mainly determined by the losses in the substrate, which will be shown in the substrate paragraph of this section, and therefore does not depend on the gap size. The inductance of the ring (Eq. 3.17) is also independent of the gap distance. Thus, no dependence of the resonance width from the gap distance is expected, which can clearly be observed in Fig. 3.13 (c). The influence of the gap width on the Q-factors of the structure is rather small. At a gap width of 0.05 mm a Q value of 19 is obtained, while at 0.3 mm it slightly rose to 21.

Arm length (l_x, l_y)

In this paragraph the arm length of the SRRs is varied. The gap size is fixed at $g = 0.15$ mm. In order to keep the coupling between the different rings constant the unit cell size has to be increased with the arm length. The distance between the single rings is kept constant at $50 \mu\text{m}$. Figure 3.14 shows the simulated transmittance spectra of the different rings. It can be clearly observed that a red shift of the resonance frequency occurs while increasing the arm length, which is also the expected behaviour. Due to the increasing arm length the area of the rings increases and therefore also the inductance grows which leads to a reduced resonance frequency. This behaviour is analyzed in more detail in the inset of Fig. 3.14. The solid line again represents the analytical model and it can be clearly seen, that the model fits the sim-

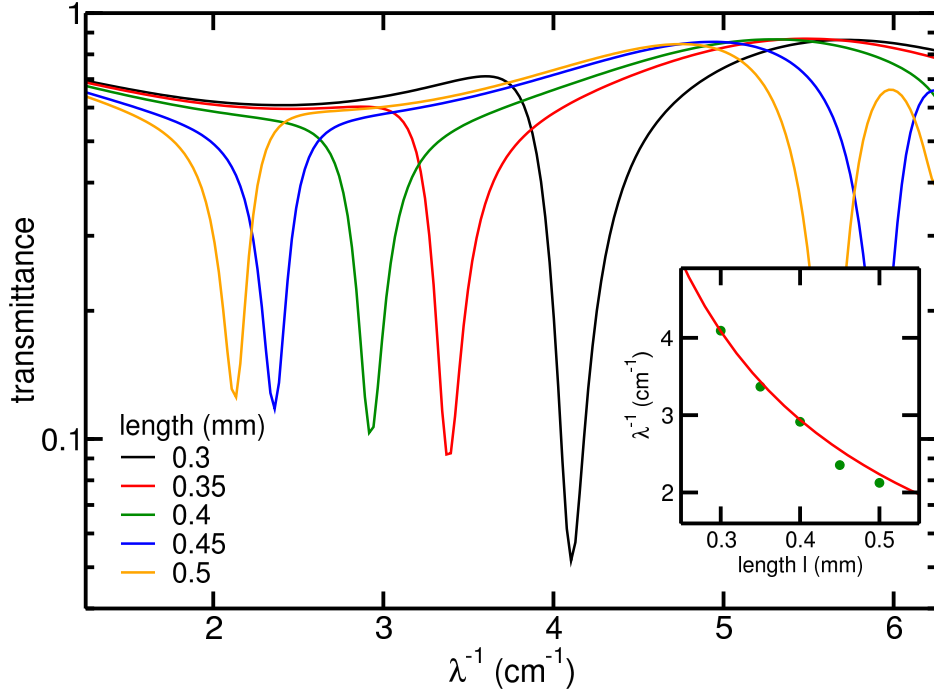


Figure 3.14: Simulated transmittance spectra in dependence of the arm length of the SRR. Inset shows the dependence of the resonance frequency from the arm length (symbols). The solid line in the inset follows the analytical model presented in the text.

ulated data almost perfectly. But for the resonance strength and width this changes drastically. Although the spectra suggest that the strength of the resonance decreases with increasing arm length, the actual behaviour is opposite. So, with increasing arm length the resonance strength increases (not shown). The effect which can be observed in the spectra arises due to the Fabry-Pérot resonances of the substrate, which leads to the seeming decrease of the resonance strength. But at this point the analytical description completely fails. As can be seen in Eq. 3.8 the inductance does not enter in the resonance strength at all. Moreover due to the growing unit cell size the analytical model proposes a decreasing resonance strength for bigger rings. This fact obviously contradicts the simulated results and shows that this simple analytical model is not sophisticated enough to describe all the effects seen in experiment/simulation. This also holds for the characteristics of the resonance width (not shown). In this case, the model proposes a decrease of the width due to the increase in inductance of the rings. The simulated result

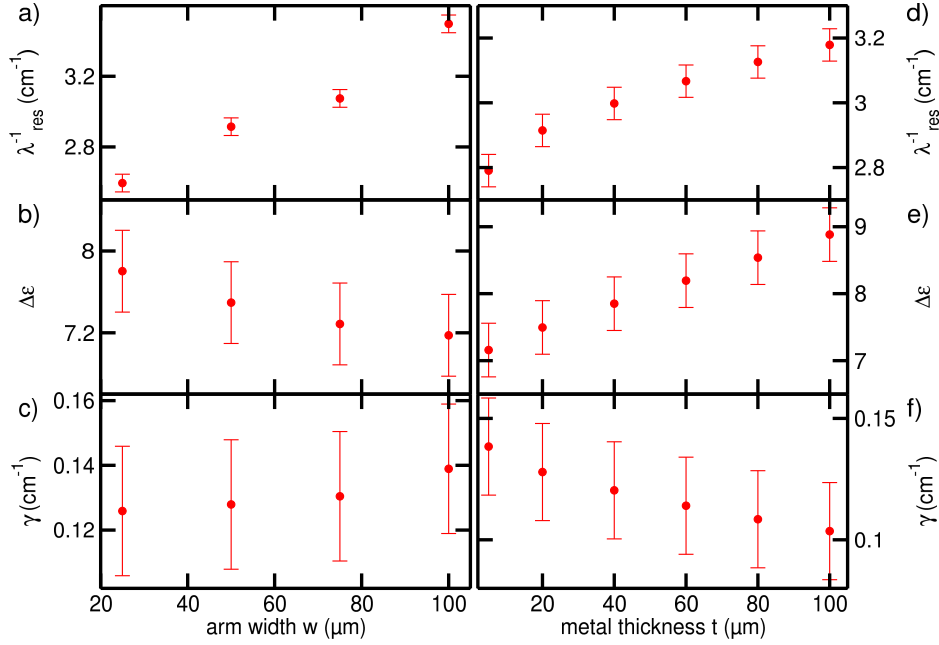


Figure 3.15: Fit parameter of simulated spectra in dependence of the arm width, (a)-(c), and metal thickness, (d)-(f). (a,d) give the resonance frequency, (b,e) the resonance strength and (c,f) the resonance width.

again shows the direct opposite. While increasing the arm length, there is a slight growth of the resonance width. Due to the large red shift of the resonance frequency with increasing side length, also the Q-factor of the structure changes significantly. At 0.3 mm a Q-factor of 35 is obtained, which is cut in half to a value of 15 at a side length of 0.5 mm.

Arm width (w) and metal thickness (t)

The arm width and the metal thickness of SRRs are mostly determined by the production technique and are therefore minor parameters. Nevertheless their influence on the resonance properties should be briefly discussed for sake of completeness. Since in the simple analytical model they enter through the diameter in both the spherical capacitance and the metal cross section, the model is not suitable to describe the resulting effects when varied. Therefore no analytical curves will be shown here. Figure 3.15 shows the resulting resonance frequency (a,d), strength (b,e) and width (c,f) for varied arm width (left panel) and metal thickness (right panel). For both pa-

rameters the resonance frequency increases with increasing parameter. Both parameters influence both the inductance and capacitance of the rings and lead to an increasing resonance frequency when increased. This is consistent with previously reported studies in the literature [68, 69]. The strength of the resonance behaves differently while changing the two parameters. An increased value of the arm width leads to a diminished strength, whereas for an increased metal thickness the strength increases. The width of the resonance behaves oppositely. The increase of the arm width leads to higher values of the width, while it decreases with increasing metal thickness. Although the changes in the resonance strength and width show a definitive trend for both parameters, it has to be noted that the absolute changes are rather small and hardly exceed their errors. However, an appropriate choice of the metal thickness and arm width can be used to fine tune the resonance frequency of the rings. In addition, the variation of these parameters also leads to some changes in the obtained Q-factors. For varying arm width the changes are small and values between $Q_w(25 \mu\text{m}) = 21$ and $Q_w(100 \mu\text{m}) = 25$ are obtained. The metal thickness in opposite shows a slightly larger effect, the Q-factor rises from $Q_t(5 \mu\text{m}) = 20$ to $Q_t(100 \mu\text{m}) = 31$.

Unit cell size (s_x, s_y)

The resonance properties of SRRs strongly depend on the size of the unit cell. This has been widely discussed in the literature, for example in Refs. [70, 72, 73]. Nevertheless, there are some interesting properties, especially with respect to the previously discussed two-layer model. Figure 3.16 shows the simulated transmittance (a) and reflectance (b) spectra of SRRs with varied unit cell size. The distance between the single rings ranges from $4 \mu\text{m}$ ($s = 0.48 \text{ mm}$) up to $44 \mu\text{m}$ ($s = 1.28 \text{ mm}$) in this study. With changing the distance between the single metamaterial constituents one changes the coupling/interaction between them. This leads to several effects which can be seen in Fig. 3.16. The increasing resonance strength can be easily explained due to the increasing density of the rings. The denser the metamaterial becomes, the more rings are excited which leads to a deepening of the resonance. A more interesting effect is the blue shift of the resonance due to the increased density. This clearly shows, that there is a strong in-plane inter-

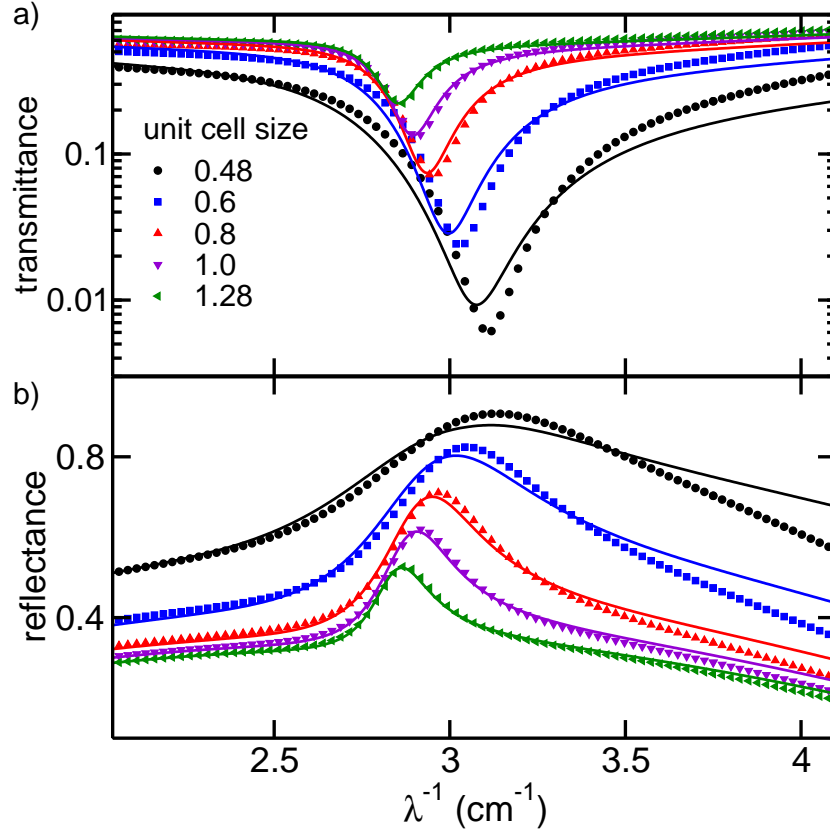


Figure 3.16: Simulated transmittance (a) and reflectance (b) spectra of SRR with different unit cell sizes. Solid lines show the two-layer fit. Unit cell sizes given in mm.

action between the single constituents which was neglected in the previous discussions. This effect has been studied in detail by Sersic *et al.* [70]. They have shown that this blue shift mainly arises due to a transversal coupling of the magnetic dipole moments of the single rings. Although some electric dipole interaction is also present in these structures, the main coupling mechanism in the quadratic unit cell can be described by an inductive one. This leads to the observed blue-shift of the resonance when the density of the rings is increased.

From the previous discussion the general behaviour of the data can be reasonably explained. But the most important point of this paragraph is another one. The solid lines in Fig. 3.16 show again the fits within the two-layer model. As can be clearly seen, the fits work very well for small densities

($s \leq 0.8$ mm) but become very inaccurate if the material is too dense. It has to be noted that the fits presented in Fig. 3.16 consider both the transmittance and reflectance data. If just the transmittance is considered, also the two-layer model can give a more accurate result, while worsening the fit of the reflectance data and vice versa. This shows the limitations of the presented two-layer model. The behaviour can be well expected since the model completely neglects any interaction between the rings. To some extent the effects arising due to the coupling of the rings are caught by an adjustment of the parameters of the model, which can be seen at the low density data in Fig. 3.16. However, at higher densities this approach fails. Therefore for highly dense samples of SRRs a more sophisticated model is necessary for an appropriate description.

Substrate

Now all geometrical parameters have been discussed regarding their influence on the resonance properties of the SRRs. But in addition to the geometrical parameters, there is also another possibility to manipulate the properties of the SRRs which is the substrate. In order to determine the influence of the substrate simulations have been done in which first a pure real refractive index of the substrate is assumed, which will be varied. This is shown in Fig. 3.17. Here two main features are prominent. On the one hand the resonance undergoes a red-shift if the substrate permittivity is increased. On the other hand the resonances are remarkably narrow in comparison to the previously shown spectra which is a consequence of the lossless substrate. The width of the resonance in all cases is below 10^{-3} cm^{-1} , leading to very high Q-values between 1000-10000. Since there are no losses in neither the metal nor the substrate theoretically a value of zero is expected. However, the simulation has a finite resolution leading to a non-zero value of the resonance width. In addition, it has to be noted that the large noise in the spectra with $\text{Re}(\varepsilon_{sub}) = 5$ (green line) above 3.7 cm^{-1} arises due to numerical instabilities and does not have any physical meaning.

The shift of the resonance is analysed in more detail in the inset of Fig. 3.17. Here the resonance frequency is shown in dependence of the substrate

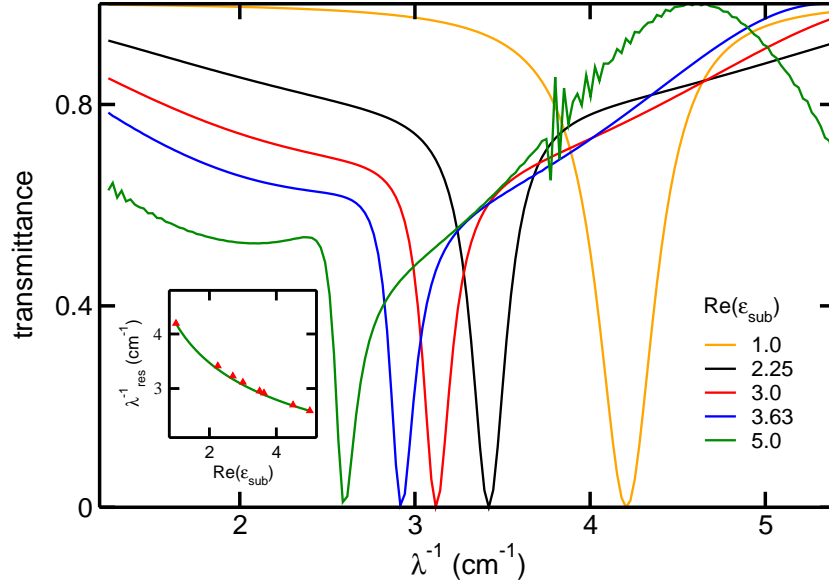


Figure 3.17: Simulated frequency dependent transmittance of SRRs for different (real) values of the substrate permittivity. The inset shows the dependence of the resonance frequency from the substrate permittivity. Solid line in the inset follows Eq. 3.18.

permittivity. The solid line in the inset follows the equation

$$\lambda_{res}^{-1}(\varepsilon_{sub}) = \frac{\lambda_{res}^{-1}(1)}{n_{avg}}, \quad (3.18)$$

where $n_{avg} = (1 + \sqrt{\varepsilon_{sub}})/2$ is the averaged index of refraction resulting from the dielectric environment of the ring and $\lambda_{res}^{-1}(1)$ is the resonance frequency without any substrate. As can be seen in the inset of Fig. 3.17 this relation describes the development of the resonance frequency almost perfectly. This property now has interesting consequences for the metamaterial, as it allows an alteration of the resonance frequency, after the material has been build by simply changing the refractive index of the substrate by external parameters. This can be realized for example by using temperature [74] or optical pumping of the substrate [75]. In addition this feature can be used by depositing an additional material on the air-interface of the rings to change the dielectric environment, which is useful for sensor applications.

In Fig. 3.18 the influence of the substrate losses on the resonance properties

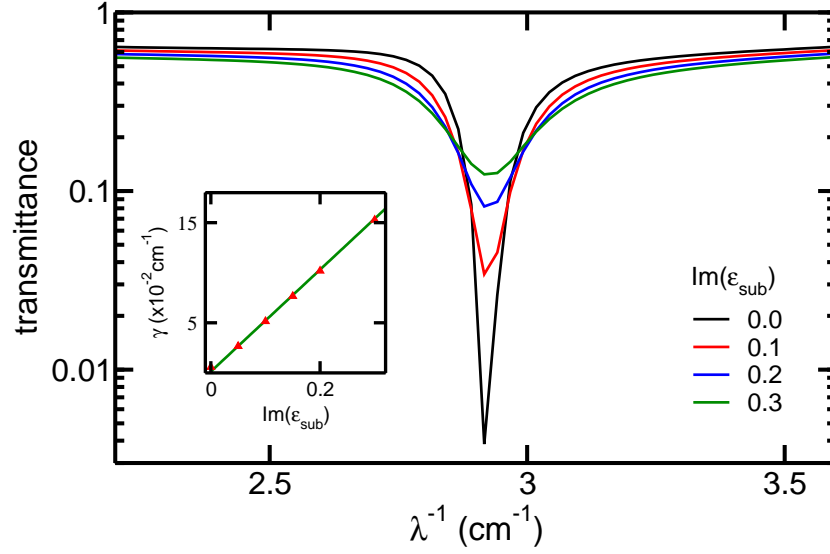


Figure 3.18: Simulated frequency dependent transmittance of SRR for different values of the substrate absorption ($Im(\epsilon_{sub})$). Inset shows the dependence of the resonance width from the substrate absorption.

can be seen. Here simulated transmittance spectra are shown where the imaginary part of the substrate has been varied (with $Re(\epsilon_{sub}) = 3.63$). While the resonance is very sharp for a lossless substrate ($Q > 1000$), the resonance gets wider as the losses are turned on, leading to Q -factors of around 20 (at $Im(\epsilon) = 0.3$ like in the real substrate used). This is shown in more detail in the inset of Fig. 3.18. It turns out that there is a nice linear dependence between the width and $Im(\epsilon_{sub})$. Therefore the substrate is very important regarding the Q -factor of the SRRs. For high- Q metamaterials substrates with losses as small as possible are necessary. On the other parameters, like position and strength, the losses of the substrate do not have any effect.

Another conclusion which can be drawn from Fig. 3.18 regards the conductivity of the metal used for building the SRR-structures. All the simulations shown are using a perfect conducting metal. The simulated data and the actual experimental data coincide regarding the resonance width/strength which can be seen in Fig. 3.7, which means that the used copper can be regarded as perfect, at least in the sub-mm frequency range and for a lossy substrate. In this case, the dielectric losses in the substrate are much larger than the ohmic losses in the metal. Therefore, effects like the finite conduc-

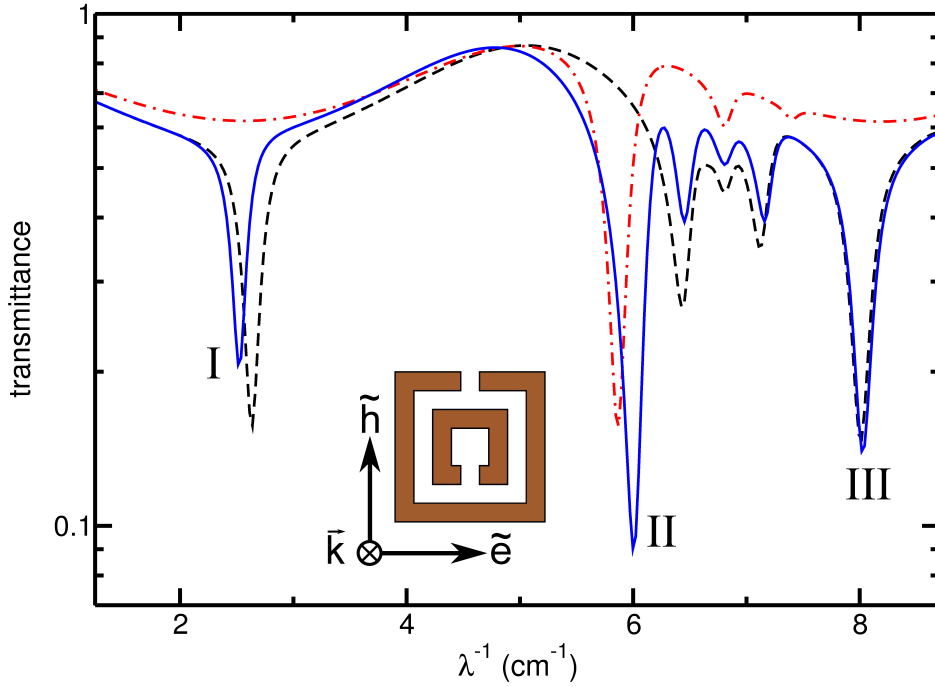


Figure 3.19: Transmittance spectra of the DSRR structure (solid blue line). Black dashed line and red dashed-dotted one show the response of the individual outer and inner ring, respectively. Inset shows the excitation geometry.

tivity or skin-effect can be neglected without losing too much accuracy. The resonance width is mostly determined by the losses in the substrate and not the ones in the metal in this case. However, for lossless substrates the finite ohmic resistance of the metal will be the limiting factor in reaching high Q -values. The effect of the metal conductivity has been studied in Ref. [37]. There it has been shown, that there is indeed an effect on the performance of the material, although being small for high conductivity metals like Cu or Ag.

Double split ring resonator

This section will discuss the basic properties of double split-ring resonators (DSRRs), like they are shown in Fig. 3.1 (b), since in the next chapter experiments on superconducting DSRs will be shown. This structure consists of two concentric split rings, whose gaps are oriented in opposite direction. In order to get a better understanding of this structure, first their basic

properties and the difference to the single rings will be discussed. In order to do this, simulations of this structure have been done. The outer ring is $0.4 \times 0.4 \text{ mm}^2$ in size, while the inner ring is $0.2 \times 0.2 \text{ mm}^2$. The width of the metal, the gap in and the distance between both rings are all $50 \mu\text{m}$. The size of the unit cell is $0.9 \times 0.9 \text{ mm}^2$. As dielectric substrate again the woven glass ($n_{sub} = 1.90 + 0.07i$) is used.

The blue solid line in Fig. 3.19 shows the transmittance spectra of the DSRR structure in the excitation geometry shown in the inset. As can be clearly seen, the response shows three main excitation modes, at 2.5 cm^{-1} , 6.0 cm^{-1} and 8.0 cm^{-1} between 1 cm^{-1} and 9 cm^{-1} , labelled by I-III. Between $6.3 - 7.5 \text{ cm}^{-1}$ additional excitations are visible. These arise due to the periodicity of the structure, *i.e.* they are strongly dependent on the choice of the unit cell size. However, these are unimportant for the following considerations and are therefore neglected in the further discussion.

In order to clarify the origin of the main excitations, additional simulations have been conducted. In this simulations the response of the outer and inner ring have been calculated separately from each other. The results are shown in Fig. 3.19 as dashed black line (outer ring) and dashed-dotted red line (inner ring), respectively. The origin of the different modes is now obvious. The modes I and III arise due to the outer ring. The low frequency mode is the fundamental LC-resonance, while the higher frequency one is the first plasmonic resonance. The plasmonic resonance is the same as already seen in Fig. 3.2, when the exciting electric field is oriented perpendicular to the gap. However, in this geometry the resonance is slightly broadened and red-shifted, since here two side length are present per unit cell which leads to an enhanced dipolar coupling [76]. In addition, also the excitations between $6.3 - 7.5 \text{ cm}^{-1}$ due to the periodicity of the structure are visible here. The mode II in opposite is the fundamental resonance of the inner ring. However, when both rings are combined to the DSRR structure, the resonance frequencies of the fundamental modes are slightly shifted due to the coupling between both rings. The mutual coupling between the rings also leads to some minor changes regarding the strength of the modes. The Q-factors, however, are not significantly altered in the combined structure. For the outer and inner ring

Q-factors of 22 and 53 are obtained, respectively. In the DSRR structure the Q-factors for the first two modes are 23 and 50 and therefore quite similar to the separated single rings. Hence, the presence of the second ring opens up another magnetically excitable mode, while leaving the main properties of the structure unchanged.

3.5 Summary

In conclusion, the basic properties of split-ring resonators have been studied in this chapter. SRRs represent a very interesting material, since they show a strong magnetic response, which can lead to a negative permeability, although consisting of non-magnetic materials. Furthermore, they are bianisotropic which opens up another possibility of controlling the propagation of light. A simple (R)LC-circuit model has been presented, which can be used to describe the electromagnetic response of this material, when excited by either the electric or magnetic field component of the radiation. This simple model suggests that for SRRs in the inequality $\chi_{me}\chi_{em} \leq \chi_e\chi_m$ the equality sign holds, *i.e.* they provide a perfect magnetoelectric material. Measurements under oblique incidence show, that this relation is indeed fulfilled for SRRs.

A big issue in metamaterial research is the proper homogenization of effective parameters, especially for single layer materials. Using normal incidence transmittance and reflectance experiments, it has been shown, that the concept of bulk averaged permittivity is clearly broken for the split rings under investigation. However, it has been demonstrated that a simple two layer model, using an effective permittivity, can describe the response of a metafilm quite accurately. The effective two-dimensional permittivity defined as a product $\chi_e \cdot d_{SRR}$ becomes a new parameter governing the electrodynamics of the split ring metamaterial. In order to further study the validity of the proposed model also experiments under oblique incidence have been made. The presented two-layer model can also be used to describe these experiments with reasonable accuracy. However, it turned out, that the retrieved parameters are slightly dependent on the angle of incidence. This indicates that a spatial dispersion has to be included in a rigorous model.

As a final part in this chapter the influence of the different geometrical parameters on the electrodynamic response of the rings has been studied. The major parameter for controlling the resonance frequency is the arm length of the rings, as can be expected. The gap width turned out to be the second important parameter to influence the resonance frequency and can be used to fine tune the response of the structure. A simple analytical model was presented to calculate the properties of the structure. This simple model can be used for calculation of the resonance frequency of the rings, however, fails at predicting the resonance strength and width of the resonance. Here, a more sophisticated model is necessary. The coupling between the rings also strongly influences the response of the rings, leading to a blue shift of the resonance frequency and widening of the resonance. Since this coupling is neglected in the two-layer model, the description of the rings using this model fails at highly dense samples. In addition, it was shown that the dielectric properties of the substrate are also of major importance. Especially the dielectric losses in the substrate highly influences the performance of the structures. For high Q-factor metamaterials lossless substrates are very important. As an introduction to the next chapter the properties of double split-ring resonators were discussed. It was shown that their behaviour can be understood by the response of the separated outer and inner ring, respectively. However, the coupling between the both rings leads to a small shift of the resonance frequencies.

Chapter 4

Optical properties of superconducting metamaterials

4.1 Quality factor in the superconducting state

As it has already been discussed above, the quality factor is an important quantity regarding the performance of metamaterials. In chapter 3 it has been shown that in the sub-millimeter frequency range the ohmic losses of the metal could be neglected since the metal behaves almost perfect. However, as the frequency is pushed higher towards the terahertz and higher ranges, the ohmic losses become prominent and the desired functions may not be implemented by using the current metamaterial design. Thus an urgent problem is to reduce the losses of these materials. In order to achieve these goals different methods had been proposed recently. One possible approach studies the behaviour of metallic metamaterials operating at cryogenic temperatures [77]. Here it has been shown that the Q-factor can be increased by 40% when the normal metal is kept at 1 K. Another approach is the usage of superconducting material instead of an ordinary metal to build the metamaterial. In the THz range a yttrium-barium-copper oxide (YBCO) film has been proposed for this purpose [78]. Although the losses decrease with decreasing temperature experimentally, the surface resistance R_s of YBCO films at 0.1 THz and 77 K is comparable to that of the normal metal [79]. Therefore YBCO may

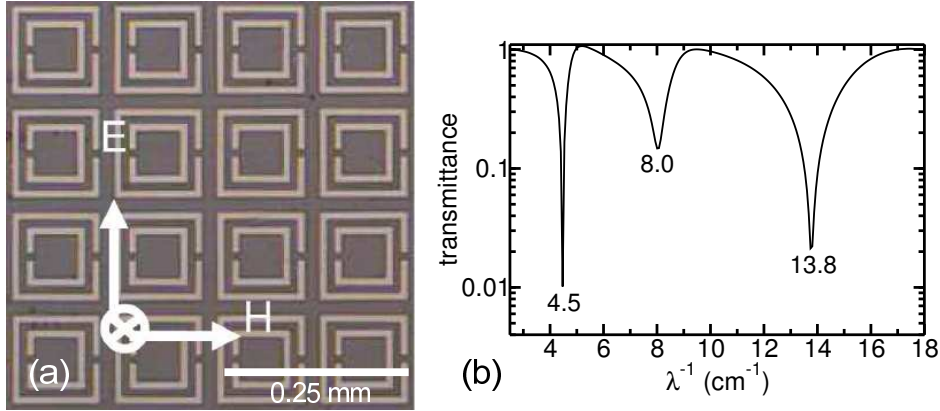


Figure 4.1: (a) Optical microscope image of the sample array and (b) its simulated transmission spectrum.

not be a very good candidate for superconducting THz metamaterials. In this section a metamaterial made of a superconducting niobium (Nb) film is studied, encouraged by the previous report that up to 0.3 THz the R_s value of Nb films at 4.2 K is lower than that of YBCO films by at least one order of magnitude. It will be demonstrated experimentally that upon entering the superconducting state the Q-factor of the metamaterial indeed is increased. Besides, it will also be shown that the superconducting metamaterial can be tuned by applying an external magnetic field. Up to now this tuning has been demonstrated at microwave frequencies [80, 81]. Thus the superconducting metamaterial provides another method to control the wave propagation apart from existing electric [82], optical [83, 84] and thermal tuning methods [85].

For this study a sample consisting of a square array of double split ring resonators (DSRR) has been produced. An optical microscope image of the sample is shown in Fig. 4.1 (a). The DSRR consists of two concentric split rings. The outer one measures $120 \mu\text{m} \times 120 \mu\text{m}$ and the inner one $80 \mu\text{m} \times 80 \mu\text{m}$. The widths of both rings, the spacing between them and their gaps are $10 \mu\text{m}$, while the spacing between the different rings in the array is $20 \mu\text{m}$. Therefore the unit cell is $140 \mu\text{m} \times 140 \mu\text{m}$ in size. The difference between single SRRs and DSRRs has already been discussed and can be found in Sec. 3.4. In order to produce this sample a Nb film is deposited on a $400 \mu\text{m}$ thick high resistivity Si(111) substrate ($n_{Si} = 3.2$) by DC magnetron sputtering. The imaginary part of the refractive index of the Si substrate in the frequency

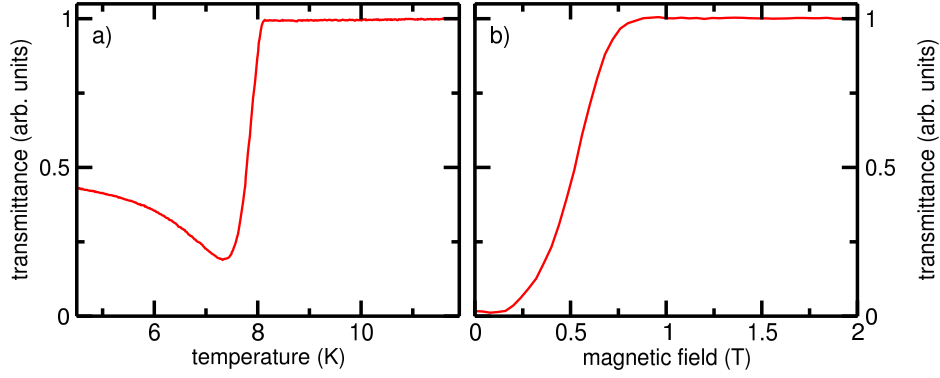


Figure 4.2: (a) temperature and (b) field scan of the superconducting DSRR structure at 4.4 cm^{-1} . Field scan is measured at 6 K.

range of the present experiment was below 1×10^{-4} at all temperatures and could be neglected. The thickness of the Nb film is about 200 nm. The samples were prepared by Prof. Jin Biao Bing from the Research Institute of Superconductor Electronics at the Nanjing University in the People's Republic of China. Single crystal niobium has a body-centred cubic structure, however, the film studied is polycrystalline. The superconducting transition temperature, T_c , of the film is about 9 K, determined by four-probe technique. The sample is then patterned using standard photolithography and reactive ion etching.

The transmittance properties of the sample has been simulated by commercially available code (CST Microwave studio) and are shown in Fig. 4.1 (b). For the simulation the film is assumed to be an ordinary metal with a conductivity of $5 \times 10^7 \text{ S/m}$. The wave is propagating perpendicular to the plane of the DSRR with the ac electric field parallel to the gap of the rings, as shown in Fig. 4.1 (a). In the simulation three resonance modes below 18 cm^{-1} are obtained at 4.5 cm^{-1} , 8.0 cm^{-1} and 13.8 cm^{-1} , respectively.

Before the experimental spectra are analysed, first the characteristic superconducting properties were investigated. In order to do this, temperature and field scans on the already patterned sample have been measured. In this measurement mode the transmitted signal is traced at a fixed frequency as a function of the applied temperature or magnetic field, respectively. The measured signal is not calibrated since only the relative changes are of inter-

est in this measurement. Figure 4.2 shows the temperature (a) and magnetic field scans (b) at a frequency of 4.4 cm^{-1} , *i.e.* in the first resonance mode of the DSRR structure. The measurements have been normalized to the normal state, *i.e.* to temperatures/fields well above the superconducting transition. The DC magnetic field for all measurements is applied in the plane of the rings, so the measurement has been done in the so called Voigt-geometry.

The temperature scan can be used to determine the critical temperature T_c of the structured superconducting film. As can be seen in Fig. 4.2 (a) the transmitted signal has a constant value well above the superconducting transition. Upon reaching the critical temperature the transmitted signal decreases strongly with decreasing temperature. This behaviour is well expected for a superconducting transition and arises due to the large changes in the conductivity of the superconductor [86]. Therefore the critical temperature of the DSRR structure is around 8 K. The slightly reduced value from the bulk value of 9.2 K arises due to the thin film geometry and is commonly seen in high-quality thin Nb films [87]. Therefore the patterning has not significantly altered the properties of the film. Below 7.5 K again a small increase in the signal is observed. This behaviour arises due to a shift in the resonance frequency with changing temperature and will be discussed in more detail in Sec. 4.2.

From the magnetic field scan in Fig. 4.2 (b) the critical field of the superconducting film can be obtained. The field dependence is measured at 6 K. Niobium is a type-II superconductor with upper critical field $H_{c2}(0) = 1.0 - 4.6 \text{ T}$ at low temperatures [88]. According to the temperature dependence of $H_{c2} = H_{c2}(0)(1 - t^2)/(1 + t^2)$ [89], where $t = T/T_c$ and T is the sample temperature, it could be estimated that at 6 K the upper critical field should be in the range between $H_{c2}(6) = 0.4 - 1.8 \text{ T}$. As can be seen in Fig. 4.2 (b) there are almost no changes in very small fields ($H_{DC} < 0.2 \text{ T}$). When the field is increased further the signal begins to increase. At this point the applied magnetic field begins to destroy the Cooper pairs and part of the film becomes normally conducting. Above 0.7 T the changes in the transmittance cease which is a good estimate for the critical field H_{c2} . In comparison to the reported values in the literature for thin films, this seems to be quite a reason-

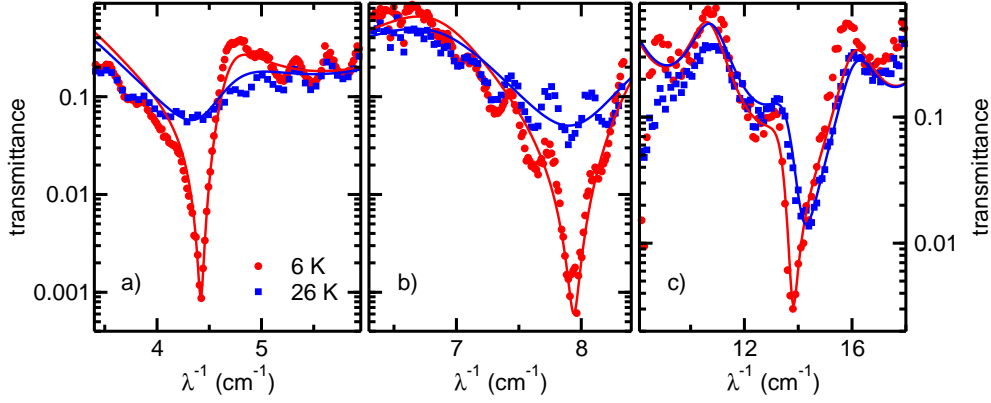


Figure 4.3: Transmittance spectra at 6 K (circles) and 26 K (squares) in the absence of a DC magnetic field for the resonance mode at (a) 4.4 cm^{-1} , (b) 7.9 cm^{-1} and (c) 13.8 cm^{-1} . Solid lines show fits according to Eq. 2.10.

able value. Therefore it could be concluded that both the critical temperature as well as the critical field slightly decrease when the film is structured, but nevertheless very good superconducting properties are obtained.

The experimental spectra are now obtained in the normally conducting state at 26 K, as well as in the superconducting one at 6 K and are presented in Fig. 4.3. The transmittance spectra are obtained in three frequency ranges, covering the three excitation modes of the simulations. Indeed, in Fig. 4.3 (a)-(c) three dips are experimentally observed at 4.4 cm^{-1} , 7.9 cm^{-1} and 13.8 cm^{-1} respectively in the absence of the external magnetic field H_{DC} , just slightly shifted to lower frequencies in comparison to the simulation. At the first glance the spectra already show that all three resonances get much narrower upon entering the superconducting state and therefore the Q-factor highly increases. In order to analyse this increase more quantitatively the spectra were fitted using the two-layer model, Eq. 2.10. For all resonances a Lorentz shape resonance, Eq. 3.8, had been assumed. The fits are shown as solid lines in Fig. 4.3 (a)-(c) and reproduce the experimental data very well. The fit parameters of the model, resonance frequency λ_0^{-1} , strength $\Delta\epsilon$ and width γ , are presented in Table 4.1. From this parameters the Q-factor of the resonances can be easily obtained via $Q = \lambda_0^{-1}/\gamma$ (see Eq. 3.6). The obtained Q-factors are also shown in Table 4.1.

Now the parameters show several effects which occur during entering the su-

Table 4.1: Electrodynamic parameters of the two-layer fits for the three excitation modes in the normally conducting and superconducting state. Values of the sheet resistance R_s are for non-patterned films and are obtained like described in the text.

T	λ_0^{-1} (cm $^{-1}$)	$\Delta\epsilon$	γ (cm $^{-1}$)	Q	R_s (m Ω)
6 K					
	4.42	1800	0.05	88	22 (at 5 cm $^{-1}$)
	7.94	800	0.08	99	29
	13.8	600	0.3	46	63
26 K					
	4.31	1800	0.65	7	200
	7.85	650	0.8	10	200
	14.2	500	0.8	18	200

perconducting state. The first obvious change regards the frequency of the resonances. For all the resonances a slight shift can be observed. This fact will be the topic of the next section and is therefore omitted here for the moment. The resonance strength stays constant within the limits of the errors. The biggest effect can be seen in the width of the resonance. There a large increase can be observed if the structures go from the superconducting in the normal state. This obviously leads to a large decrease in the Q-factor. This result demonstrates that low loss can be achieved as the Nb film is in the superconducting state. The physical reason is clear, because the superconducting Nb film has a lower surface resistance R_s than in its normal state. At 6 K the complex conductivity σ of the Nb film from previous measurements in the literature is about $(2 + 6i) \times 10^5 \Omega^{-1}\text{cm}^{-1}$ at 5 cm $^{-1}$ (close to 4.4 cm $^{-1}$), $(1.6 + 5i) \times 10^5 \Omega^{-1}\text{cm}^{-1}$ at 8 cm $^{-1}$ and $(1.2 + 3i) \times 10^5 \Omega^{-1}\text{cm}^{-1}$ at 14 cm $^{-1}$ [86]. In the normal state just above T_c the resistivity of Nb film is about $4 \mu\Omega\text{cm}$ ($\sigma = 2.5 \times 10^5 \Omega^{-1}\text{cm}^{-1}$). Approximately this value equals the resistivity at 26 K since at low temperatures in the normal conducting state there is just a small temperature dependence in the conductivity of Nb. The complex surface impedance is given by [65]:

$$Z_s = R_s + iX_s = \sqrt{\frac{\mu_0\omega}{i\sigma}} \quad (4.1)$$

The R_s values can therefore be calculated and are summarized in Table 4.1. However, the skin depth in normal conducting niobium ranges between 300 nm (at 4 cm^{-1}) and 150 nm (at 16 cm^{-1}) and is larger as half the thickness of the film. Hence, the electromagnetic field can penetrate the whole film and the film resistance is given by $R_s = 1/(\sigma d)$. According to the R_s values it is obvious that the surface resistance in the normal state is much larger than in the superconducting one. Therefore the superconducting metamaterial made from Nb is a very nice candidate for low-loss devices. However, the change in the surface resistance alone is not large enough to explain the increase in the Q-factor. A second effect leading to an increase in the quality factor can be attributed to the penetration depth of the electromagnetic field in metals. In the normal state the skin depth is larger than the thickness of the film, hence the whole film is penetrated by the electromagnetic field. However, in the superconducting state the penetration depth is reduced to $\approx 90 \text{ nm}$ [86]. Therefore the currents can just flow in two small layers near the surface of the Nb. Effectively this situation is similar to an increase of the metal thickness in a perfect metal. This effect has been already studied in Fig. 3.15 (f), where it has been shown, that an increase of the metal thickness leads to a slight decrease in the resonance width. Hence, the effect of decreased penetration depth also leads to an increase in the Q-factor.

An even better performance of the structure can be obtained if the working temperature is decreased further. However, the losses can not be switched off completely since it is hindered by the residual surface resistance of the film. As the temperature tends to zero, the surface resistance R_s of the film approaches a finite value, the so called residual surface resistance, which is determined by the impurities of the superconducting film. Another obstacle are the radiation losses of the metamaterial. For a given structure these losses can not be reduced and therefore limit the loss performance of these devices essentially. Hence, to get a maximal loss performance the fabrication of high quality films is absolutely necessary. If further improvements are required a careful adjustment of the unit cell geometry could be used to decrease the radiation losses.

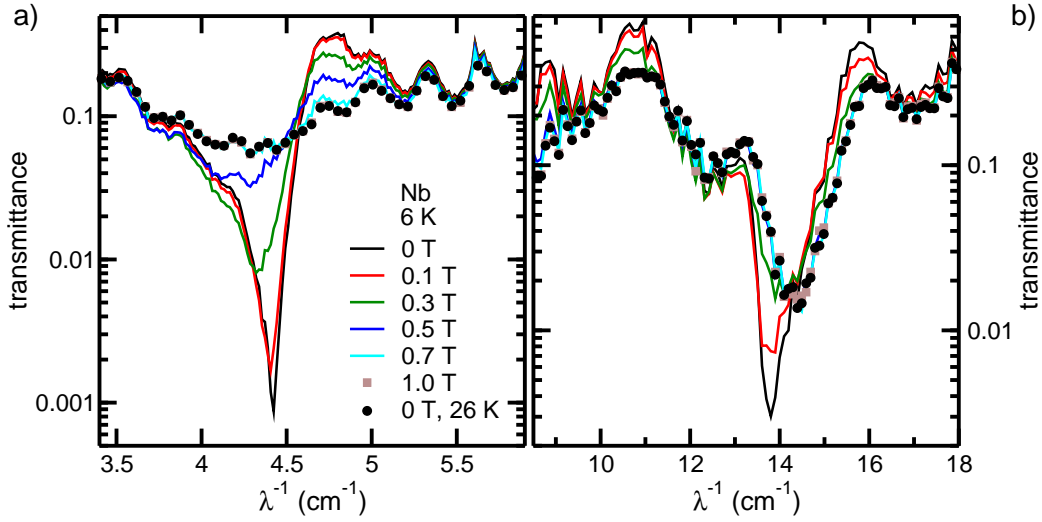


Figure 4.4: Transmittance spectra of the superconducting DSRR at 6 K at different external magnetic fields for the (a) low frequency and (b) high frequency mode, respectively.

4.2 Tunability of the resonance properties by external parameters

As could already be seen in Fig. 4.3 and Table 4.1 the transmission properties of the superconducting metamaterial depend strongly on the temperature. Therefore the temperature is one parameter which can be used to tune the properties of these materials. However, the usage of superconductors opens up another possibility of tuneability. Since superconductors are perfect diamagnets, they strongly react on external magnetic fields. Therefore one could expect that applying a static magnetic field will have an influence on the resonance properties of the superconducting metamaterial. In order to check this assumption, a static magnetic field in the range of 0 – 1 T has been applied to the superconducting metamaterial and the respective transmission spectra had been measured. The magnetic field was applied in the plane of the rings (Voigt geometry). Figure 4.4 summarizes the results of this experiment. Figure 4.4 (a) shows the behaviour of the low frequency mode, while Fig. 4.4 (b) presents the high frequency mode. The intermediate mode at 7.9 cm^{-1} is not shown here since its behaviour is strongly similar to the low frequency mode.

In Fig. 4.4 (a) it can be clearly seen, that the resonance frequency shifts to lower frequencies with increasing magnetic field up to 0.7 T. At higher fields the transmission spectra tend to be the same and the resonance frequency does not change any more. Figure 4.4 (b) shows a similar behaviour for the high frequency mode, except that here the resonance frequency increases with the increase of the magnetic field. The physical reason for this shift in the resonance frequencies are the superconducting properties of the Nb film, like the magnetic penetration depth and critical current density strongly depend upon the external magnetic field. If the external field is large enough, the superconductivity is quenched and the film goes in the normal state. In order to support this argument in Fig. 4.4 (a) and (b) the transmission data for the same sample but at 26 K with no applied external field is also shown. As can be seen in Fig. 4.4 these data closely coincide with the spectra obtained at 6 K and fields higher than 0.7 T. This observation suggests that the upper critical field of the sample is 0.7 T which is consistent with the field scan in Fig. 4.2(b) and also in the expected range from previous reports in the literature as already discussed earlier.

The shift of the resonance frequencies is analysed in more detail in Fig. 4.5. Here, the obtained values for all three modes are shown as a function of the applied magnetic field. The frequencies are again obtained by a two-layer fit and given in GHz for a clearer visibility of the changes. As can be seen in Fig. 4.5 (a,b) for the first two modes the resonance frequency decreases with increasing the applied field. However, for the intermediate mode the stable state is already reached at 0.2 T. For higher fields only changes in the resonance width can be observed up to the critical field. The overall changes in frequency are about 3 GHz for both modes. Figure 4.5(c) depicts the field dependence of the highest mode. In opposite to the first two modes here the resonance frequency rises with increasing field. In addition, the overall changes are about 10 GHz which is much larger than for the low frequency modes.

In order to clarify how the behaviour of the different resonances arises, surface current simulations of the structure have been carried out. These are shown in Fig. 4.6 for the (b) low frequency, (c) intermediate and (d) high

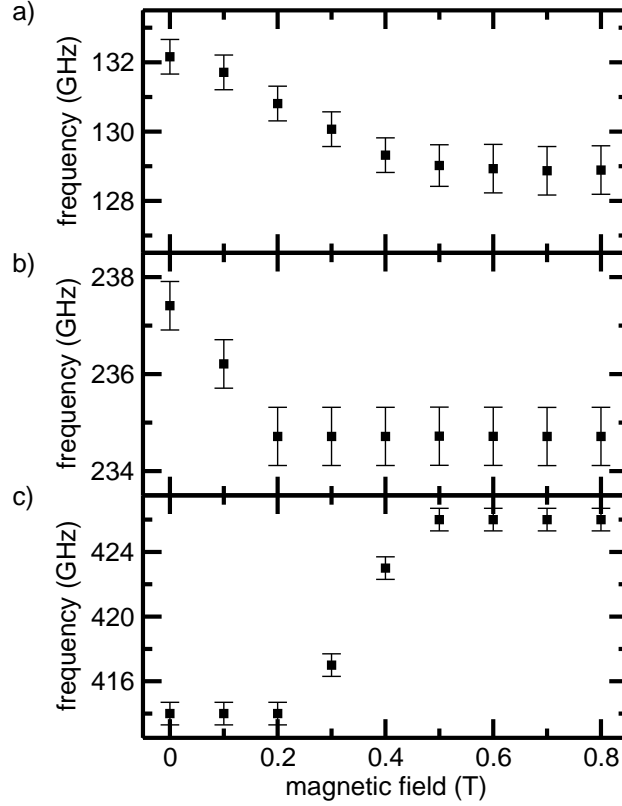


Figure 4.5: The behaviour of the resonance frequency upon applying an external magnetic field for the different modes at (a) 4.4 cm^{-1} , (b) 7.9 cm^{-1} and (c) 13.8 cm^{-1} . For better visibility the frequencies are given in GHz in this figure.

frequency mode. Figure 4.6 (a) gives the simulation geometry. As can be seen in Fig. 4.6 (b) a circular current in the outer ring is excited at the lowest excitation frequency. This is the characteristic behaviour for the excitation of the LC-resonance of the ring, where the gap acts as a capacitance and the ring as inductance. Figure 4.6 (c) shows the same behaviour but here the LC-resonance of the inner ring is excited. This supports again the argumentation about the origin of the different excitation modes of a DSRR in Sec. 3.4. Furthermore this also gives directly the explanation of the origin of the frequency shift for the first two modes. If the ohmic resistance of the metal, from which the SRRs are formed, is considered, the resonance frequency is given by Eq. 3.4. This equation can directly explain the observed effects. With the increasing external magnetic field, parts of the sample become nor-

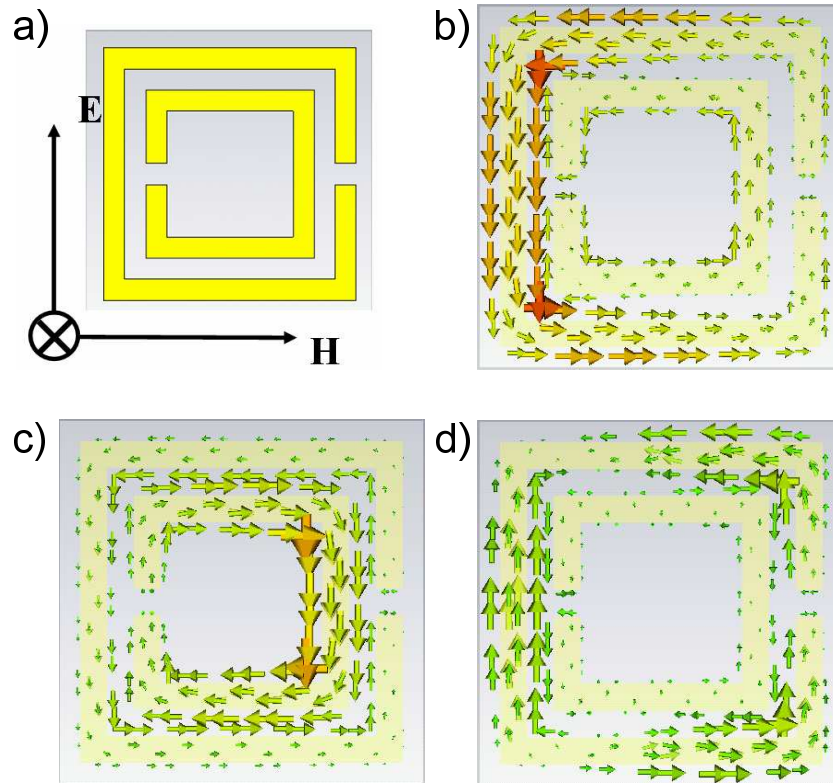


Figure 4.6: The excitation geometry (a) and the surface current distribution for the resonant modes at (b) 4.5 cm^{-1} , (c) 8.0 cm^{-1} and (d) 13.8 cm^{-1} .

mally conducting. Therefore the resistance of the sample rises, which leads to a decrease in the resonance frequency following Eq. 3.4.

For the high frequency mode the situation is different. As can be seen in Fig. 4.6 (d) no circular currents are induced in any of the rings, which means that the resonance is a plasmonic one. The current in the outer ring has the same direction as the one in the adjacent one, leading to attractive forces between them. As the film enters the superconducting state, these attraction becomes larger and the current prefers to distribute in the outer edge of the ring. So the electric length of the outer ring is extended effectively and therefore the resonance frequency is reduced.

In addition, the current distribution in Fig. 4.6 gives another interpretation of the different resonance modes in a split-ring structure. The frequency of the fundamental mode lies at that point, at which half of a wavelength of

the radiation fits in the structure (Fig. 4.6 (b)). Tripling this frequency then leads to the excitation of the $3\lambda/2$ -mode (Fig. 4.6 (d)). On the contrary the $2\lambda/2$ -mode can not be excited by the electromagnetic field, since in this case the charges at both sides of the gap were equal in sign and value.

As a final remark it has to be noted, that the whole tuneability which was shown here by an external magnetic field, could also be realized with the temperature as tune-parameter. The behaviour of all the resonances is exactly the same if the properties of the structure are tuned by the temperature. Therefore all explanations and conclusion drawn throughout this section also hold for the temperature. The superconducting metamaterials can therefore be tuned by two external parameters, the temperature and the magnetic field, which opens up a large usability of these materials.

4.3 Asymmetric SRRs

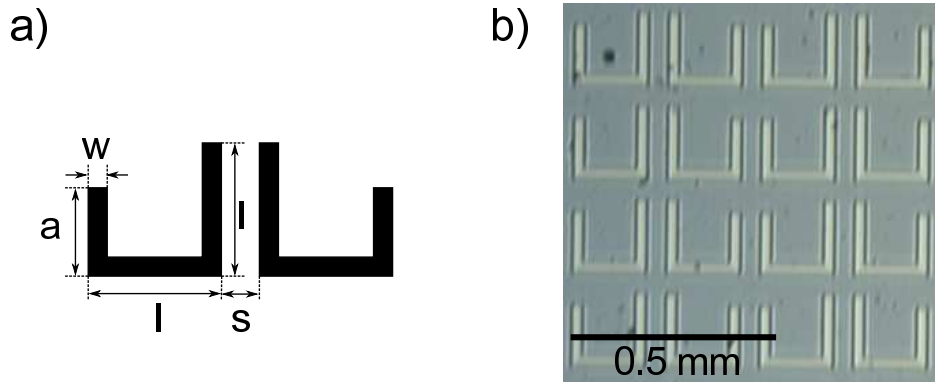


Figure 4.7: a) Schematic unit cell of the asymmetric SRR with the definition of the geometrical parameters, b) microscopic image of the sample

In order to increase the loss performance of a metamaterial two factors have to be reduced. The first one is to reduce the ohmic losses of the metamaterial constituents and has been discussed in Sec. 4.1. The second approach considers the radiation losses which are always present in metamaterials. In order to reduce these losses one has to design the metamaterial constituents carefully. The goal in this design process should be the reduction of the coupling of

the electromagnetic field to the actual structure, which will in consequence lead to reduced radiation losses. A possible realization of such a structure can be created by introducing a certain asymmetry in the unit cell of the metamaterial. Several of such structures have been investigated in the literature. For example in Refs. [90, 91] split rings with two gaps, with different gap sizes, have been presented. Another approach has been shown in Ref. [36] where the gap of the SRR is arranged asymmetrically in the ring. But also the coupling of two rectangular, but otherwise symmetrical, rings with different arm lengths can introduce enough asymmetry to reach a significant effect [34]. All these different approaches lead to a significant increase in the quality factor, which arises due to a reduction of the radiation losses.

In this section another possible approach of reducing the radiation losses is presented. Figure 4.7 (a) shows a schematic picture of the structure under investigation. Here, the asymmetry is introduced by reducing the length of one arm in respect to the other. In order to suppress an undesired circular dichroism the asymmetric ring has been mirrored, so the unit cell consists of two rings arranged in a way like it is shown in Fig. 4.7 (a). A sample with the following geometrical parameters has been produced: $l = 0.18$ mm, $a = 0.15$ mm, $w = 0.025$ mm and $s = 0.05$ mm. The overall unit cell size is 0.46 mm and the metal thickness is about 200 nm. The sample was made of superconducting niobium to reduce the ohmic losses of the structure. As a substrate high resistive silicon (111) ($n_{Si} = 3.2$) was used. The substrate was about 0.4 mm thick. The production details are the same as for the sample in Sec. 4.1 and can be found there. Figure 4.7 (b) shows an actual microscopic image of the sample.

The asymmetric structure now has been studied using temperature and magnetic field dependent transmittance spectroscopy. In addition the asymmetry of the rings opens up a second geometry in which the first (LC-)resonance of the rings can be excited. While in the conventional SRRs the excitation of this resonance is forbidden when the electric field is oriented perpendicular to the gap, their excitation is now possible due to the asymmetry of the arms. Since the coupling of the structure to the electromagnetic field is zero in the symmetric case, it is expected that the small asymmetry leads to a weak

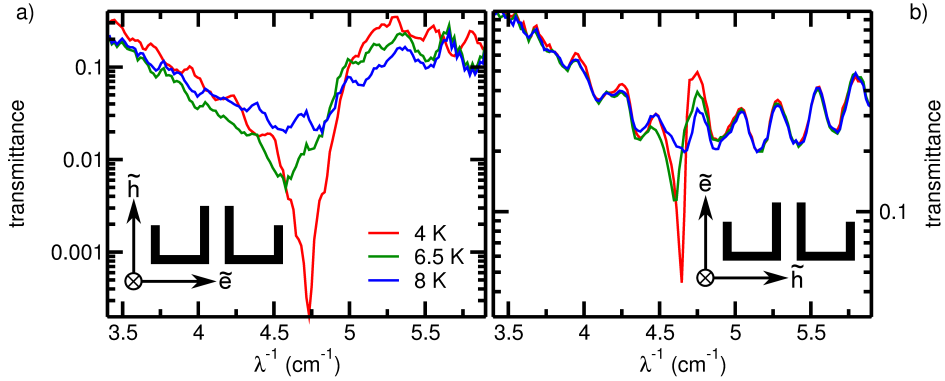


Figure 4.8: Transmittance spectra of the asymmetric split rings in two excitation geometries at different temperatures. a) conventional geometry, b) 90° rotated geometry. Insets show the excitation geometries.

coupling in this geometry. This should result in an even higher Q-factor in this geometry.

Figure 4.8 shows the transmission spectra of the sample at different temperatures. Figure 4.8 (a) shows the geometry with the exciting electric field parallel to the gap, while in Fig. 4.8 (b) the electric field is polarized perpendicular to the gap. In both excitation geometries a clear resonance could be observed. However, the mode strength in the conventional geometry is much stronger than in the perpendicular one. Due to the marginal asymmetry in the studied sample this could be well expected. In addition the resonance is shifted slightly to lower frequencies in the perpendicular geometry compared to the conventional one. In both geometries the thermal tunability of the niobium could be well observed. In this aspect the asymmetric sample behaves like it is expected from the experiments on the DSRR in Sec. 4.2. Here also a decrease in the resonance frequency is observed with increasing temperature. Above 7.5 K no more changes in the resonance frequency/strength could be observed. Therefore it can be assumed that this is the critical temperature of this sample, which is slightly lower than in the DSRR sample. The reason is probably a worse sample quality. The magnetic field tuning is also possible for the asymmetric sample and results in similar spectra as the temperature dependent ones in Fig. 4.8 and therefore are not shown. From the upper critical field data also a slightly worse sample quality could be observed ($H_{c2} = 0.6$ T) compared to the DSRR structure.

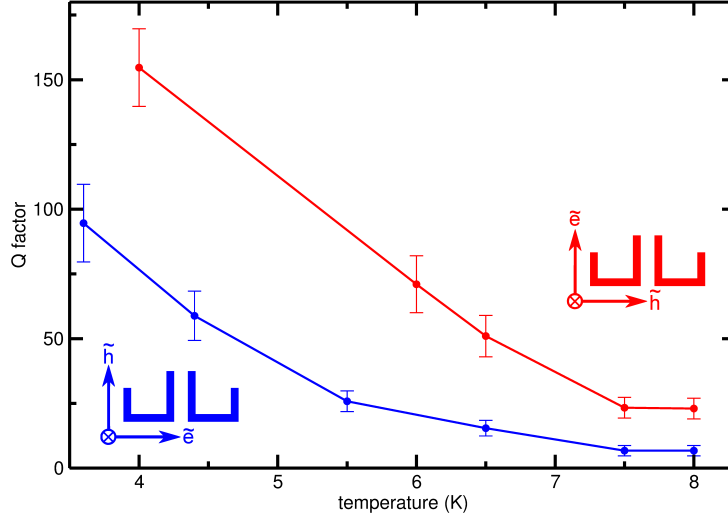


Figure 4.9: Temperature dependence of the Q-factor of the asymmetric split rings in both excitation geometries.

As already shown in Fig. 4.8 (b) the resonance in the perpendicular polarization is very sharp. In order to quantify this, all spectra have been analysed using the two-layer formalism (Eq. 2.10) and from these fits the Q-factors have been calculated. These are summarized in Fig. 4.9 for both excitation geometries. The blue curve shows the temperature dependent Q-factor in the conventional geometry, while the red one results from the perpendicular geometry. As could be clearly seen here, the Q-factor is constant for temperatures higher than the critical temperature ($T > 7.5$ K). Below the critical temperature the Q-factor for both polarizations begins to increase. In the conventional geometry the quality factors are not significantly different from that observed in Sec. 4.1. In this geometry the asymmetry does not influence the performance of the metamaterial device, compared to Sec. 4.1, and only the expected increase due to the superconducting transition could be observed. However, in the perpendicular geometry the situation changes drastically. Here very large values up to 150 can be reached at low temperatures. Therefore the weak electromagnetic coupling between the radiation and the metamaterial structure indeed leads to significantly reduced radiation losses which manifest itself in a very good loss performance of the structure. By further decreasing the asymmetry the coupling of the structure to the electromagnetic field can be further suppressed. Therefore an even better

performance should be obtainable.

4.4 Summary

In conclusion, in this chapter the studies about the possibilities of increasing the loss performance of metamaterials were shown. The properties of superconducting metamaterials made from thin Nb films have been investigated. It has been shown, that the Q-factor of double split ring resonators indeed increase significantly upon the superconducting transition. Values between 50 and 100 can be reached for the simple DSRR design. The reason for the observed behaviour could be attributed to the decrease in the surface resistance of the films. Furthermore, it turned out that the transmission properties of these superconducting metamaterials can be tuned using external parameters like static magnetic field or temperature. It was also shown that the radiation losses of a metamaterial, the second important loss mechanism besides the ohmic losses, could be reduced significantly by carefully designing the unit cell of the metamaterial. Asymmetric split ring resonators were produced from superconducting Nb films in order to make use of the reduced ohmic losses. These samples were studied by temperature and magnetic field dependent transmission spectroscopy. Here the Q-factors up to 150 were obtained. The asymmetric ring design therefore is a very promising candidate for low loss metamaterial devices.

Chapter 5

Optical activity in chiral metamaterials

5.1 Chiral Metamolecules

In this chapter the bianisotropy of the split-ring resonators is used to form chiral quasi-molecules from two inductively coupled SRR layers which, amongst other things, show a huge optical activity. Chirality means, that the structure does not have a mirror symmetry, *i.e.* it can not be superimposed with its mirror image. The layered geometry to build chiral structures has been studied for various different metamaterials [14, 92–94]. The chirality of these structures also opens up another possibility of achieving a negative index of refraction [5, 95–97]. Since first theoretically proposed, this has been experimentally verified for different structures [60, 98–101]. Also a circular dichroism is often observed in these chiral metamolecules [102, 103]. Although there are several interesting effects in these structures, this chapter mainly focusses on the description of the rotary power of these chiral metamolecules built from SRRs.

The main idea of this section is presented in Fig. 5.1, where a unit cell of a chiral metamolecule is shown. It consists of two layers of SRR (with same geometrical parameters) which are separated by a small distance D and rotated

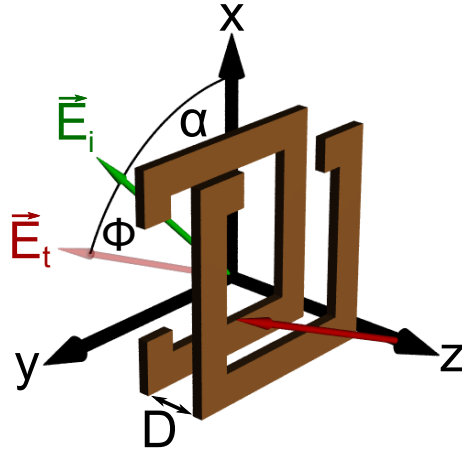


Figure 5.1: Schematic view of a chiral metamolecule created from two layers of mutual twisted SRR-layers separated by a distance D . The chirality of this structure leads to a large optical activity.

against each other by 90° . Now what will happen if electromagnetic radiation is passing through such a structure? Let's assume, without losing any generality, an incident wave linearly polarized along the x -direction ($\alpha = 0^\circ$ in Fig. 5.1) travelling along the $+z$ -direction. If the frequency of the radiation equals the eigenfrequency of the LC-mode of the first ring, this mode will be excited. Due to the bianisotropy of the ring, the excitation of the LC-resonance will create a longitudinal magnetic field polarised along the z -direction. Since the distance between the rings is very small ($D \ll \lambda$) this magnetic field can couple to the LC-resonance of the second ring layer which will lead to an electric field component along the y -direction. Therefore after passing through this metamolecule, the polarization state of the incident light will be modified from linear to elliptical whereas the principal axis of the light will be rotated by an angle ϕ in respect to the incident light.

In addition the coupling of the two resonators results in a splitting of the resonance in two different modes. Qualitatively this behaviour could be well understood in analogy to conventional atomic physics. In this picture the single ring could be seen as single atom (which is justified since all characteristic sizes $a \ll \lambda$) with a defined ground state. If now two of this meta-atoms are strongly coupled a hybridisation of the ground state in a bonding and anti-bonding state will occur like it is the case for hydrogen-like molecules.

This behaviour can be well seen in the experimental spectra.

Similar structures have been studied in the literature in the microwave [104], terahertz [105] and infrared region [106–109].

In order to investigate these properties three different samples were produced as discussed in Ch. 3. The size of the rings in all samples is (for definition see Fig. 3.12): side length $l = 0.35$ mm, gap width $g = 0.13$ mm, width $w = 20$ μm and metal thickness $t = 20$ μm . Two of the samples have the "conventional" unit cell shown in Fig. 5.1 and differ just in the unit cell size ($s = 0.7$ mm and $s = 0.9$ mm) to check the influence of the in-plane coupling on the coupling properties. Since, as will be shown later, the transmission properties of this coupled rings are highly anisotropic, the third sample has a modified unit cell. For this sample a C_4 symmetry has been introduced which leads to an increased unit cell size of $s = 1.8$ mm. A sketch of this symmetrized unit cell can be found in the inset of Fig. 5.8. The two layers were separated by a thin mylar foils (polyethylene terephthalate = PET) in all samples. Unless otherwise noted the thickness of the mylar in all experiments was 50 μm . The substrate for all samples was about 0.5 mm thick, therefore the overall thickness of the samples was around 1 mm (since there is one substrate on each layer of SRR). The samples have been studied by polarization resolved transmittance and phase experiments. In addition, also the polarization state after transmission has been determined by using wire grid polarizers, which allows the direct measurement of the polarization rotation.

5.2 Analysis by transmission matrix formalism

In order to analyze the properties of the chiral metamolecule, the full 2×2 complex transmission matrix of the layered split ring structures is obtained. This matrix fully characterizes the transmission characteristics of the metamaterial structure. Therefore eight independent experimental quantities have been measured for each sample. These are amplitude and the phase of the transmitted radiation for two orthogonal polarizations and within parallel and crossed polarizers. From these quantities the transmission matrix can be

obtained by

$$\underbrace{\begin{pmatrix} T_x \\ T_y \end{pmatrix}}_{\vec{T}} = \underbrace{\begin{pmatrix} t_{xx} e^{i\varphi_{xx}} & t_{xy} e^{i\varphi_{xy}} \\ -t_{yx} e^{i\varphi_{yx}} & t_{yy} e^{i\varphi_{yy}} \end{pmatrix}}_{\hat{M}} \underbrace{\begin{pmatrix} E_x^0 \\ E_y^0 \end{pmatrix}}_{\vec{E}}. \quad (5.1)$$

Here $E_{x,y}^0$ are the components of the incident electric field along the x, y axes, $T_{x,y}$ are the components of the transmitted radiation, $t_{xx,yy}$, $\phi_{xx,yy}$ are the measured transmission amplitudes and phases within parallel polarizers for x, y polarization and $t_{xy,yx}$ and $\phi_{xy,yx}$ are the amplitudes and phases measured in crossed polarizers. After determination of the transmission matrix within x,y coordinates the transmission for an arbitrary polarization can be calculated. For example, the transmission matrix for principal axes rotated by an angle α can be obtained by applying the conventional rotation matrix

$$\hat{R}(\alpha) = \begin{pmatrix} \cos(\alpha) & -\sin(\alpha) \\ \sin(\alpha) & \cos(\alpha) \end{pmatrix} \quad (5.2)$$

to the transmission matrix. For the rotated transmission matrix then

$$\vec{T}(\alpha) = \hat{R}(\alpha) \hat{M} \hat{R}(\alpha)^{-1} \vec{E} \quad (5.3)$$

holds, where \hat{R}^{-1} denotes the inverse rotation matrix. From the transmission matrix for an arbitrary angle the Stokes parameters of the transmitted radiation can be calculated. These parameters are suitable magnitudes for the description of the polarization state of light and are given by [110]:

$$\begin{aligned} S_0 &= T_x^2 + T_y^2, \\ S_1 &= T_x^2 - T_y^2, \\ S_2 &= 2T_x T_y \cos(\delta) \\ S_3 &= 2T_x T_y \sin(\delta), \end{aligned} \quad (5.4)$$

where $T_{x,y}$ are the components of the transmitted electric field $\vec{T}(\alpha)$ and $\delta = \arg(T_y/T_x)$ is their relative phase shift. From this parameters now the

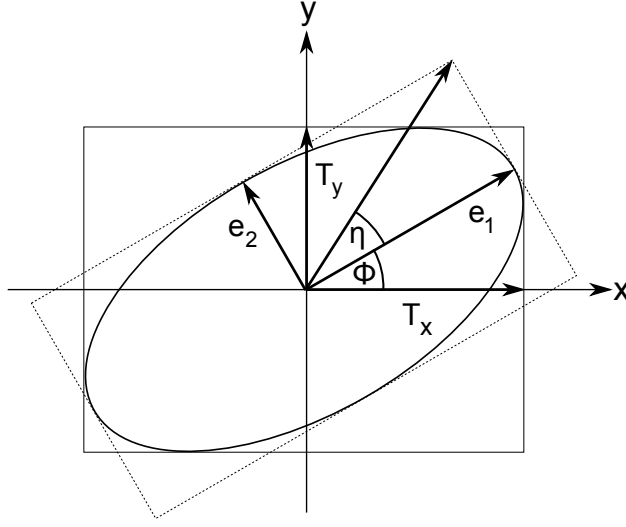


Figure 5.2: Elliptic polarization: Φ denotes the angle of polarization rotation, η denotes the angle between the major (e_1) and minor (e_2) axis of the ellipse and is a measure of the ellipticity of the ellipse.

optical activity Φ , as well as the ellipticity η can be obtained by

$$\begin{aligned}\Phi &= \frac{1}{2} \arctan \left(\frac{S_2}{S_1} \right), \\ \eta &= \frac{1}{2} \arcsin \left(\frac{S_3}{S_0} \right).\end{aligned}\tag{5.5}$$

A graphical description of these parameters can be found in Fig. 5.2. Overall this matrix formalism allows the determination of the optical activity by measurements of the transmittance and phase shift data. This can then be compared to the directly measured optical activity.

5.3 A Lagrangian viewpoint on split-ring coupling

In order to describe the response of the coupled system more quantitatively a Lagrangian formalism can be applied using again the simple LC-circuit

model. The Lagrangian of the uncoupled layer i of SRRs is given by

$$\mathcal{L}_i = \frac{L\dot{Q}_i^2}{2} - \frac{Q_i^2}{2C}, \quad (5.6)$$

with Q_i being the charge accumulated in the gap of the ring in layer i [105]. Here the first term describes the magnetic energy and relates to the kinetic energy of the oscillation. The second one describes the electrostatic energy of the ring and can be understood as the potential energy of the system. For the whole coupled system therefore

$$\mathcal{L} = \frac{L}{2} \left(\dot{Q}_1^2 - \omega_0^2 Q_1^2 \right) + \frac{L}{2} \left(\dot{Q}_2^2 - \omega_0^2 Q_2^2 \right) + M_H \dot{Q}_1 \dot{Q}_2 \quad (5.7)$$

holds. The last term in this equation describes the coupling between the two SRR-layers, with M_H being the mutual inductance of the two layers. In this picture the coupling is assumed to be strictly magnetic. The electric dipole-dipole interaction in this configuration is zero, since the electric fields in the slit gaps of the two layers are perpendicular to one another. The Lagrangian (Eq. 5.7) can now be entered in the Euler-Lagrange equation:

$$\frac{d}{dt} \left(\frac{\partial \mathcal{L}}{\partial \dot{Q}_i} \right) - \frac{\partial \mathcal{L}}{\partial Q_i} = 0 \quad (i = 1, 2). \quad (5.8)$$

Expanding Eq. 5.8 results in a coupled system of equations of motion:

$$\begin{aligned} L\ddot{Q}_1 + \frac{1}{C}Q_1 + M_H\ddot{Q}_2 &= 0 \\ L\ddot{Q}_2 + \frac{1}{C}Q_2 + M_H\ddot{Q}_1 &= 0. \end{aligned} \quad (5.9)$$

Solving Eq. 5.9 using a time harmonic dependence $Q_i = Q_0^i e^{i\omega t}$ leads to the eigenfrequencies ω_{\pm} of the coupled system:

$$\omega_{\pm} = \frac{\omega_0}{\sqrt{1 \mp \kappa}}. \quad (5.10)$$

Here ω_0 gives the resonance frequency of the decoupled system and $\kappa = M_H/L$ the coupling strength between the two layers. This could be directly

determined from the measured spectra, since

$$\kappa = \frac{\omega_+^2 - \omega_-^2}{\omega_+^2 + \omega_-^2}. \quad (5.11)$$

The solution of Eq. 5.9 also shows that the anti-bonding mode ω_+ arises due to an asymmetric charge distribution ($Q_1 = -Q_2$), while the bonding mode ω_- has a symmetric one ($Q_1 = Q_2$).

The coupling strength κ will be dependent on the distance D between the two layers. In order to get a first approximation for this dependence an equation for the mutual inductance is necessary. The mutual inductance between two conducting loops (i,j) is defined analogous to the self inductance and therefore

$$M_{ij}^H = \frac{1}{I_j} \iint_{F_i} \vec{B}_j d\vec{F}. \quad (5.12)$$

It can be easily shown that $M_{ij}^H = M_{ji}^H$ using the magnetic reciprocity. The magnetic field of a quadratic conducting loop (with side length l) in a given distance D is determined by [111]:

$$H = \frac{Il^2}{2\pi\sqrt{\frac{l^2}{2} + D^2}} \left(\frac{1}{\frac{l^2}{4} + D^2} \right), \quad (5.13)$$

where I is the current through the loop. Combining Eq. 5.13 and 5.12 and assuming a constant field distribution throughout the loop leads to:

$$M_H = \frac{\mu_0 l^4}{2\pi\sqrt{\frac{l^2}{2} + D^2}} \left(\frac{1}{\frac{l^2}{4} + D^2} \right). \quad (5.14)$$

Now the coupling strength

$$\kappa = M_H/L \quad (5.15)$$

can be calculated using the inductance of a single ring (Eq. 3.17). Although this model is very simple, a reasonable agreement to the experimental data is obtained (see inset of Fig. 5.4).

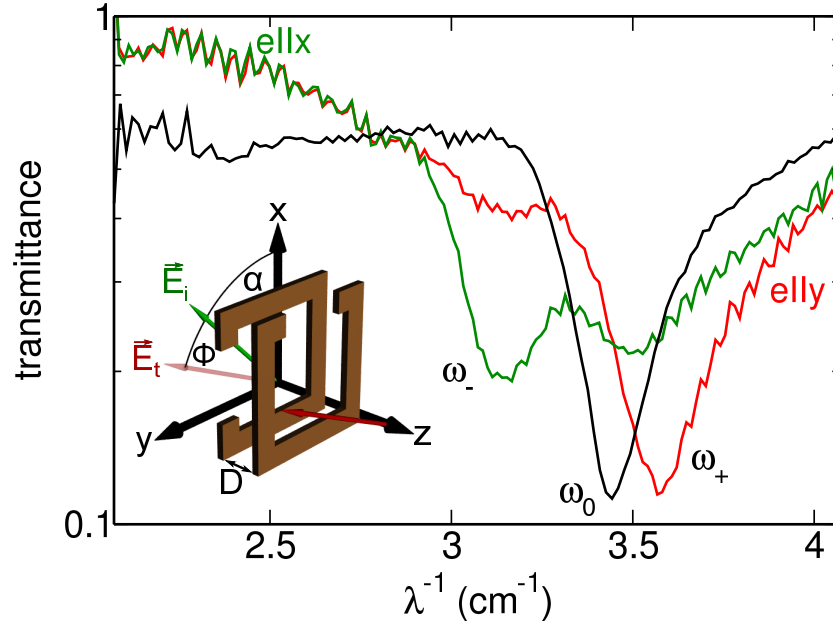


Figure 5.3: Transmittance spectra of inductively coupled SRR with unit cell size $s = 0.9 \text{ mm}$ under different incident polarizations. The inset shows the excitation geometry with $\vec{k} \parallel z$.

5.4 Experimental characterization of coupled SRRs

Now that the theoretical framework of the chiral structures has been depicted, the actual experiments will be discussed. Figure 5.3 shows the transmittance spectra of the sample with 0.9 mm unit cell under two different incident polarizations. The excitation geometry can be found in the inset with $\vec{k} \parallel z$. Unless otherwise noted all transmittance spectra shown in this chapter are measured with parallel polarizers. In addition, also the transmittance spectrum of an uncoupled SRR layer is shown (black line). As can be expected from Eq. 5.10 the uncoupled resonance splits in two resonances (denoted by ω_{\pm} in Fig. 5.3) which can be nicely seen in both excitation geometries. In addition a strong dependence of the transmission properties from the incident polarization could be observed. When the first ring layer gets excited by the electric field (green line), the ω_{-} -mode is much stronger than the higher frequency mode. Otherwise, in the case in which the electric field excites the

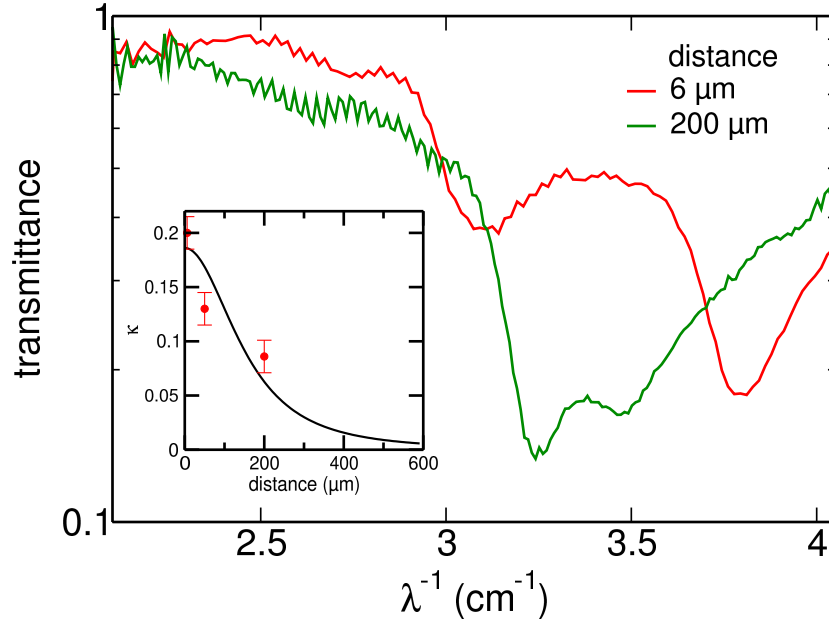


Figure 5.4: Transmittance spectra of inductively coupled SRR separated by $6\ \mu\text{m}$ (red) and $200\ \mu\text{m}$ (green) mylar, respectively. The inset shows the coupling strength in dependence of the layer distance. Solid line - theoretical curve following Eq. 5.14, symbols - experimental data.

second ring layer (red line) the ω_+ -mode is the stronger one. Clearly, simple split ring structures are expected to reveal pronounced anisotropy due to the constructional asymmetry of these metamaterials. This behaviour will be discussed in Fig. 5.5 in more detail.

Figure 5.4 shows the transmittance spectra of structures with different layer spacers. For a better visibility of the splitting the spectrum for the $6\ \mu\text{m}$ is shown with the incident polarization along the y -direction and for the $200\ \mu\text{m}$ sample along the x -direction. The inset of Fig. 5.3 shows the dependence of the coupling strength from the distance between the two split ring layers. In order to realize this experimentally, mylar foils with different thicknesses have been used as spacer layer. In Fig. 5.4 it could be well observed that the coupling decreases with increasing distance, *i.e.* the separation of the ω_{\pm} decreases with increasing layer separation. The solid line in the inset of Fig. 5.3 shows an analytical curve obtained by Eq. 5.15. As can be seen in the figure the simple inductive coupling model resembles the experimental data rather well. It has to be noted that Eq. 5.15 contains no free fitting param-

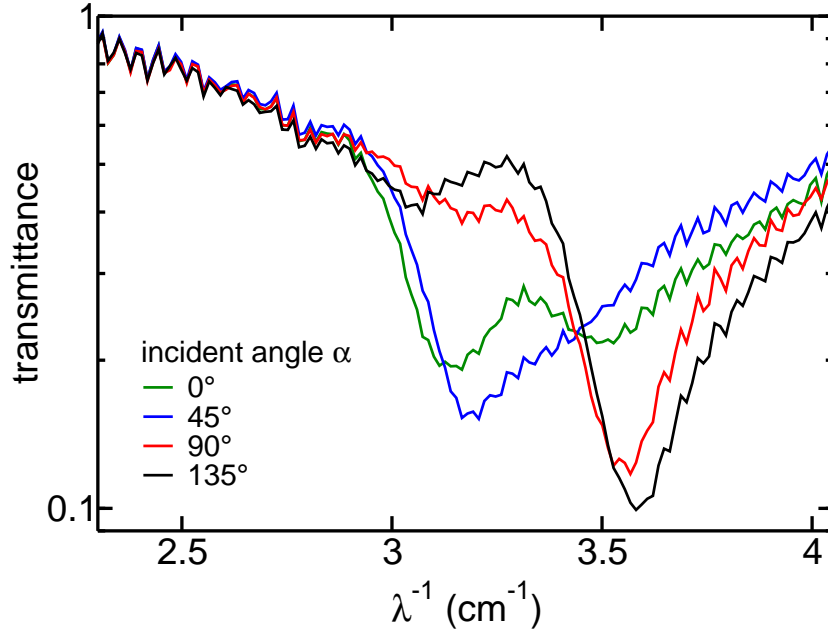


Figure 5.5: Transmittance spectra of inductively coupled SRR under different angles of incidence for the 0.9 mm sample.

eter, nevertheless the experimental values are reasonably reproduced. With increasing spacer thickness the coupling strength decreases as it is expected. Therefore also the splitting of the resonances will decrease until the system is decoupled and the single layer spectra are obtained.

Figure 5.5 shows the behaviour of the metastructure under different angles of incidence. The excitation geometry again is given in Fig. 5.1. Thus, $\alpha = 0^\circ$ corresponds to $\tilde{e} \parallel x$ in Fig. 5.3 and $\alpha = 90^\circ$ to $\tilde{e} \parallel y$, respectively. Here the evolution of the modes can be nicely observed. At $\alpha = 0^\circ$ the ω_- -mode is slightly stronger than the ω_+ one. With increasing the angle the ω_- -mode gains in strength upon reaching its maximum at 45° . At this angle the ω_+ -mode nearly disappeared. If the angle is increased further the situation changes. Now the ω_+ -mode increases in strength while the ω_- -mode begins to decrease. The ω_+ -mode reaches its maximum at 135° . From this behaviour it could be concluded that the principle axes of this structure lie along the $\pm 45^\circ$ direction. A detailed field analysis can for example be found in Refs. [105, 107]. There it has been shown, that the resulting surface currents in the two layers are either in the same (ω_-) or in the opposite (ω_+) direction. Therefore the result-

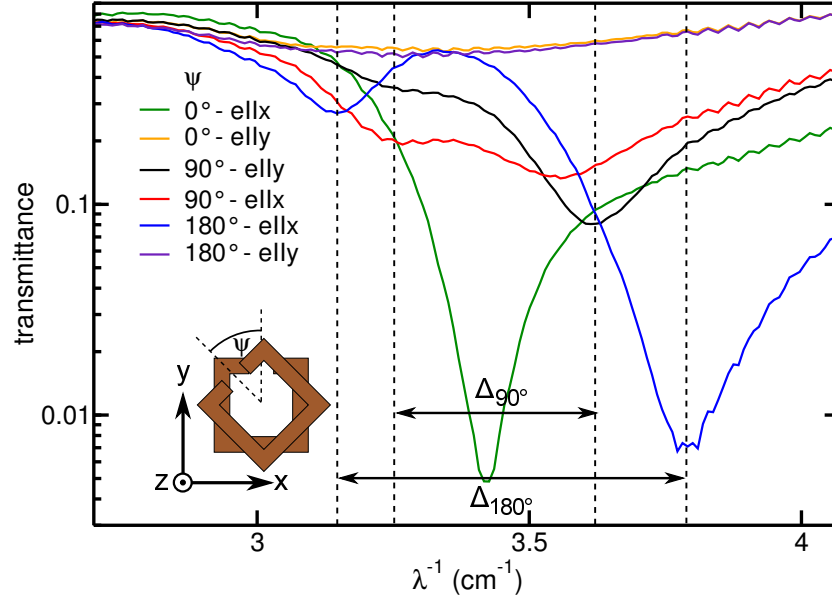


Figure 5.6: Transmittance spectra of inductively coupled SRRs with different twist angles ψ for the sample with 0.7 mm unit cell. The inset shows the excitation geometry and definition of ψ .

ing magnetic dipoles are aligned parallel or anti-parallel, respectively. So the hybridization of the modes in the coupled system arises due to a longitudinal magnetic dipole-dipole interaction between the two layers. By irradiating the coupled system along the principle axis, one can selectively excite the parallel or the anti-parallel mode.

Figure 5.6 shows the dependence of the transmittance spectra on the twist angle ψ between the two layers. As can be clearly seen here, the transmission properties strongly depend on the twist angle. For the parallel orientated sample ($\psi = 0^\circ$) no splitting of the resonance could be observed. Surprisingly a very large hybridization could be seen for the 180° sample. As it is expected no excitation of the structure occurs in the 0° and 180° configuration for y-polarization. To understand this behaviour again the Lagrangian-formalism presented in Sec. 5.3 could be used. If $\psi \neq 90^\circ$ the electric moments of the two layers are not orthogonal anymore. Hence, in Eq. 5.7 also the electric interaction between the two layers has to be considered. This leads to an

extended Lagrangian [106]:

$$\mathcal{L} = \frac{L}{2} \left(\dot{Q}_1^2 - \omega_0^2 Q_1^2 \right) + \frac{L}{2} \left(\dot{Q}_2^2 - \omega_0^2 Q_2^2 \right) + M_H \dot{Q}_1 \dot{Q}_2 - M_E \omega_0^2 Q_1 Q_2 \cos \psi, \quad (5.16)$$

with M_E giving the electric interaction. Here just the electric dipole-dipole interaction has been considered. The contribution of higher order multipoles can be neglected for the twist-angles under consideration and get important just for some intermediate angles [106]. Now solving Eq. 5.8 using Eq. 5.16 leads to the eigenfrequencies

$$\omega_{\pm} = \omega_0 \sqrt{\frac{1 \mp \kappa_E \cos \psi}{1 \mp \kappa_H}}, \quad (5.17)$$

where $\kappa_E = M_E/L$ gives the electric coupling strength. For $\psi = 90^\circ$ Eq. 5.17 reduces to Eq. 5.10 as expected. Now equation 5.17 explains the results seen in Fig. 5.6. So the largest splitting of the resonance can be seen at $\psi = 180^\circ$ since both the electric as well as the magnetic interaction lead to an enhanced hybridization. In addition Eq. 5.17 also leads to the conclusion, that $\kappa_E \approx \kappa_H$ for the structure under investigation, since the splitting in the 0° -sample is below the resolution limit of the spectrometer. Therefore the electric and magnetic coupling nearly compensate each other which leads to a nearly undisturbed resonance.

Figure 5.7 shows the influence of the split ring density on the transmittance properties of the coupled system. For this purpose samples with unit cell size of 0.7 mm (solid lines) and 0.9 mm (dashed lines) have been produced. Black lines in Fig. 5.7 show the single layer response of the two samples. The green and red lines show the spectra of the coupled system for $\tilde{e} \parallel x$ and $\tilde{e} \parallel y$, respectively (excitation geometry can be found again in Fig. 5.1). In agreement to the simulated spectra in Fig. 3.16 the single layer spectra show a red shift of the resonance frequency when the unit cell size is increased as a consequence of the reduction in the in-plane coupling of the rings. Furthermore the resonance is stronger in the denser sample due to the increased number of excited rings. Overall this behaviour could also be observed in the coupled system. But in addition, it could be seen in Fig. 5.7 that the asymmetry of the splitting ($\Delta_+^x < \Delta_-^x$), which already arises due to

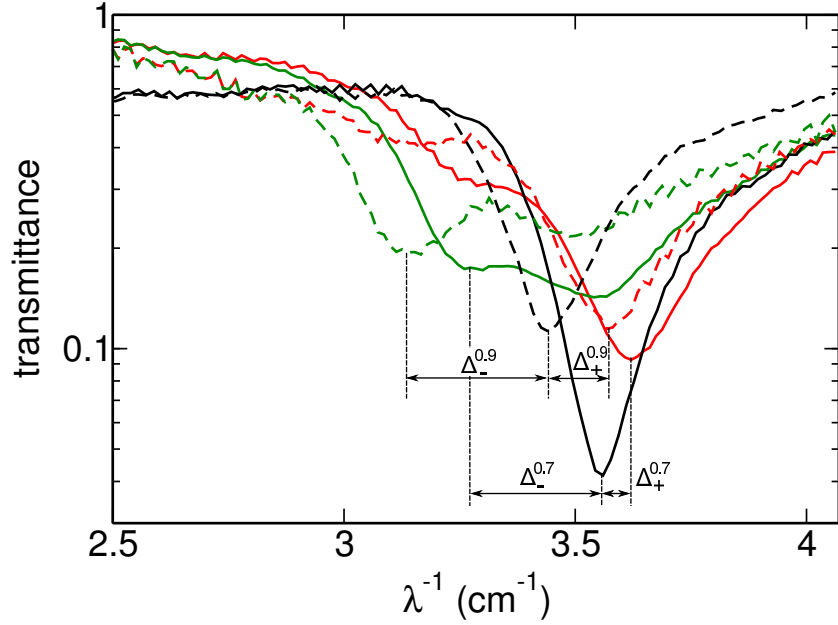


Figure 5.7: Transmittance spectra of inductively coupled SRRs with different densities. Black - single layer, red - $\tilde{\epsilon} \parallel y$, green - $\tilde{\epsilon} \parallel x$, dashed lines - unit cell 0.9 mm, solid lines - unit cell 0.7 mm.

Eq. 5.10, gets stronger if the density of the rings is increased. An explanation thereof can again be provided by the Lagrangian model presented above, if an additional term is introduced which considers the in-plane coupling of the rings. Therefore the new Lagrangian is given by

$$\mathcal{L} = \mathcal{L}_0 - \frac{M_{ip}}{2} \dot{Q}_1^2 - \frac{M_{ip}}{2} \dot{Q}_2^2, \quad (5.18)$$

where \mathcal{L}_0 is the given by Eq. 5.7 and M_{ip} gives the mutual in-plane inductance. Here a pure inductive in-plane coupling has been assumed which is the same in both layers. Solving Eq. 5.8 provides the new eigenfrequencies of the system

$$\omega_{\pm} = \frac{\omega_0}{\sqrt{1 \mp \kappa - \kappa_{ip}}}, \quad (5.19)$$

where $\kappa_{ip} = M_{ip}/L$ is a measure of the in-plane coupling strength. It can be seen that the in-plane coupling leads to an additional increase (decrease) of ω_+ (ω_-). But since κ_{ip} acts in the same direction like κ for the ω_+ -mode, but in the opposite direction for the ω_- -mode the asymmetry of the splitting

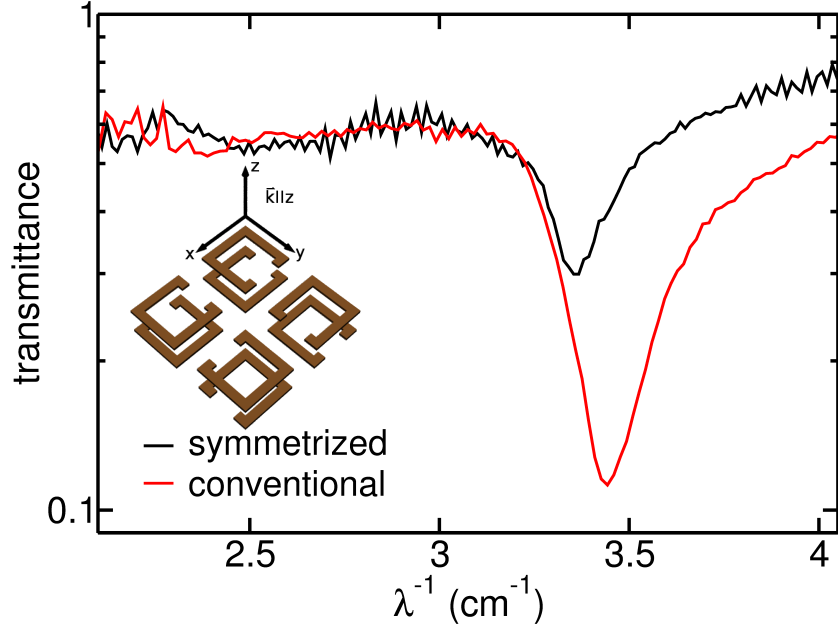


Figure 5.8: Transmittance spectra of a single layer of the symmetrized sample in comparison to the conventional one. Inset shows a sketch of the symmetrized unit cell.

will increase for an increased in-plane coupling. Therefore again the simple Lagrangian model provides a good estimate and explanation of the experimental data. But also it can be seen in Fig. 5.7 that $\kappa_{ip} \ll \kappa$. This could already be expected since the in-plane distance is much larger than the distance between the two layers. Thus, for the most cases the in-plane coupling could be neglected and all further experiments will just be done for one of the samples, namely the 0.9 mm sample.

One point remains open in this section. The response of the coupled system is strongly anisotropic which can be seen in Figs. 5.3 and 5.5 and has already been discussed. But for a possible application this behaviour is highly undesirable. Hence, a sample has been produced in which additional symmetry elements have been introduced in the unit cell. A sketch of this C_4 -symmetric unit cell can be found in the inset of Fig. 5.8. Due to this changes the unit cell size doubled and is 1.8 mm for this sample. All other parameters are the same as for the conventional sample. The single layer transmission properties are shown in Fig. 5.8. For comparison, the single layer transmittance of the

conventional unit cell is shown, too. The symmetrized sample shows a slightly red-shifted resonance frequency as well as a decrease in strength. Both facts could be easily explained by the previous discussion and simply arise due to the smaller effective density compared to the conventional sample, since in the single layer just two of four rings are excited. So besides these well expected changes no unforeseen effects occur.

5.5 Optical activity of inductively coupled metamaterials

Figure 5.9 shows the phase shift (a,c) and transmittance spectra (b,d) for the conventional unit cell (left panel) and the symmetrized one (right panel), respectively. The excitation geometry for both samples is shown in the inset of Fig. 5.9 (b,d). All spectra are measured within two incident polarizations in parallel and crossed polarizers. The parallel measurements (red and green lines) in transmittance (Fig. 5.9 (b)) of the conventional unit cell show the, by now well known, splitting of the resonance with differing strength of the two excitation modes. These resonances can also be well seen in the phase shift data (Fig. 5.9 (a)). The black and blue lines show in addition the measurements in crossed polarizers. Here it can be seen that a large amount of the electromagnetic field is converted to the orthogonal polarization in respect to the incident field when the resonance in the structure is excited. Especially when excited along the y-direction the transmitted intensity reaches 10% which already gives a hint at the large optical activity of these metamolecule structure. When excited along the x-direction the crossed signal is about a factor of three smaller, but nevertheless reaches values around 3% which is still a good detectable signal, since the stray signal outside the resonance (below 2.8 cm^{-1}) lies around 10^{-3} . The phase shift data also shows the large anisotropy. In addition a large jump in the phase shift data can be seen, which was also observable in the crossed polarization measurement of the single layer under oblique incidence (Fig. 3.9).

Figure 5.9 (c,d) shows the same measurements for the symmetrized sample.

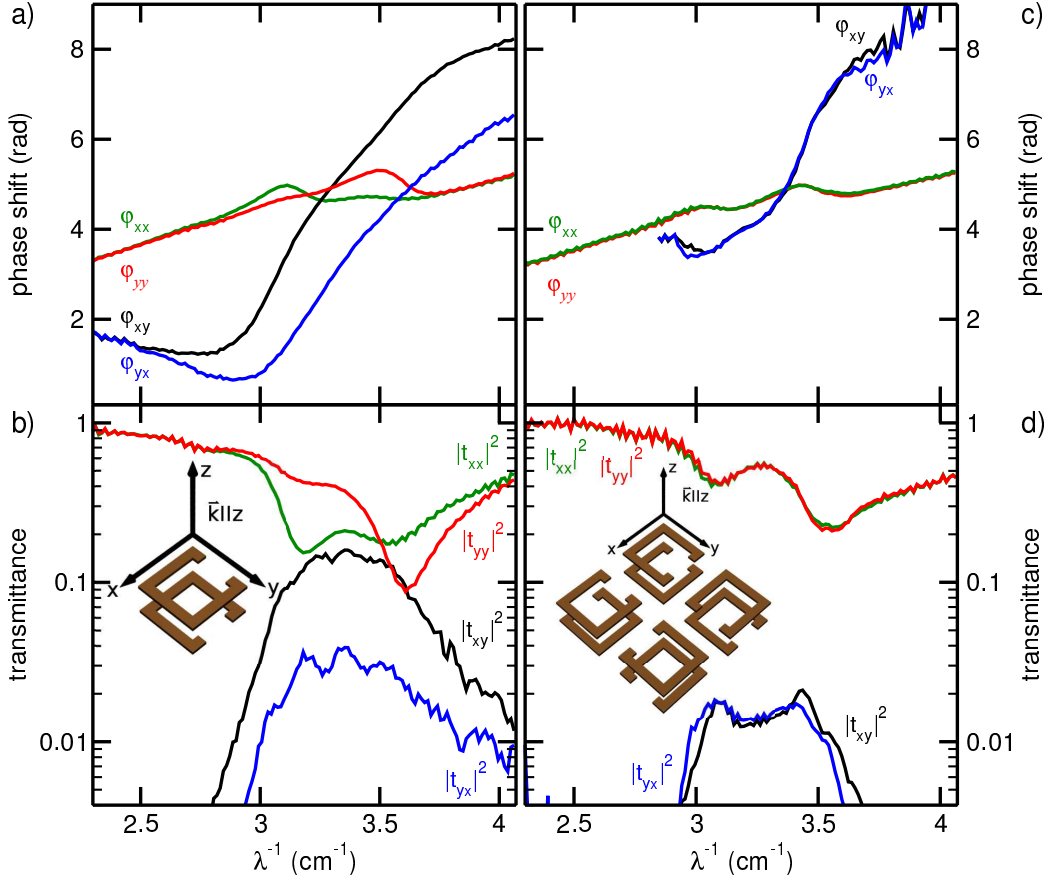


Figure 5.9: Frequency dependence of the measured phase shift (a) and transmittance (b) of the bi-layered structure of SRRs in parallel and crossed polarizers. (c) Phase shift and (d) transmittance of the symmetrized structure. The notation at the curves correspond to the elements of the 2×2 transmission matrix (Eq. 5.1). The insets show the geometrical arrangement of the unit cells.

Clearly, the anisotropy is almost completely removed and the spectra for both polarizations closely coincide due to the presence of the C_4 symmetry. This already indicates at this point that the transmission matrix for the symmetrical geometry is symmetric as well. In this case the angle of the polarization rotation is not expected to depend on the polarization state of the incident beam. But in addition it could also be expected that the optical activity of the symmetrized sample will be smaller than in the conventional sample since the crossed signal reaches just 2%. It has to be noted that the phase shift data for the symmetrized sample is cut off below $\approx 2.9 \text{ cm}^{-1}$.

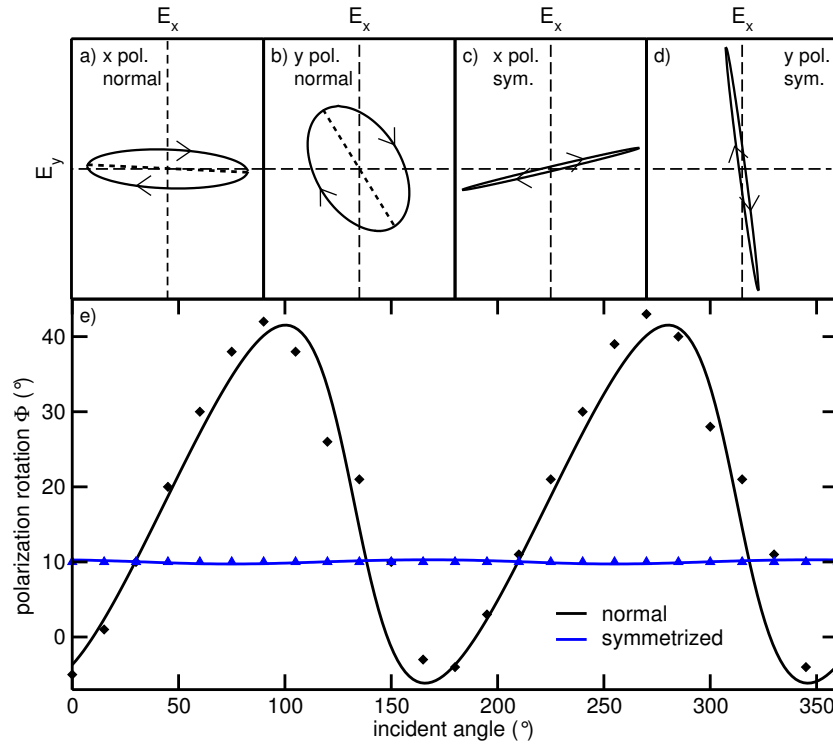


Figure 5.10: Polarization state after transmission through (a,b) the normal sample, and (c,d) the symmetrized sample at 3.3 cm^{-1} for incident x and y polarizations, respectively. (e) Angle of the polarization rotation of two samples shown investigated. Symbols denote the directly measured data, the solid lines the data calculated using the transmission and rotation matrices, Eq. 5.3.

Since the signal is near zero the measurement system loses its stability and therefore no meaningful measurements are possible here.

All measured data were combined to determine the transmission matrix according to Eq. 5.1 and to get the angle dependent optical activity following Eq. 5.5 for all samples investigated. These results are summarized in Fig. 5.10, where Figs. 5.10 (a)-5.10(d) show the calculated polarization state after transmission through the different samples at 3.3 cm^{-1} . As can be seen not only the angle of polarization has been rotated after transmission but also the polarization state has been changed from linear to elliptical. Figure 5.10 (e) shows the polarization rotation, where the solid lines represent the data calculated from the transmission matrix method and directly measured data are shown as symbols. The polarization rotation obtained by the two

described methods closely coincides thus giving another proof of the correctness of the measuring method and of the data processing. As expected, the sample shown in Figs. 5.9 (a,b) reveals a large dependence on the incident polarization angle and in the symmetrized array this dependence is removed within the experimental accuracy. From this data the rotary power Θ can be obtained, for which $\Theta = \Phi\lambda/d$ holds, where $d = 90 \mu\text{m}$ is the thickness of the sample and λ the wavelength. A rotary power of $\Theta \simeq 600 \text{ deg}/\lambda$ for the simple sample and $\Theta \simeq 330 \text{ deg}/\lambda$ for the symmetrized one at a radiation wavelength $\lambda = 3 \text{ mm}$ is obtained. The rotary power of the symmetrized sample is about 60% of that of the simple sample and is independent of the polarization angle within the experimental resolution. The decrease of the rotary power is due to a dephasing influence of the neighbour rings. This effect is absent in the simple sample because all resonators have the same orientation. The rotary power of typical natural occurring materials like quartz ($\Theta = 0.01 \text{ deg}/\lambda$) or sugar ($\Theta = 4 \cdot 10^{-4} \text{ deg}/\lambda$) are four to six orders of magnitudes smaller, than the obtained values for the metastructure [112]. Similar structures have been investigated in the literature at terahertz frequencies and in the infrared spectral range. Here, values of $1530 \text{ deg}/\lambda$ at $17 \mu\text{m}$ (Ref. [108]) and $420 \text{ deg}/\lambda$ at $\approx 3 \mu\text{m}$ (Ref. [109]) are reported, which are quite comparable to those obtained in this work and show the advantage of the metastructures compared to natural materials.

As could be seen in Fig. 5.10 (a-d) the polarization state of the light changes upon transmission from linear to elliptical, which is an undesired property for a polarization rotator. A strict polarization rotation device would ideally just change the angle of polarization but not the polarization state. Therefore an ellipticity of zero would be the desired state. Now, is it possible to reach this goal with this structure? In order to investigate this question in more detail the transmission matrix formalism can be used again, which also allows the calculation of the ellipticity besides the polarization rotation angle using Eq. 5.5. The results of this calculations are shown in Fig. 5.11 (a,b) for the simple sample and (c,d) symmetrized one. Figure 5.11 (a,c) shows the angle of polarization rotation and (b,d) the ellipticity in dependence of the frequency. As can be seen in Fig. 5.11 (a,b) both the polarization rotation and the ellipticity strongly depend on the frequency of the exciting light as well as the

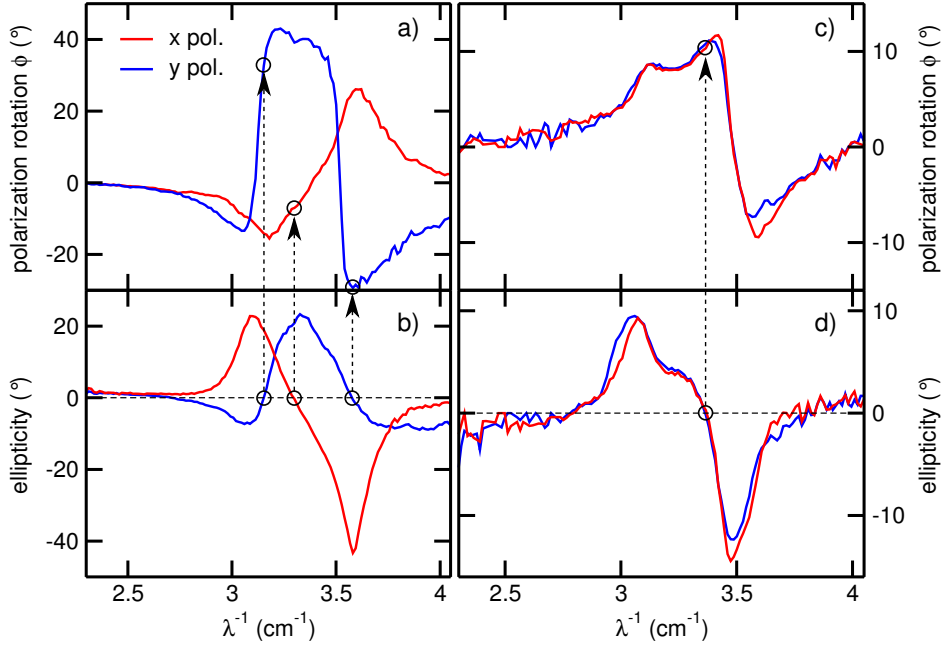


Figure 5.11: Frequency dependent polarization rotation (a,b) and ellipticity (c,d) calculated from the spectra (Fig. 5.9) using Eq. 5.1. Left panels: conventional sample, right panels: symmetrized sample.

orientation of the polarization vector. Outside of the resonance range both the ellipticity and the polarization rotation become zero as it is expected. Figure 5.11 (d) shows that in fact there exist frequencies (at 3.2 cm^{-1} and 3.6 cm^{-1}) at which the ellipticity becomes zero while the polarization rotation has still a large value (35° and -29°) at least for an incident polarization orientated along the y-direction. For the orthogonal polarization there is also a frequency with zero ellipticity (at 3.3 cm^{-1}), but in this case the polarization rotation is very small in comparison (-7°). The same procedure is repeated for the symmetrized sample in Fig. 5.10 (c,d). Here again it can be clearly seen that the anisotropy is lifted in the symmetrized sample. At 3.4 cm^{-1} there also exist a frequency at which the ellipticity becomes zero with a reasonably high value of the polarization rotation (11°). Therefore for both investigated sample geometries in fact a pure polarization rotator could be realized, which just rotates the polarization vector without changing the polarization state of the light.

5.6 Summary

In this chapter the coupling of twisted layers of split ring resonators was studied. It has been shown that the layers, with a twist angle of 90° , couple inductively which leads to the formation of chiral quasi-molecules and the splitting of the fundamental mode in two distinct modes. The splitting of the mode is strongly dependent on the coupling strength of the two layers and can be adjusted by changing the distance between them. The chirality of this structure leads to an optical activity which exceeds the one of natural materials by four to six orders of magnitudes. However, a pronounced asymmetry in the transmission properties of the coupled system, and therefore in the optical activity, is observed, which make an application difficult. In order to overcome this problem additional symmetry elements were introduced in the unit cell, which leads to an angle independent response of the structure. Rotary powers of $\Theta \simeq 600 \text{ deg}/\lambda$ for the simple sample and $\Theta \simeq 330 \text{ deg}/\lambda$ for the symmetrized one were obtained. However, it turned out, that not only the polarization direction got rotated but also the polarization state was changed upon transmission. By a careful choice of the excitation frequency, this problem can be overcome and a pure polarization rotator can be constructed using the layered metamaterial geometry.

Chapter 6

Electric excitation of the paramagnetic resonance in GGG

Split ring resonators are bianisotropic, which means there exists a cross-coupling between electric and magnetic fields in these materials. This fact has been extensively discussed in the previous chapters and also applied to couple two adjacent layers of SRRs in Ch. 5. In this chapter the bianisotropy of the SRRs is used to couple the rings to the electron-spin resonance (ESR) of a magnetic material. It will be shown that this coupling enables the excitation of the paramagnetic resonance using the electric field component of the incident radiation. A classical model of two coupled oscillator is presented to explain the observed effects. In addition, the coupling leads to an anticrossing of the coupled split-ring-electron-spin resonances which is similar to classical anticrossing effects in condensed matter physics. The observed anticrossing leads to an inversion of the ESR-signal.

Copper split rings were used in the present experiments and were prepared as already discussed above (see Ch. 3.1 for details). The rings are $0.35 \text{ mm} \times 0.35 \text{ mm}$ in size with a gap width $g = 0.17 \text{ mm}$. The metal thickness is $20 \mu\text{m}$ with an arm width $w = 50 \mu\text{m}$. The overall unit cell size is $s = 0.7 \text{ mm}$. Thus the studied rings are very similar to the ones investigated in Ch. 5, except of a slightly larger gap size. The samples were produced on a woven glass substrate with a thickness of 0.56 mm . As a paramagnetic material for the

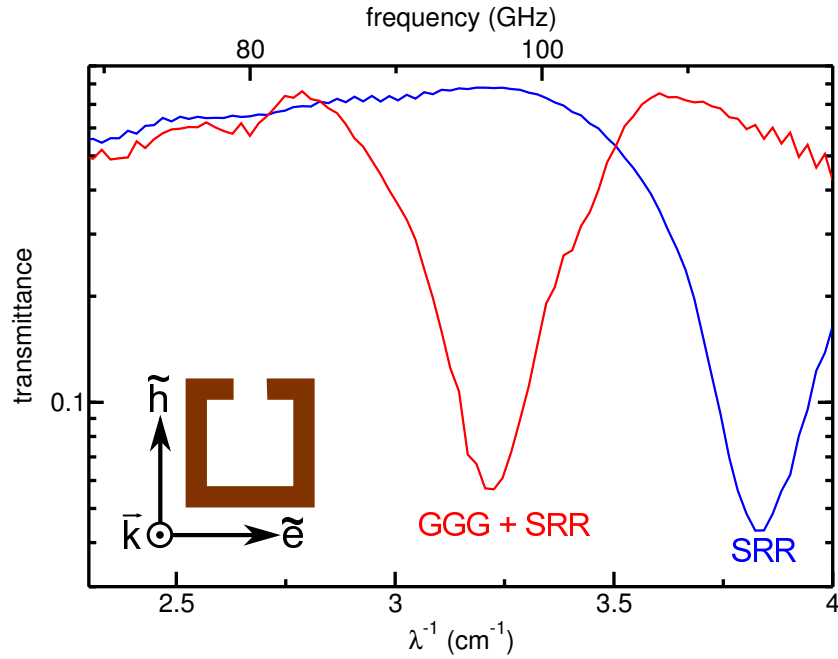


Figure 6.1: Transmittance spectra of the split ring + substrate system (blue) and the GGG + split ring + substrate system (red).

ESR experiments gadolinium gallium garnet ($\text{Gd}_3\text{Ga}_5\text{O}_{12}$, GGG) was used. Samples of GGG are commercially available substrates with a characteristic size of $10 \times 10 \times 0.48 \text{ mm}^3$. The refractive indices of the woven glass and the GGG has been determined in separate transmittance experiments as $n_s = 2.07 + 0.04i$ and $n_{GGG} = 3.4 + 0.008i$, respectively.

Typical transmittance spectra of the SRR used in this chapter are presented in Fig. 6.1. The blue line shows the transmittance of the rings on the substrate when excited with the electrical field of the electromagnetic radiation. The resonance frequency lies at 3.82 cm^{-1} (114 GHz) and therefore slightly higher than of the rings used in Ch. 5. This is well expected after Ch. 3.4 due to the increased gap size. The situation changes now if the GGG is brought in contact with the SRRs. The red line in Fig. 6.1 shows the transmission spectrum of the GGG-rings-substrate system without an external magnetic field. As can be clearly seen, the resonance frequency is at 3.26 cm^{-1} (98 GHz) and thus shifted significantly compared to the conventional sample. The reason for this change is the change in the dielectric environment of the rings. As has been discussed in Ch. 3.4 the presence of a substrate significantly alters

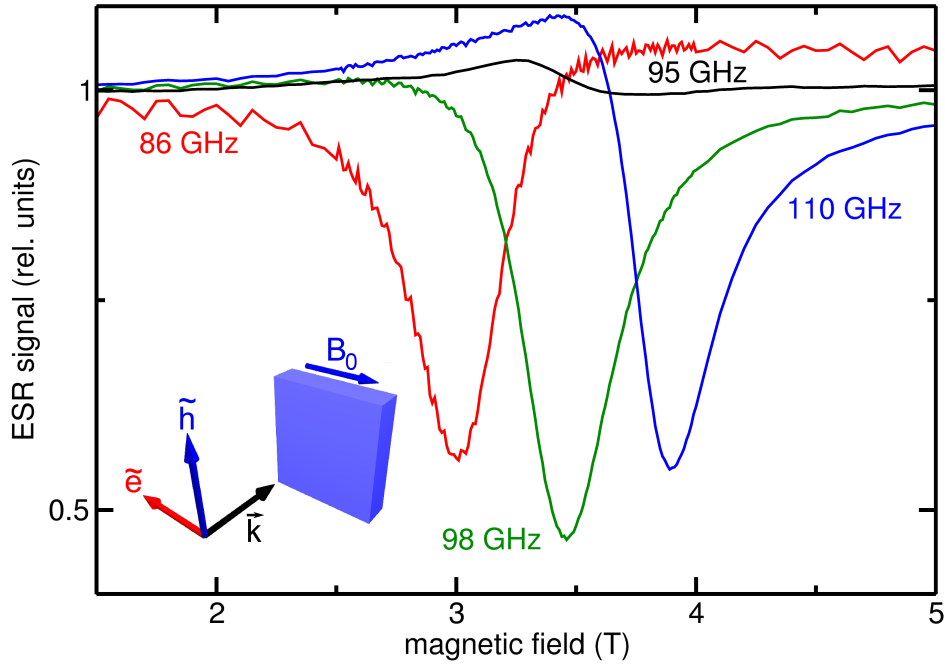


Figure 6.2: ESR signal of pure GGG at different frequencies at $T = 175$ K. Inset shows the excitation geometry. Black line shows excitation with $\tilde{h} \parallel B_0$ at 95 GHz.

the resonance frequency of the SRR. With the GGG attached to the rings a dielectric medium is present on both sides of the rings, which leads to the observed shift in the resonance frequency.

Now, before the coupled system of GGG and SRRs is investigated, the electron-spin resonance experiments on pure GGG should be discussed. In these experiments the transmitted signal at a fixed frequency is measured as a function of an applied static magnetic field. In GGG both Ga^{3+} and O^{2-} have filled electronic shells and hence are magnetically neutral. Gd^{3+} has the electronic configuration $[\text{Xe}]4f^7$ and is a spin-only ion with $S = 7/2$. Without an external magnetic field the spin-states are degenerate. When brought into a magnetic field the degeneracy of the spin-states will be lifted and the energy levels are split (Zeeman effect). The energetic splitting between the split levels equals to $\Delta E = g\mu_B B_0$. Here $g \approx 2$ is the g-factor of the electron, μ_B the Bohr magneton and B_0 the external magnetic field. Photons with an energy equal to the Zeeman splitting can now be absorbed, leading to sharp

electron spin resonances. Thus the resonance condition is

$$h\nu = g\mu_B B_0, \quad (6.1)$$

where h is the Planck's constant. But beside this energetic condition also a second condition is important for the excitation of the ESR. Due to the selection rules, transitions are only allowed when the oscillating magnetic field (\tilde{h}) of the electromagnetic radiation is oriented perpendicular to the static magnetic field. The inset of Fig. 6.2 shows a sketch of the active geometry. Therefore, these experiments are highly sensitive to the excitation geometry. This provides the experimental selectivity of the polarization of the electromagnetic wave to the ESR signal.

Figure 6.2 shows typical ESR signals of GGG for different frequencies. As can be clearly seen, a strong absorption of the electromagnetic radiation occurs if both, the excitation geometry ($\tilde{h} \perp B_0$) and the resonance condition (Eq. 6.1) are fulfilled. The resonance magnetic field is directly proportional to the exciting frequency. If the incident polarization is rotated by 90° , the condition for the excitation geometry is broken and therefore no ESR signal could be observed (black line in Fig. 6.2). However, in Fig. 6.2 nevertheless a small excitation can be observed, showing an slightly enhanced transmission at the resonance field. This points towards an unknown magnetoelectric effect in GGG which has to be studied in more detail.

If the split rings are now combined with the GGG, most interesting effects occur. Figure 6.3 shows the result of these experiments. The incident polarization in this case does not fulfil the excitation condition (*i.e.* $\tilde{h} \parallel B_0$) and thus almost no effect can be observed above or below the resonance of the split rings (see curves for 86 GHz or 110 GHz, respectively). This situation changes drastically if the excitation frequency equals the resonance frequency of the rings. The green curve shows the ESR signal at 98 GHz for which the resonance frequency of the rings coincides with the electron-spin resonance in GGG. Indeed a very strong signal can be observed which is the result of the coupling between the two systems. This behaviour can be explained by the bianisotropy of the split rings. In resonance the electric component of the

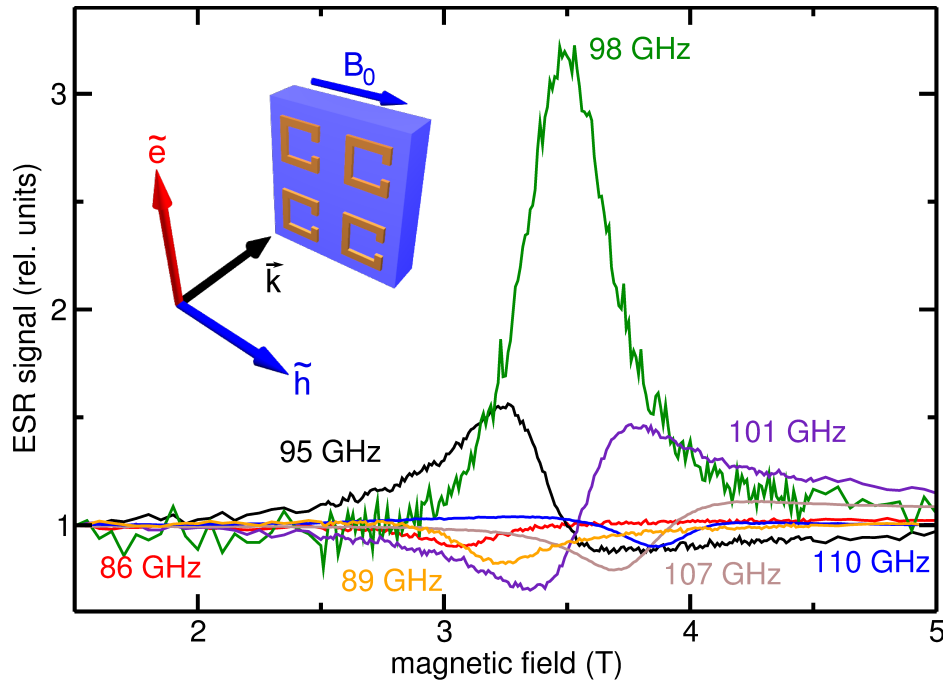


Figure 6.3: ESR signal of coupled SRR and GGG at various frequencies at $T = 175$ K. When the resonance frequencies of the rings and the GGG coincide a strong enhancement in the signal can be observed. Inset shows the excitation geometry.

radiation excites a circular current in the rings. This oscillating current leads to a magnetic ac field oriented perpendicular to the plane of the rings. This ac magnetic field is obviously also perpendicular to the static magnetic field B_0 and, therefore, the excitation condition of the ESR in GGG is fulfilled. Hence, the ESR could be excited by the electric component of the radiation. Due to the broad resonance of the split rings an effect can be observed also at frequencies near the resonance.

As a first guess one would naively expect an additional absorption within the resonance condition. Surprisingly, the ESR signal shows a maximum as a function of the magnetic field when the resonance condition is met. This inversion of the ESR signal arises due to the coupling between the GGG and the SRR and the subsequent modifications of the effective material parameters. The basic physics of this effects can be explained using a simple model

of two coupled oscillators [113]:

$$\begin{aligned} m_1 \ddot{x}_1 + g_1 \dot{x}_1 + k_1 x_1 - k_{12} x_2 &= e_1 E_0 e^{-i\omega t} \\ m_2 \ddot{x}_2 + g_2 \dot{x}_2 + k_2 x_2 - k_{12} x_1 &= e_2 E_0 e^{-i\omega t}, \end{aligned} \quad (6.2)$$

here $x_{1,2}$, $m_{1,2}$, $g_{1,2}$, $k_{1,2}$ and $e_{1,2}$ are the displacements, masses, damping constants, restoring forces constants, and effective charges of both oscillators, respectively. The coupling between the two oscillators is given by k_{12} . The excitation is given by a time harmonic electric field in the form $E = E_0 e^{-i\omega t}$, with $\omega = 2\pi\nu$ being the angular frequency of the excitation. Using the Ansatz $x_{1,2}(t) = x_{1,2}^0 e^{-i\omega t}$, the substitutions

$$\begin{aligned} \omega_{1,2}^2 &= \frac{k_{1,2}}{m_{1,2}}, k = \frac{k_{12}}{\sqrt{m_1 m_2}}, f_{1,2} = \frac{n e_{1,2}^2}{\epsilon_0 m_{1,2}}, \gamma_{1,2} = \frac{g_{1,2}}{m_{1,2}}, \\ \Omega_{1,2} &= \omega_{1,2}^2 - \omega^2 - i\omega\gamma_{1,2} \end{aligned} \quad (6.3)$$

and some simple mathematics, one could obtain an expression for the effective susceptibility $\chi_e = P/\epsilon_0 E_0 = n(e_1 x_1 + e_2 x_2)/\epsilon_0 E_0$ of the coupled system. Here n is the charge density and ϵ_0 the permittivity of the free space. Therefore the effective dielectric permittivity of the system is

$$\epsilon(\omega) - 1 = \frac{f_1 \Omega_2 + f_2 \Omega_1 + 2k\sqrt{f_1 f_2}}{\Omega_1 \Omega_2 - k^2}. \quad (6.4)$$

In addition the eigenfrequencies of the system become renormalized due to the coupling. They are given by the poles of Eq. 6.4:

$$\omega_{\pm}^2 = \frac{1}{2} \left[\omega_1^2 + \omega_2^2 \pm \sqrt{(\omega_1^2 - \omega_2^2)^2 + 4k^2} \right]. \quad (6.5)$$

Although based on a very simple model, Eq. 6.4 already catches the basic physics of the problem. In order to explain the experiments in Fig. 6.3 one sets the strength of the second oscillator to zero ($f_2 = 0$). This corresponds to the situation in the present experiments since the spins of the GGG are inactive because of the geometry of the experiment ($\tilde{h} \parallel B_0$). If the resonance frequencies of both oscillators coincide ($\omega_1 = \omega_2 = \omega_0$), the response of the coupled system splits into two resonances at $\omega_{\pm}^2 = \omega_0^2 \pm k$. The absorption in

resonance ($\omega = \omega_0$) of the coupled system can then be obtained by Eq. 6.4, leading to

$$\text{Im}[\epsilon(\omega_0)] = \frac{\gamma_2 \omega_0 f_1}{\omega_0^2 \gamma_1 \gamma_2 + k^2}. \quad (6.6)$$

As can be seen in Eq. 6.6 the coupling term is present in the denominator only. Therefore, an increased coupling will lead to an overall decreased absorption in the system, which is exactly what could be observed in the experiment [Fig. 6.3]. This behaviour is very similar to the electromagnetically induced transparency [114] which also could be observed in metamaterials [115].

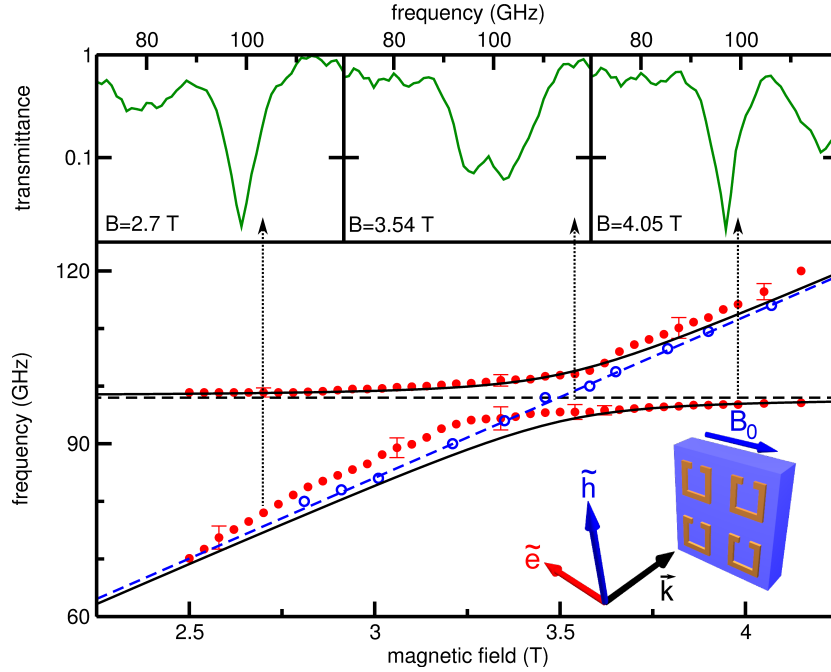


Figure 6.4: Anticrossing of electron-spin and split-ring resonances. Upper panels: Typical transmittance spectra at different fields at $T = 175$ K. Lower panel: Solid red circles - positions of the resonances in the anticrossing regime. Open blue circles: resonance frequencies of pure GGG. Straight dashed lines represent the behaviour of the resonances without coupling. Solid lines are drawn according to Eq. 6.5.

A second experiment is shown in Fig. 6.4. Here the incident polarization is chosen in a way that both the split rings ($\tilde{e} \parallel \text{gap}$) as well as the paramagnetic resonance ($\tilde{h} \perp B_0$) are excited by the incident radiation. A sketch of this geometry can be found in the inset of Fig. 6.4. The upper panel of Fig. 6.4 shows typical transmittance spectra when both resonances are active at dif-

ferent magnetic fields. At fields well outside the coupling region ($B_0 = 2.7$ T and 4.05 T, respectively) two distinct resonances could be observed, which can clearly be attributed to the split-rings or the GGG, respectively. But for magnetic fields around 3.5 T the resonances are strongly coupled and therefore an unambiguous assignment cannot be done and one should speak about coupled split-ring-electron-spin resonance. The lower panel of Fig. 6.4 shows the frequency of both resonances as a function of the magnetic field (red filled circles). A clear effect of anticrossing of both resonances can be clearly seen. This effect is similar to classical anticrossing effects in condensed matter physics like phonon + photon, where the interaction region is called a polariton. In addition, in Fig. 6.4 the behaviour of the pure ESR in GGG is shown (open blue circles). As can be expected from Eq. 6.1 a direct proportionality between the applied field and resonance frequency is observed (shown as dashed blue line). The black dashed line shows the resonance frequency of the SRR which is independent of the external field. Solid black lines are obtained using Eq. 6.5 with $\omega_1 = \text{const}$ and $\omega_2 = \frac{g\mu_B}{\hbar} B_0$. As can be clearly seen the simple model nicely depicts the experimental points.

In conclusion, in this chapter the coupling of split ring resonators to a paramagnetic material has been investigated. The bianisotropic properties of the SRR enables the excitation of the electron-spin resonance in GGG using the electric field component of the light. In opposite to the conventional ESR the coupling between the split-ring metamaterial and the GGG leads to a maximum in the transmittance. In addition, it has been shown, that in the geometry in which both the SRR and the GGG are excited an anticrossing of the modes can be observed. All experimental results can be explained using a classical model of two coupled oscillators.

Chapter 7

Conclusion

The field of metamaterials has attracted much research interest in the last few years, due to their unusual electrodynamic properties. Features like a negative permeability and a negative index of refraction, which are not obtainable in natural materials, can be realized using these materials. These effects open up the way to novel applications like cloaking devices or sub-diffractive imaging. An important realization of a metamaterial is given by the split-ring resonators. Although consisting of purely non-magnetic material, they show a very large magnetic response. Furthermore split-ring resonators are bianisotropic, *i.e.* they show a cross-coupling between the electric and the magnetic field. This enables another possible way of controlling the propagation of light. In addition, they are largely scalable over a broad frequency range and easy to produce. Therefore, they are a promising candidate for future application. However, in order to do this, their basic properties have to be fully understood. Thus, a main concern of this work is dedicated to the investigation of electrodynamic properties of split-ring metamaterials.

In this work split-ring resonators were studied using submillimeter wave spectroscopy which allows the measurement of the intensity and phase shift of the transmitted and reflected light within controlled polarization geometries. The investigations were concentrated on:

Magnetolectric properties

The split rings can be excited either by electric or by magnetic component of the electromagnetic radiation. When excited electrically several different modes can be seen in experiment. However, only the fundamental mode of the structure shows substantial magnetic/bianisotropic response and still remains within the effective parameter approximation. Therefore, this work focussed mainly on this fundamental mode. A simple (R)LC-circuit model was presented, which can be used to understand the response of the rings to a good approximation. This model suggest a Lorentzian shape for the resonances, which can be nicely seen in experiment. In addition, according to this model the condition $\chi_{em}\chi_{me} = \chi_e\chi_m$ is fulfilled for split-ring resonators, which is the thermodynamic maximum for magneto-electric media and greatly exceeds the value occurring in natural materials. This assumption could be confirmed using oblique incidence transmittance and reflectance experiments. SRRs are therefore building blocks for a perfect magneto-electric material.

Homogenization

The homogenization of metamaterials is yet a major topic in current research, although studied for over ten years. Especially for single layer samples, so called metafilms, the homogenization is not a simple task. In the present work it was shown, that a bulk approach description clearly fails for metafilms made of SRRs. To overcome this problem a simple two-layer model has been proposed, in which the metafilm is considered as an effective layer on top of a dielectric substrate. As it turned out, this model can reproduce the experimental spectra almost perfectly, as long as the thickness of the effective layer is also considered. Instead of the susceptibility χ_e alone, the product of $\chi_e \cdot d$ is the characterizing magnitude in this picture. This model is equivalent to the model of surface polarizabilities often proposed for the description of metafilms. However, experiments under oblique incidence have revealed, that the resulting parameters slightly depend on the angle of incidence. This points towards a spatial dispersion, not considered in this model yet. Therefore, the inclusion of the spatial dispersion in a rigorous physical model will be a very important future task for theoreticians working in the field of metamaterials.

Loss performance

The Q-factor of split-ring resonators is an important parameter for certain applications. Especially in sensor applications a very high Q-factor is necessary. The conventional samples studied in this work showed Q-values between 15 and 30. Three main parameters determine the Q-factor of the structure: the ohmic losses in the metal, the dielectric losses in the substrate and the radiation losses. For lossy substrate it was shown, that the dielectric losses exceed substantially the ohmic losses in the metal. However, for lossless substrates the ohmic losses becomes important. In order to further improve the performance of the structures, superconducting metals can be used. It was shown that in split-rings made from superconducting Nb the Q-factor indeed can be greatly improved below the superconducting transition. Values up to $Q \sim 100$ can be easily reached using superconductors. In addition, the usage of superconductors as metal opens up another possibility of tuneability. In course of this work it turned out, that the resonance frequency in this materials can be tuned by external parameters, like temperature and/or external static magnetic field. The third loss mechanism, namely the radiation losses, is not easily manipulated. The radiation losses are inherent to a given structure and therefore an adaption of the basic constituents of the structure is necessary. A possible approach, presented in this work, is to use slightly asymmetric split-rings. Due to the asymmetry the coupling of the electromagnetic field to the structure, and therefore the radiation losses, can be reduced. It turned out, that using this modified unit cell as well as superconducting Nb leads to a further improvement of the metamaterials performance. In this structure overall Q-factors of up to 150 can be reached. A careful design of the metamaterials unit cell, as well as the usage of low loss materials, can be used to greatly improve the performance of the metamaterial.

Novel applications

The bianisotropy of the SRRs opens up new possibilities of controlling the propagation of light. It was shown that the bianisotropy can be used to build chiral quasi-molecules from two layers of mutually twisted split-rings. It turned out, that this coupled structure shows a large optical activity far exceeding the ones obtainable in natural materials. The pronounced anisotropy

in this structure could be removed by introducing a C_4 symmetry in the unit cell. Rotary powers of up to $600 \text{ deg}/\lambda$ and $330 \text{ deg}/\lambda$ can be reached for the anisotropic and symmetrized samples, respectively. Therefore, ultra-thin polarization rotators can be realized using metamaterials. Furthermore the bianisotropy can also be used to excite the paramagnetic resonance in a magnetic material using the electric field of the light. In opposite to the conventional ESR the coupling between the split-rings and the magnetic system lead to an inversion of the ESR signal, *i.e.* a maximum in the transmittance can be observed.

To summarize, although the basic physics of split-ring metamaterials are simple to understand, their intrinsic properties nevertheless can lead to unusual and unexpected effects opening up the road for novel applications in the future.

Appendix A

Retrieval of boundary matrix

First consider a situation as shown in Fig. A.1 (a). An electromagnetic wave is incident from the left side on a boundary between two different isotropic, linear media, whose optical properties can be described by the dielectric permittivity ε and the magnetic permeability μ . Furthermore it is assumed, that in these media no free currents or charges are present, so just dielectric media are considered. Therefore the constituent relations for this media are given by

$$\vec{D} = \varepsilon_0 \varepsilon \vec{E}, \quad (\text{A.1})$$

$$\vec{B} = \mu_0 \mu \vec{H}. \quad (\text{A.2})$$

Here \vec{D} , \vec{B} give the electric and magnetic flux densities, \vec{E} , \vec{H} the electric and magnetic fields and ε_0 , μ_0 the permittivity and permeability of the vacuum, respectively. Using the superposition principle the electric/magnetic field in each medium can be divided in a part which goes from left to right (indicated by the superscript +) and from right to left (indicated by -). Throughout this work a $e^{-i\omega t}$ time dependence is assumed, where $\omega = 2\pi\nu$ is the angular frequency of the wave. Therefore the electric field in medium i is given by

$$\vec{E}_i = \left(\vec{E}_i^+ e^{i\vec{k}_i \vec{x}} + \vec{E}_i^- e^{-i\vec{k}_i \vec{x}} \right) e^{-i\omega t}. \quad (\text{A.3})$$

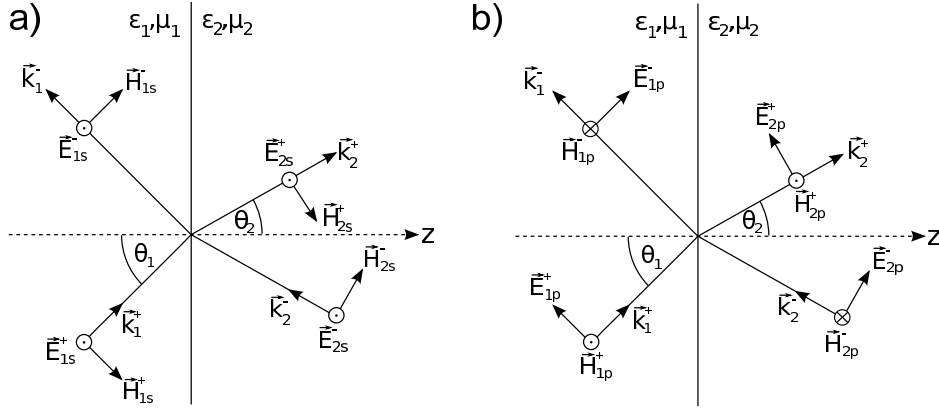


Figure A.1: Geometry for the calculation of the boundary matrix for a) *s*-wave and b) *p*-wave.

A similar equation also holds for the magnetic field. At a boundary between two media the electromagnetic field obeys certain boundary conditions [116]. On the one hand the tangential component of the electric field, and in case of vanishing currents in the media also the magnetic field, have to be continuous:

$$\vec{n} \times (\vec{E}_1 - \vec{E}_2) = \vec{E}_1^t - \vec{E}_2^t = 0, \quad (\text{A.4})$$

$$\vec{n} \times (\vec{H}_1 - \vec{H}_2) = \vec{H}_1^t - \vec{H}_2^t = 0, \quad (\text{A.5})$$

where \vec{n} is the normal vector of the boundary. Furthermore the normal components of the magnetic induction, and in a media without any free charges also the electric displacement, have to be continuous:

$$\vec{n} \circ (\vec{B}_1 - \vec{B}_2) = \vec{B}_1^n - \vec{B}_2^n = 0, \quad (\text{A.6})$$

$$\vec{n} \circ (\vec{D}_1 - \vec{D}_2) = \vec{D}_1^n - \vec{D}_2^n = 0. \quad (\text{A.7})$$

From the boundary conditions, Eqs. A.4-A.7, it follows, that for the further considerations the polarization of the incident light is of major importance. First consider a wave linearly polarized with the electric field along the *y*-direction, as shown in Fig. A.1 (a). Such a wave is called *s*- or TE-wave. The boundary condition for the magnetic field can be expressed in terms of the

electric field using one of the Maxwell equations. The magnetic field then is:

$$\vec{H} = -\frac{i}{\omega\mu_0\mu}\vec{\nabla}\times\vec{E}. \quad (\text{A.8})$$

From the tangential boundary conditions (Eqs. A.4,A.5) and using the substitution of Eq. A.8, it follows:

$$E_{1s}^+ + E_{1s}^- = E_{2s}^+ + E_{2s}^- \quad (\text{A.9})$$

$$\sqrt{\frac{\varepsilon_1}{\mu_1}}(E_{1s}^+ - E_{1s}^-)\cos\theta_1 = \sqrt{\frac{\varepsilon_2}{\mu_2}}(E_{2s}^+ - E_{2s}^-)\cos\theta_2, \quad (\text{A.10})$$

where θ_i gives the angle of the wavevector \vec{k}_i to the surface normal and the subscript s denotes the s -component of the electric field. θ_2 is determined by Snell's law, $\sin\theta_2 = \frac{n_1}{n_2}\sin\theta_1$, with n_i being the respective index of refraction. Equations A.9 and A.10 can be represented in matrix form:

$$\begin{pmatrix} 1 & 1 \\ \sqrt{\frac{\varepsilon_1}{\mu_1}}\cos\theta_1 & -\sqrt{\frac{\varepsilon_1}{\mu_1}}\cos\theta_1 \end{pmatrix} \begin{pmatrix} E_{1s}^+ \\ E_{1s}^- \end{pmatrix} = \begin{pmatrix} 1 & 1 \\ \sqrt{\frac{\varepsilon_2}{\mu_2}}\cos\theta_2 & -\sqrt{\frac{\varepsilon_2}{\mu_2}}\cos\theta_2 \end{pmatrix} \begin{pmatrix} E_{2s}^+ \\ E_{2s}^- \end{pmatrix}, \quad (\text{A.11})$$

or

$$\begin{pmatrix} E_{2s}^+ \\ E_{2s}^- \end{pmatrix} = \frac{1}{2} \begin{pmatrix} 1 + \alpha & 1 - \alpha \\ 1 - \alpha & 1 + \alpha \end{pmatrix} \begin{pmatrix} E_{1s}^+ \\ E_{1s}^- \end{pmatrix} = \hat{D}_{21}^s \begin{pmatrix} E_{1s}^+ \\ E_{1s}^- \end{pmatrix}, \quad (\text{A.12})$$

with $\alpha = \sqrt{\frac{\varepsilon_1\mu_2}{\varepsilon_2\mu_1}}\frac{\cos\theta_1}{\cos\theta_2}$. \hat{D}_{21}^s therefore interconnects the electric fields at the right and left side of the boundary. For an incident wave with the electric field in the plane of incidence, as shown in Fig. A.1(b), a so called p - or TM-wave, similar considerations can be made which leads to an expression:

$$\begin{pmatrix} E_{2p}^+ \\ E_{2p}^- \end{pmatrix} = \frac{1}{2} \begin{pmatrix} \frac{\cos\theta_1}{\cos\theta_2} + \sqrt{\frac{\varepsilon_1\mu_2}{\varepsilon_2\mu_1}} & \frac{\cos\theta_1}{\cos\theta_2} - \sqrt{\frac{\varepsilon_1\mu_2}{\varepsilon_2\mu_1}} \\ \frac{\cos\theta_1}{\cos\theta_2} - \sqrt{\frac{\varepsilon_1\mu_2}{\varepsilon_2\mu_1}} & \frac{\cos\theta_1}{\cos\theta_2} + \sqrt{\frac{\varepsilon_1\mu_2}{\varepsilon_2\mu_1}} \end{pmatrix} \begin{pmatrix} E_{1p}^+ \\ E_{1p}^- \end{pmatrix} = \hat{D}_{21}^p \begin{pmatrix} E_{1p}^+ \\ E_{1p}^- \end{pmatrix}. \quad (\text{A.13})$$

For normal incidence ($\theta_1 = \theta_2 = 0$) the distinction between s - and p -wave becomes unnecessary since $\hat{D}_{21}^s = \hat{D}_{21}^p = \hat{D}_{21}$.

Appendix B

4×4 formalism

The starting point for the calculations are the Maxwell equations which may be written in matrix form:

$$\begin{pmatrix} 0 & 0 & 0 & 0 & -\frac{\partial}{\partial z} & \frac{\partial}{\partial y} \\ 0 & 0 & 0 & \frac{\partial}{\partial z} & 0 & -\frac{\partial}{\partial x} \\ 0 & 0 & 0 & -\frac{\partial}{\partial y} & \frac{\partial}{\partial x} & 0 \\ 0 & \frac{\partial}{\partial z} & -\frac{\partial}{\partial y} & 0 & 0 & 0 \\ -\frac{\partial}{\partial z} & 0 & \frac{\partial}{\partial x} & 0 & 0 & 0 \\ \frac{\partial}{\partial y} & -\frac{\partial}{\partial x} & 0 & 0 & 0 & 0 \end{pmatrix} \begin{pmatrix} E_x \\ E_y \\ E_z \\ H_x \\ H_y \\ H_z \end{pmatrix} = \frac{\partial}{\partial t} \begin{pmatrix} D_x \\ D_y \\ D_z \\ B_x \\ B_y \\ B_z \end{pmatrix}. \quad (\text{B.1})$$

Using Eq. 2.13, the harmonic time dependence $e^{-i\omega t}$ and the assumption, that there is no spatial dependence of the material parameters in the x - and y -direction, *i.e.* k_x and k_y are constant, gives:

$$\begin{pmatrix} 0 & 0 & 0 & 0 & -\frac{\partial}{\partial z} & ik_y \\ 0 & 0 & 0 & \frac{\partial}{\partial z} & 0 & -ik_x \\ 0 & 0 & 0 & -ik_y & ik_x & 0 \\ 0 & \frac{\partial}{\partial z} & -ik_y & 0 & 0 & 0 \\ -\frac{\partial}{\partial z} & 0 & ik_x & 0 & 0 & 0 \\ ik_y & -ik_x & 0 & 0 & 0 & 0 \end{pmatrix} \begin{pmatrix} E_x \\ E_y \\ E_z \\ H_x \\ H_y \\ H_z \end{pmatrix} = -i\omega \hat{M} \begin{pmatrix} E_x \\ E_y \\ E_z \\ H_x \\ H_y \\ H_z \end{pmatrix}. \quad (\text{B.2})$$

The third and sixth rows are two algebraic equations which can be used to eliminate two of the variables and express them by the other four. Solving this for $E_z = \Gamma_3$ and $H_z = \Gamma_6$ leads to:

$$\begin{aligned}\Gamma_3 &= a_{31}\Gamma_1 + a_{32}\Gamma_2 + a_{34}\Gamma_4 + a_{35}\Gamma_5 \\ \Gamma_6 &= a_{61}\Gamma_1 + a_{62}\Gamma_2 + a_{64}\Gamma_4 + a_{65}\Gamma_5\end{aligned}\tag{B.3}$$

with

$$\begin{aligned}a_{31} &= [M_{36}(M_{61} + \frac{k_y}{\omega}) - M_{31}M_{66}]/d, \\ a_{32} &= [M_{36}(M_{62} - \frac{k_x}{\omega}) - M_{32}M_{66}]/d, \\ a_{34} &= [M_{36}M_{64} - M_{66}(M_{34} - \frac{k_y}{\omega})]/d, \\ a_{35} &= [M_{36}M_{65} - M_{66}(M_{35} - \frac{k_x}{\omega})]/d, \\ a_{61} &= [M_{63}M_{31} - M_{33}(M_{61} + \frac{k_y}{\omega})]/d, \\ a_{62} &= [M_{63}M_{32} - M_{33}(M_{62} - \frac{k_x}{\omega})]/d, \\ a_{64} &= [M_{63}(M_{34} - \frac{k_y}{\omega}) - M_{64}M_{33}]/d, \\ a_{65} &= [M_{63}(M_{35} - \frac{k_x}{\omega}) - M_{65}M_{33}]/d, \\ d &= M_{66}M_{33} - M_{63}M_{36}.\end{aligned}\tag{B.4}$$

Equations B.3 can now be substituted in Eq. B.2 leading to a 4×4 representation of the Maxwell equations in the form

$$\frac{\partial}{\partial z}\vec{\psi} = i\omega\hat{S}\vec{\psi}\tag{B.5}$$

with $\vec{\psi} = (E_x, E_y, H_x, H_y)^T$ being the reduced vector of field amplitudes. The components of \hat{S} are given by:

$$\begin{aligned}
S_{11} &= M_{51} + (M_{53} + \frac{k_x}{\omega})a_{31} + M_{56}a_{61}, \\
S_{12} &= M_{52} + (M_{53} + \frac{k_x}{\omega})a_{32} + M_{56}a_{62}, \\
S_{13} &= M_{54} + (M_{53} + \frac{k_x}{\omega})a_{34} + M_{56}a_{64}, \\
S_{14} &= M_{55} + (M_{53} + \frac{k_x}{\omega})a_{35} + M_{56}a_{65}, \\
S_{21} &= -M_{41} - (M_{43} - \frac{k_y}{\omega})a_{31} - M_{46}a_{61}, \\
S_{22} &= -M_{42} - (M_{43} - \frac{k_y}{\omega})a_{32} - M_{46}a_{62}, \\
S_{23} &= -M_{44} - (M_{43} - \frac{k_y}{\omega})a_{34} - M_{46}a_{64}, \\
S_{24} &= -M_{45} - (M_{43} - \frac{k_y}{\omega})a_{35} - M_{46}a_{65}, \\
S_{31} &= -M_{21} - M_{23}a_{31} - (M_{26} - \frac{k_x}{\omega})a_{61}, \\
S_{32} &= -M_{22} - M_{23}a_{32} - (M_{26} - \frac{k_x}{\omega})a_{62}, \\
S_{33} &= -M_{24} - M_{23}a_{34} - (M_{26} - \frac{k_x}{\omega})a_{64}, \\
S_{34} &= -M_{25} - M_{23}a_{35} - (M_{26} - \frac{k_x}{\omega})a_{65}, \\
S_{41} &= M_{11} + M_{13}a_{31} + (M_{16} + \frac{k_y}{\omega})a_{61}, \\
S_{42} &= M_{12} + M_{13}a_{32} + (M_{16} + \frac{k_y}{\omega})a_{62}, \\
S_{43} &= M_{14} + M_{13}a_{34} + (M_{16} + \frac{k_y}{\omega})a_{64}, \\
S_{44} &= M_{15} + M_{13}a_{35} + (M_{16} + \frac{k_y}{\omega})a_{65}.
\end{aligned} \tag{B.6}$$

Following the procedure described in Section 2.2.2, one is able to calculate the propagation matrix \hat{P} . In order to calculate the transmission and reflection coefficients it is convenient to change the basis from ψ to ψ' , whereas the components of ψ' consist of the waves propagating in positive/negative direction with two orthogonal polarizations. It is easy to show that the columns

of the basis transformation matrix \hat{V} consists of the four eigenvectors of the vacuum. Therefore \hat{V} is given by:

$$\hat{V} = \begin{pmatrix} \frac{k_z}{\sqrt{1-k_y^2}} & \frac{k_z}{\sqrt{1-k_y^2}} & 0 & 0 \\ 0 & 0 & \frac{k_z}{\sqrt{1-k_x^2}} & \frac{k_z}{\sqrt{1-k_x^2}} \\ -\frac{k_x k_y}{\sqrt{1-k_y^2}} & \frac{k_x k_y}{\sqrt{1-k_y^2}} & -\sqrt{1-k_x^2} & \sqrt{1-k_x^2} \\ \sqrt{1-k_x^2} & -\sqrt{1-k_x^2} & \frac{k_x k_y}{\sqrt{1-k_x^2}} & -\frac{k_x k_y}{\sqrt{1-k_x^2}} \end{pmatrix} \quad (\text{B.7})$$

Here the eigenvectors of the vacuum have been normalized to the absolute value of the wavevector, *i.e.* $k_x^2 + k_y^2 + k_z^2 = 1$. The propagation matrix \hat{P} in the new basis is now

$$\hat{P}' = \hat{V}^{-1} \hat{P} \hat{V}. \quad (\text{B.8})$$

Therefore the transmission and reflectance coefficients can be calculated by Eq. 2.21. The resulting coefficients are then explicitly given by (with $E_x^i = E_y^i = 1$):

$$\begin{aligned} d &= \hat{P}'_{22} \hat{P}'_{44} - \hat{P}'_{24} \hat{P}'_{42}, \\ r_{xx} &= (\hat{P}'_{24} \hat{P}'_{41} - \hat{P}'_{21} \hat{P}'_{44})/d, \\ r_{xy} &= -(\hat{P}'_{23} \hat{P}'_{44} - \hat{P}'_{24} \hat{P}'_{43})/d, \\ r_{yx} &= (\hat{P}'_{21} \hat{P}'_{42} - \hat{P}'_{22} \hat{P}'_{41})/d, \\ r_{yy} &= -(\hat{P}'_{22} \hat{P}'_{43} - \hat{P}'_{23} \hat{P}'_{42})/d, \\ t_{xx} &= \hat{P}'_{11} + \hat{P}'_{12} r_{xx} + \hat{P}'_{14} r_{yx}, \\ t_{xy} &= \hat{P}'_{13} + \hat{P}'_{12} r_{xy} + \hat{P}'_{14} r_{yy}, \\ t_{yx} &= \hat{P}'_{31} + \hat{P}'_{32} r_{xx} + \hat{P}'_{34} r_{yx}, \\ t_{yy} &= \hat{P}'_{33} + \hat{P}'_{32} r_{xy} + \hat{P}'_{34} r_{yy}. \end{aligned} \quad (\text{B.9})$$

Bibliography

- [1] V. G. Veselago. *The electrodynamics of substances with simultaneously negative values of ϵ and μ* . Sov. Phys. Usp. **10**, 4, p. 509 (1968), URL <http://stacks.iop.org/0038-5670/10/i=4/a=R04?key=crossref.49e6b8a483029417bb518fd3889a3ed3>
- [2] J. B. Pendry, A. J. Holden, D. J. Robbins, W. J. Stewart. *Magnetism from Conductors and Enhanced Nonlinear Phenomena*. IEEE Trans. Microwave Theory Tech. **47**, p. 2075 (1999), URL <http://ieeexplore.ieee.org/lpdocs/epic03/wrapper.htm?arnumber=798002>
- [3] J. B. Pendry, A. J. Holden, W. J. Stewart, I. Youngs. *Extremely Low Frequency Plasmons in Metallic Mesostructures*. Phys. Rev. Lett. **76**, 25, p. 4773 (1996), URL <http://link.aps.org/doi/10.1103/PhysRevLett.76.4773>
- [4] R. A. Shelby, D. R. Smith, S. Schultz. *Experimental Verification of a Negative Index of Refraction*. Science **292**, p. 77 (2001), URL <http://www.sciencemag.org/cgi/doi/10.1126/science.1058847>
- [5] J. B. Pendry. *A Chiral Route to Negative Refraction*. Science **306**, p. 1353 (2004), URL <http://www.sciencemag.org/cgi/doi/10.1126/science.1104467>
- [6] E. Cubukcu, K. Aydin, E. Ozbay, S. Foteinopoulou, C. M. Soukoulis. *Electromagnetic waves: Negative refraction by photonic crystals*. Nature **423**, p. 604 (2003), URL <http://www.nature.com/doifinder/10.1038/423604b>

- [7] A. Pimenov, A. Loidl, P. Przyslupski, B. Dabrowski. *Negative refraction in ferromagnet-superconductor superlattices*. Phys. Rev. Lett. **95**, p. 247009 (2005), URL <http://link.aps.org/doi/10.1103/PhysRevLett.95.247009>
- [8] S. Engelbrecht, A. M. Shuvaev, Y. Luo, V. Moshnyaga, A. Pimenov. *Negative refraction in natural ferromagnetic metals*. European Physics Letters **95**, p. 37005 (2011), URL <http://stacks.iop.org/0295-5075/95/i=3/a=37005?key=crossref.801efba2b4c1712ab53595d2749089e0>
- [9] U. Leonhardt. *Optical Conformal Mapping*. Science **312**, 5781, p. 1777 (2006), URL <http://www.sciencemag.org/cgi/doi/10.1126/science.1126493>
- [10] J. B. Pendry, D. Schurig, D. R. Smith. *Controlling Electromagnetic Fields*. Science **312**, p. 1780 (2006), URL <http://www.sciencemag.org/cgi/doi/10.1126/science.1125907>
- [11] J. B. Pendry. *Negative Refraction Makes a Perfect Lens*. Phys. Rev. Lett. **85**, 18, p. 3966 (2000), URL <http://link.aps.org/doi/10.1103/PhysRevLett.85.3966>
- [12] A. Grbic, G. V. Eleftheriades. *Overcoming the Diffraction Limit with a Planar Left-Handed Transmission-Line Lens*. Phys. Rev. Lett. **92**, p. 117403 (2004), URL <http://link.aps.org/doi/10.1103/PhysRevLett.92.117403>
- [13] D. Schurig, J. J. Mock, D. R. Smith. *Electric-field-coupled resonators for negative permittivity metamaterials*. Applied Physics Letters **88**, p. 041109 (2006), URL <http://link.aip.org/link/APPLAB/v88/i4/p041109/s1&Agg=doi>
- [14] A. Rogacheva, V. A. Fedotov, A. S. Schwanecke, N. I. Zheludev. *Giant Gyrotropy due to Electromagnetic-Field Coupling in a Bilayered Chiral Structure*. Phys. Rev. Lett. **97**, p. 177401 (2006), URL <http://link.aps.org/doi/10.1103/PhysRevLett.97.177401>

- [15] M. Kafesaki, I. Tsiapa, N. Katsarakis, T. Koschny, C. M. Soukoulis, E. N. Economou. *Left-handed metamaterials: The fishnet structure and its variations*. Physical Review B **75**, p. 235114 (2007), URL <http://link.aps.org/doi/10.1103/PhysRevB.75.235114>
- [16] G. V. Kozlov, A. A. Volkov. *Coherent Source Submillimeter Wave Spectroscopy*. In G. Grüner (Editor), *Millimeter and Submillimeter Wave Spectroscopy of Solids*, p. 51. Springer, Berlin (1998)
- [17] A. V. Pronin, Y. G. Goncharov, T. Fischer, J. Wosnitza. *Phase-sensitive terahertz spectroscopy with backward-wave oscillators in reflection mode*. REVIEW OF SCIENTIFIC INSTRUMENTS **80**, 12, p. 123904 (2009), URL <http://link.aip.org/link/RSINAK/v80/i12/p123904/s1&Agg=doi>
- [18] P. Yeh. *Optical waves in layered media*. John Wiley & Sons, Inc. (2005)
- [19] M. Born, E. Wolf. *Principles of Optics*. Cambridge University Press (2006)
- [20] S. Teitler, B. W. Henvis. *Refraction in Stratified, Anisotropic Media*. J. Opt. Soc. Am. **60**, p. 830 (1970), URL <http://www.opticsinfobase.org/abstract.cfm?URI=josa-60-6-830>
- [21] D. W. Berreman. *Optics in Stratified and Anisotropic Media: 4x4 Formulation*. J. Opt. Soc. Am. **62**, 4, p. 502 (1972), URL <http://www.opticsinfobase.org/abstract.cfm?URI=josa-62-4-502>
- [22] A. F. Oskooi, D. Roundy, M. Ibanescu, P. Bermel, J. D. Joannopoulos, S. G. Johnson. *MEEP: A flexible free-software package for electromagnetic simulations by the FDTD method*. Computer Physics Communications **181**, pp. 687–702 (2010), URL <http://linkinghub.elsevier.com/retrieve/pii/S001046550900383X>
- [23] A. Taflove, S. C. Hagness. *Computational Electrodynamics: The Finite-Difference Time-Domain Method*. Artech House (2005)

- [24] W. N. Hardy, L. A. Whitehead. *Split-ring resonator for use in magnetic resonance from 200-2000 MHz*. Review of Scientific Instruments **52**, p. 213 (1981), URL <http://link.aip.org/link/?RSI/52/213/1&Agg=doi>
- [25] H. J. Schneider, P. Dullenkopf. *Slotted tube resonator: A new NMR probe head at high observing frequencies*. Rev. Sci. Instrum. **48**, 1, p. 68 (1977), URL <http://link.aip.org/link/RSINAK/v48/i1/p68/s1&Agg=doi>
- [26] B. T. Ghim, G. A. Rinard, R. W. Quine, S. S. Eaton, G. R. Eaton. *Design and Fabrication of Copper-Film Loop-Gap Resonators*. Journal of Magnetic Resonance, Series A **120**, 1, pp. 72–76 (1996), URL <http://linkinghub.elsevier.com/retrieve/pii/S106418589690100X>
- [27] J. Zhou, K. Th., M. Kafesaki, E. N. Economou, J. B. Pendry, C. M. Soukoulis. *Saturation of the Magnetic Response of Split-Ring Resonators at Optical Frequencies*. Phys. Rev. Lett. **95**, p. 223902 (2005), URL <http://link.aps.org/doi/10.1103/PhysRevLett.95.223902>
- [28] D. R. Smith, W. J. Padilla, D. C. Vier, S. C. Nemat-Nasser, S. Schultz. *Composite Medium with Simultaneously Negative Permeability and Permittivity*. Phys. Rev. Lett. **84**, p. 4184 (2000), URL <http://link.aps.org/doi/10.1103/PhysRevLett.84.4184>
- [29] N. Katsarakis, T. Koschny, M. Kafesaki, E. N. Economou, C. M. Soukoulis. *Electric coupling to the magnetic resonance of split ring resonators*. Appl. Phys. Lett. **84**, p. 2943 (2004), URL <http://link.aip.org/link/APPLAB/v84/i15/p2943/s1&Agg=doi>
- [30] J. Yang, J. Hwang, T. Timusk. *Left-handed behavior of split-ring resonators: Optical measurements and numerical analysis*. Phys. Rev. B **77**, 20, p. 205114 (2008), URL <http://link.aps.org/doi/10.1103/PhysRevB.77.205114>

- [31] H. Chen, L. Ran, J. Huangfu, X. Zhang, K. Chen, T. M. Grzegorzczuk, J. A. Kong. *Left-handed materials composed of only S-shaped resonators*. Phys. Rev. E **70**, p. 057605 (2004), URL <http://link.aps.org/doi/10.1103/PhysRevE.70.057605>
- [32] S. Linden, C. Enkrich, M. Wegener, J. Zhou, T. Koschny, C. Soukoulis. *Magnetic Response of Metamaterials at 100 Terahertz*. Science **306**, p. 1351 (2004), URL <http://www.sciencemag.org/cgi/doi/10.1126/science.1105371>
- [33] M. Bayandir, K. Aydin, E. Ozbay, P. Markos, C. M. Soukoulis. *Transmission properties of composite metamaterials in free space*. Appl. Phys. Lett. **81**, p. 120 (2002), URL <http://link.aip.org/link/APPLAB/v81/i1/p120/s1&Agg=doi>
- [34] K. Aydin, I. Pryce, H. A. Atwater. *Symmetry breaking and strong coupling in planar optical metamaterials*. Optics Express **18**, 13, p. 13407 (2010), URL <http://www.opticsinfobase.org/abstract.cfm?URI=oe-18-13-13407>
- [35] R. S. Penciu, K. Aydin, M. Kafesaki, T. Koschny, E. Ozbay, E. N. Economou, C. M. Soukoulis. *Multi-gap individual and coupled split-ring resonator structures*. Optics Express **16**, 22, p. 18131 (2008), URL <http://www.opticsinfobase.org/abstract.cfm?URI=oe-16-22-18131>
- [36] I. A. I. Al-Naib, C. Jansen, M. Koch. *High Q-factor metasurfaces based on miniaturized asymmetric single split resonators*. Appl. Phys. Lett. **94**, p. 153505 (2009), URL <http://link.aip.org/link/APPLAB/v94/i15/p153505/s1&Agg=doi>
- [37] R. Singh, A. K. Azad, J. F. O'Hara, A. J. Taylor, W. Zhang. *Effect of metal permittivity on resonant properties of terahertz metamaterials*. Optics Letters **33**, 13, p. 1506 (2008), URL <http://www.opticsinfobase.org/abstract.cfm?URI=ol-33-13-1506>
- [38] C. Rockstuhl, T. Zentgraf, H. Guo, N. Liu, C. Etrich, I. Loa, K. Syassen, J. Kuhl, F. Lederer, H. Giessen. *Resonances of split-ring*

- resonator metamaterials in the near infrared*. Appl. Phys. B **84**, pp. 219–227 (2006), URL <http://www.springerlink.com/index/10.1007/s00340-006-2205-2>
- [39] C. Enkrich, F. Pérez-Willard, D. Gerthsen, J. Zhou, T. Koschny, C. M. Soukoulis, M. Wegener, S. Linden. *Focused-Ion-Beam Nanofabrication of Near-Infrared Magnetic Metamaterials*. Advanced Materials **17**, p. 2547 (2005), URL <http://doi.wiley.com/10.1002/adma.200500804>
- [40] C. Rockstuhl, F. Lederer, C. Etrich, T. Zentgraf, J. Kuhl, H. Giessen. *On the reinterpretation of resonances in split-ring-resonators at normal incidence*. Opt. Express **14**, 19, p. 8827 (2006), URL <http://www.opticsinfobase.org/abstract.cfm?URI=oe-14-19-8827>
- [41] J. W. Nilsson, S. A. Riedel. *Electric Circuits*. Prentice Hall (2011)
- [42] W. F. J. Brown, R. M. Hornreich, S. Shtrikman. *Upper Bound on the Magnetoelectric Susceptibility*. Physical Review **168**, 2, p. 574 (1968), URL <http://link.aps.org/doi/10.1103/PhysRev.168.574>
- [43] P. Gay-Balmaz, O. J. F. Martin. *Electromagnetic resonances in individual and coupled split-ring resonators*. Journal of Applied Physics **92**, 5, p. 2929 (2002), URL <http://link.aip.org/link/JAPIAU/v92/i5/p2929/s1&Agg=doi>
- [44] N. Katsarakis, G. Konstantinidis, A. Kostopoulos, R. S. Penciu, T. F. Gundogdu, M. Kafesaki, E. N. Economou, T. Koschny, C. M. Soukoulis. *Magnetic response of split-ring resonators in the far-infrared frequency regime*. Optics Letters **30**, 11, p. 1348 (2005), URL <http://www.opticsinfobase.org/abstract.cfm?URI=ol-30-11-1348>
- [45] C. R. Simovski, S. A. Tretyakov. *Local constitutive parameters of metamaterials from an effective-medium perspective*. Physical Review B **75**, p. 195111 (2007), URL <http://link.aps.org/doi/10.1103/PhysRevB.75.195111>

- [46] T. Koschny, P. Markos, D. R. Smith, C. M. Soukoulis. *Resonant and antiresonant frequency dependence of the effective parameters of metamaterials*. Phys. Rev. E **68**, p. 065602 (2003), URL <http://link.aps.org/doi/10.1103/PhysRevE.68.065602>
- [47] C. Caloz, A. Lai, T. Itoh. *The challenge of homogenization in metamaterials*. New journal of Physics **7**, p. 167 (2005), URL <http://stacks.iop.org/1367-2630/7/i=1/a=167?key=crossref.80a7b46fcbb5c5fc2a27b207d3f93844>
- [48] D. R. Smith, J. B. Pendry. *Homogenization of metamaterials by field averaging*. J. Opt. Soc. Am. B **23**, 3, p. 391 (2006), URL <http://www.opticsinfobase.org/abstract.cfm?URI=JOSAB-23-3-391>
- [49] M. G. Silveirinha, C. A. Fernandes. *Transverse-average field approach for the characterization of thin metamaterial slabs*. Physical Review E **75**, p. 036613 (2007), URL <http://link.aps.org/doi/10.1103/PhysRevE.75.036613>
- [50] R. Liu, T. J. Cui, D. Huang, B. Zhao, D. R. Smith. *Description and explanation of electromagnetic behaviors in artificial metamaterials based on effective medium theory*. Physical Review E **76**, p. 026606 (2007), URL <http://link.aps.org/doi/10.1103/PhysRevE.76.026606>
- [51] C. R. Simovski. *Material Parameters of Metamaterials (a Review)*. Optics and Spectroscopy **107**, 5, p. 726 (2009), URL <http://www.springerlink.com/index/10.1134/S0030400X09110101>
- [52] C. R. Simovski. *On electromagnetic characterization and homogenization of nanostructured metamaterials*. Journal of Optics **13**, p. 013001 (2011), URL <http://stacks.iop.org/2040-8986/13/i=1/a=013001?key=crossref.7321766a6630b917c6f066f2abc1e2cc>
- [53] D. Morits, C. Simovski. *Electromagnetic characterization of planar and bulk metamaterials: A theoretical study*. Physical Review B **82**, p. 165114 (2010), URL <http://link.aps.org/doi/10.1103/PhysRevB.82.165114>

- [54] C. Menzel, T. Paul, C. Rockstuhl, T. Pertsch, S. Tretyakov, F. Lederer. *Validity of effective material parameters for optical fishnet metamaterials*. Phys. Rev. B **81**, p. 035320 (2010), URL <http://link.aps.org/doi/10.1103/PhysRevB.81.035320>
- [55] T. Paul, C. Menzel, W. Śmigaj, C. Rockstuhl, P. Lalanne, F. Lederer. *Reflection and transmission of light at periodic layered metamaterial films*. Phys. Rev. B **84**, p. 115142 (2011), URL <http://link.aps.org/doi/10.1103/PhysRevB.84.115142>
- [56] A. Alù. *Restoring the physical meaning of metamaterial constitutive parameters*. Phys. Rev. B **83**, p. 081102 (2011), URL <http://link.aps.org/doi/10.1103/PhysRevB.83.081102>
- [57] A. V. Kildishev, J. D. Borneman, X. Ni, V. M. ShalaeV, V. P. Drachev. *Bianisotropic Effective Parameters of Optical Metamagnetics and Negative-Index Materials*. Proceedings of the IEEE **99**, 10, p. 1691 (2011), URL <http://ieeexplore.ieee.org/lpdocs/epic03/wrapper.htm?arnumber=5982077>
- [58] M. Albooyeh, D. Morits, C. Simovski. *Electromagnetic characterization of substrated metasurfaces*. Metamaterials **5**, 4, pp. 178 – 205. ISSN 1873-1988 (2011), URL <http://www.sciencedirect.com/science/article/pii/S1873198811000296>
- [59] A. Andryieuski, C. Menzel, C. Rockstuhl, R. Malureanu, F. Lederer, A. Lavrinenko. *Homogenization of resonant chiral metamaterials*. Phys. Rev. B **82**, p. 235107 (2010), URL <http://link.aps.org/doi/10.1103/PhysRevB.82.235107>
- [60] C. Menzel, C. Rockstuhl, T. Paul, F. Lederer. *Retrieving effective parameters for quasiplanar chiral metamaterials*. Appl. Phys. Lett. **93**, p. 233106 (2008), URL <http://link.aip.org/link/APPLAB/v93/i23/p233106/s1&Agg=doi>
- [61] E. F. Kuester, M. A. Mohamed, M. Piket-May, c. L. Holloway. *Averaged Transition Conditions for Electromagnetic Fields at a*

- Metafilm*. IEEE Transactions on Antennas and Propagation **51**, 10, p. 2641 (2003), URL <http://ieeexplore.ieee.org/lpdocs/epic03/wrapper.htm?arnumber=1236082>
- [62] C. L. Holloway, A. Dienstfrey, E. F. Kuester, J. F. O'Hara, A. K. Azad, A. J. Taylor. *A discussion on the interpretation and characterization of metafilms/metasurfaces: The two-dimensional equivalent of metamaterials*. Metamaterials **3**, pp. 100–112 (2009), URL <http://linkinghub.elsevier.com/retrieve/pii/S1873198809000231>
- [63] C. L. Holloway, E. Kuester, A. Dienstfrey. *Characterizing Metasurfaces/Metafilms: The Connection Between Surface Susceptibilities and Effective Material Properties*. IEEE Antennas and Wireless Propagation Letters **10**, p. 1507 (2011), URL <http://ieeexplore.ieee.org/lpdocs/epic03/wrapper.htm?arnumber=6121930>
- [64] A. M. Shuvaev, S. Engelbrecht, M. Wunderlich, A. Schneider, A. Pimenov. *Strong dynamic magnetoelectric coupling in metamaterial*. Eur. Phys. J. B **79**, pp. 163–167 (2011), URL <http://www.springerlink.com/index/10.1140/epjb/e2010-10493-1>
- [65] M. Dressel, G. Grüner. *Electrodynamics of Solids: Optical Properties of Electrons in Matter*. Cambridge University Press, Cambridge, 1st edition (2002)
- [66] E. Plum, V. A. Fedotov, N. I. Zheludev. *Optical activity in extrinsically chiral metamaterial*. Appl. Phys. Lett. **93**, p. 191911 (2008), URL <http://link.aip.org/link/APPLAB/v93/i19/p191911/s1&Agg=doi>
- [67] E. Plum, X.-X. Liu, V. A. Fedotov, Y. Chen, D. P. Tsai, N. I. Zheludev. *Metamaterials: optical activity without chirality*. Phys. Rev. Lett. **102**, p. 113902 (2009), URL <http://link.aps.org/doi/10.1103/PhysRevLett.102.113902>

- [68] K. Aydin, I. Bulu, K. Guven, M. Kafesaki, C. M. Soukoulis, E. Ozbay. *Investigation of magnetic resonances for different split-ring resonator parameters and designs*. New J. Phys. **7**, p. 168 (2005), URL <http://stacks.iop.org/1367-2630/7/i=1/a=168?key=crossref.92f45dc0189440130b66bde8cca4a02a>
- [69] R. Singh, E. Smirnova, A. J. Taylor, J. F. O'Hara, W. Zhang. *Optically thin terahertz metamaterials*. Optics Express **16**, 9, p. 6537 (2008), URL <http://www.opticsinfobase.org/abstract.cfm?URI=oe-16-9-6537>
- [70] I. Sersic, M. Frimmer, E. Verhagen, A. Femius Koenderink. *Electric and Magnetic Dipole Coupling in Near-Infrared Split-Ring Metamaterial Arrays*. Phys. Rev. Lett. **103**, p. 213902 (2009), URL <http://link.aps.org/doi/10.1103/PhysRevLett.103.213902>
- [71] F. Terman. *Radio engineer's handbook*. McGraw-Hill Book Company (1943)
- [72] R. Singh, C. Rockstuhl, W. Zhang. *Strong influence of packing density in terahertz metamaterials*. Applied Physics Letters **97**, p. 241108 (2010), URL <http://link.aip.org/link/APPLAB/v97/i24/p241108/s1&Agg=doi>
- [73] R. Singh, C. Rockstuhl, F. Lederer, W. Zhang. *The impact of nearest neighbor interaction on the resonances in terahertz metamaterials*. Applied Physics Letters **94**, p. 021116 (2009), URL <http://link.aip.org/link/APPLAB/v94/i2/p021116/s1&Agg=doi>
- [74] R. Singh, A. K. Azad, Q. X. Jia, A. J. Taylor, H.-T. Chen. *Thermal tunability in terahertz metamaterials fabricated on strontium titanate single crystal substrates*. Optics Letters **36**, 7, pp. 1230–1232 (2011), URL <http://www.opticsinfobase.org/abstract.cfm?URI=ol-36-7-1230>
- [75] J.-M. Manceau, N.-H. Shen, M. Kafesaki, C. M. Soukoulis, S. Tzortzakis. *Dynamic response of metamaterials in the terahertz*

- regime: Blueshift tunability and broadband phase modulation.* Applied Physics Letters **96**, p. 021111 (2010), URL <http://link.aip.org/link/APPLAB/v96/i2/p021111/s1&Agg=doi>
- [76] W. Rechberger, A. Hohenau, A. Leitner, J. R. Krenn, B. Lamprecht, F. R. Aussenegg. *Optical properties of two interacting gold nanoparticles.* Optics C **220**, p. 137 (2003), URL <http://linkinghub.elsevier.com/retrieve/pii/S0030401803013579>
- [77] R. Singh, Z. Tian, J. Han, C. Rockstuhl, J. Gu, W. Zhang. *Cryogenic temperatures as a path toward high-Q terahertz metamaterials.* Applied Physics Letters **96**, p. 071114 (2010), URL <http://link.aip.org/link/APPLAB/v96/i7/p071114/s1&Agg=doi>
- [78] J. Gu, R. Singh, Z. Tian, W. Cao, M. He, J. W. Zhang, J. Han, H.-T. Chen, W. Zhang. *Terahertz superconductor metamaterial.* Applied Physics Letters **97**, p. 071102 (2010), URL <http://link.aip.org/link/APPLAB/v97/i7/p071102/s1&Agg=doi>
- [79] I. Wilke, M. Khazan, C. T. Rieck, P. Kuzel, T. Kaiser, C. Jaekel, H. Kurz. *Terahertz surface resistance of high temperature superconducting thin films.* Journal of Applied Physics **87**, 6, p. 2984 (2000), URL <http://link.aip.org/link/JAPIAU/v87/i6/p2984/s1&Agg=doi>
- [80] M. Ricci, N. Orloff, S. M. Anlage. *Superconducting metamaterials.* Appl. Phys. Lett. **87**, p. 034102 (2005), URL <http://link.aip.org/link/APPLAB/v87/i3/p034102/s1&Agg=doi>
- [81] M. C. Ricci, H. Xu, R. Prozorov, A. P. Zhuravel, A. V. Ustinov, S. M. Anlage. *Tunability of Superconducting Metamaterials.* IEEE TRANSACTIONS ON APPLIED SUPERCONDUCTIVITY **17**, 2, pp. 918–921 (2007), URL <http://ieeexplore.ieee.org/lpdocs/epic03/wrapper.htm?arnumber=4277675>
- [82] H.-T. Chen, W. J. Padilla, J. M. O. Zide, A. C. Gossard, T. A. J., R. D. Averitt. *Active terahertz metamaterial devices.* Nature **444**, pp.

- 597–600 (2006), URL <http://www.nature.com/doi/10.1038/nature05343>
- [83] W. J. Padilla, D. N. Basov, D. R. Smith. *Negative refractive index metamaterials*. *Materials Today* **9**, 7-8, p. 28 (2006)
- [84] H.-T. Chen, J. F. O'Hara, A. K. Azad, A. J. Taylor, R. D. Averitt, D. B. Shrekenhamer, W. J. Padilla. *Experimental demonstration of frequency-agile terahertz metamaterials*. *Nature Photonics* **2**, 5, pp. 295–298 (2008), URL <http://www.nature.com/doi/10.1038/nphoton.2008.52>
- [85] T. Driscoll, S. Palit, M. M. Quazilbash, M. Brehm, F. Keilmann, B.-G. Chae, S.-J. Yun, H.-T. Kim, S. Y. Cho, N. M. Jokerst, D. R. Smith, D. N. Basov. *Dynamic tuning of an infrared hybrid-metamaterial resonance using vanadium dioxide*. *Appl. Phys. Lett.* **93**, p. 024101 (2008), URL <http://link.aip.org/link/APPLAB/v93/i2/p024101/s1&Agg=doi>
- [86] A. V. Pronin, M. Dressel, A. Pimenov, A. Loidl, I. V. Roshchin, L. H. Greene. *Direct observation of the superconducting energy gap developing in the conductivity spectra of niobium*. *Phys. Rev. B* **57**, p. 14416 (1998), URL <http://link.aps.org/doi/10.1103/PhysRevB.57.14416>
- [87] L. H. Greene, J. F. Dorsten, I. V. Roshcin, A. C. Abeyta, T. A. Tanzer, G. Kuchler, W. L. Feldmann, P. W. Bohn. *Raman scattering as a probe of the superconducting proximity effect*. *Czech. J. Phys.* **46**, p. 3115 (1996), URL <http://link.springer.com/10.1007/BF02548118>
- [88] C. Peroz, C. Villard. *Flux flow properties of niobium thin films in clean and dirty superconducting limits*. *Phys. Rev. B* **72**, p. 014515 (2005), URL <http://link.aps.org/doi/10.1103/PhysRevB.72.014515>
- [89] M. W. Coffey, J. R. Clem. *Unified theory of effects of vortex pinning and flux creep upon the rf surface impedance of type-II*

- superconductors*. Phys. Rev. Lett. **67**, 3, pp. 386–389 (1991), URL <http://link.aps.org/doi/10.1103/PhysRevLett.67.386>
- [90] V. A. Fedotov, M. Rose, S. L. Prosvirnin, N. Papasimakis, N. I. Zheludev. *Sharp Trapped-Mode Resonances in Planar metamaterials with a Broken Structural Symmetry*. Physical Review Letters **99**, p. 147401 (2007), URL <http://link.aps.org/doi/10.1103/PhysRevLett.99.147401>
- [91] V. A. Fedotov, A. Tsiatmas, J. H. Shi, R. Buckingham, P. de Groot, Y. Chen, S. Wang, N. I. Zheludev. *Temperature control of Fano resonances and transmission in superconducting metamaterials*. Optics Express **18**, 9, p. 9015 (2010), URL <http://www.opticsinfobase.org/abstract.cfm?URI=oe-18-9-9015>
- [92] Y. Svirko, N. Zheludev, M. Osipov. *Layered chiral metallic microstructures with inductive coupling*. Appl. Phys. Lett. **78**, p. 498 (2001), URL <http://link.aip.org/link/APPLAB/v78/i4/p498/s1&Agg=doi>
- [93] N. Kanda, K. Konishi, M. Kuwata-Gonokami. *Terahertz wave polarization rotation with double layered metal grating of complimentary chiral patterns*. Opt. Express **15**, 18, p. 11117 (2007), URL <http://www.opticsinfobase.org/abstract.cfm?URI=oe-15-18-11117>
- [94] E. Plum, V. A. Fedotov, A. S. Schwanecke, N. I. Zheludev, Y. Chen. *Giant optical gyrotropy due to electromagnetic coupling*. Appl. Phys. Lett. **90**, p. 223113 (2007), URL <http://link.aip.org/link/APPLAB/v90/i22/p223113/s1&Agg=doi>
- [95] S. Tretyakov, A. Serdyukov, I. Semchenko, A. Sihvola. *Waves and energy in chiral nihility*. J. Electromagn. Waves Appl. **17**, pp. 695–706 (2003), URL <http://www.tandfonline.com/doi/abs/10.1163/156939303322226356>
- [96] C. Zhang, T. J. Cui. *Negative reflections of electromagnetic waves in*

- a strong chiral medium*. Appl. Phys. Lett. **91**, p. 194101 (2007), URL <http://link.aip.org/link/APPLAB/v91/i19/p194101/s1&Agg=doi>
- [97] B. Wang, J. Zhou, T. Koschny, C. M. Soukoulis. *Nonplanar chiral metamaterials with negative index*. Appl. Phys. Lett. **94**, p. 151112 (2009), URL <http://link.aip.org/link/APPLAB/v94/i15/p151112/s1&Agg=doi>
- [98] E. Plum, J. Zhou, J. Dong, V. A. Fedotov, T. Koschny, C. M. Soukoulis, N. I. Zheludev. *Metamaterial with negative index due to chirality*. Phys. Rev. B **79**, p. 035407 (2009), URL <http://link.aps.org/doi/10.1103/PhysRevB.79.035407>
- [99] J. Zhou, J. Dong, B. Wang, T. Koschny, M. Kafesaki, C. M. Soukoulis. *Negative refractive index due to chirality*. Phys. Rev. B **79**, p. 121104 (2009), URL <http://link.aps.org/doi/10.1103/PhysRevB.79.121104>
- [100] S. Zhang, Y.-S. Park, J. Li, X. Lu, W. Zhang, X. Zhang. *Negative Refractive Index in Chiral metamaterials*. Phys. Rev. Lett. **102**, p. 023901 (2009), URL <http://link.aps.org/doi/10.1103/PhysRevLett.102.023901>
- [101] B. Wang, J. Zhou, T. Koschny, M. Kafesaki, C. M. Soukoulis. *Chiral metamaterials: simulations and experiments*. J. Opt. A **11**, p. 114003 (2009), URL <http://stacks.iop.org/1464-4258/11/i=11/a=114003?key=crossref.239de0a78b75b5ef7d95601682387048>
- [102] M. Decker, M. W. Klein, M. Megener, S. Linden. *Circular dichroism of planar chiral magnetic metamaterials*. Optics Letters **32**, p. 856 (2007), URL <http://www.opticsinfobase.org/abstract.cfm?URI=ol-32-7-856>
- [103] J. K. Gansel, M. Thiel, M. S. Rill, M. Decker, K. Bade, V. Saile, G. von Freymann, S. Linden, M. Wegener. *Gold Helix Photonic Metamaterial as Broadband Circular Polarizer*. Science **325**, p. 1513 (2009), URL <http://www.sciencemag.org/cgi/doi/10.1126/science.1177031>

- [104] T. Li, H. Liu, T. Li, S. M. Wang, F. M. Wang, R. X. Wu, P. Chen, S. N. Zhu, X. Zhang. *Magnetic resonance hybridization and optical activity of microwaves in a chiral metamaterial*. Appl. Phys. Lett. **92**, p. 131111 (2008), URL <http://link.aip.org/link/APPLAB/v92/i13/p131111/s1&Agg=doi>
- [105] H. Liu, D. A. Genov, D. M. Wu, Y. M. Liu, Z. W. Liu, C. Sun, S. N. Zhu, X. Zhang. *Magnetic plasmon hybridization and optical activity at optical frequencies in metallic nanostructures*. Phys. Rev. B **76**, p. 073101 (2007), URL <http://link.aps.org/doi/10.1103/PhysRevB.76.073101>
- [106] N. Liu, H. Liu, S. Zhu, H. Giessen. *Stereometamaterials*. Nature Photon. **3**, p. 157 (2009), URL <http://www.nature.com/doifinder/10.1038/nphoton.2009.4>
- [107] X. Xiong, W.-H. Sun, Y.-J. Bao, R.-W. Peng, M. Wang, C. Sun, X. Lu, J. Shao, Z.-F. Li, N.-B. Ming. *Switching the electric and magnetic responses in a metamaterial*. Phys. Rev. B **80**, p. 201105(R) (2009), URL <http://link.aps.org/doi/10.1103/PhysRevB.80.201105>
- [108] X. Xiong, W.-H. Sun, Y.-J. Bao, M. Wang, R.-W. Peng, C. Sun, X. Lu, J. Shao, Z.-F. Li, N.-B. Ming. *Construction of a chiral metamaterial with a U-shaped resonator assembly*. Phys. Rev. B **81**, p. 075119 (2010), URL <http://link.aps.org/doi/10.1103/PhysRevB.81.075119>
- [109] M. Decker, R. Zhao, C. M. Soukoulis, S. Linden, M. Wegener. *Twisted split-ring-resonator photonic metamaterial with huge optical activity*. Optics Letters **35**, 10, pp. 1593–1595 (2010), URL <http://www.opticsinfobase.org/abstract.cfm?URI=ol-35-10-1593>
- [110] J. A. Kong. *Electromagnetic Wave Theory*. John Wiley & Sons (1986)
- [111] K. Finkenzeller. *RFID Handbook: Fundamentals and Applications in Contactless Smart Cards, Radio Frequency Identification and Near-Field Communication, Third Edition*. Wiley (2010)

-
- [112] R. Menzel. *Photonics: Linear and Nonlinear Interactions of Laser Light and Matter*. Springer (2001)
- [113] A. S. Barker, J. J. Hopfield. *Coupled-Optical-Phonon-Mode Theory of the Infrared Dispersion in BaTiO₃, SrTiO₃, and KTaO₃*. Phys. Rev. **135**, 6A, p. A1732 (1964), URL <http://link.aps.org/doi/10.1103/PhysRev.135.A1732>
- [114] M. Fleischhauer, A. Imamoglu, J. P. Marangos. *Electromagnetically induced transparency: Optics in coherent media*. Reviews of Modern Physics **77**, 2, p. 633 (2005), URL <http://link.aps.org/doi/10.1103/RevModPhys.77.633>
- [115] N. Papasimakis, V. A. Fedotov, N. I. Zheludev, S. L. Prosvirnin. *Metamaterial Analog of Electromagnetically Induced Transparency*. Phys. Rev. Lett. **101**, p. 253903 (2008), URL <http://link.aps.org/doi/10.1103/PhysRevLett.101.253903>
- [116] J. D. Jackson. *Classical Electrodynamics*. Wiley (1998)

Curriculum Vitae

Personal details

Name: Dipl.-Phys. Sebastian Engelbrecht
Adress: Greinergasse 22-24/3/4, 1190 Wien
Date of birth: June 6, 1983
Place of birth: Schweinfurt, Germany
Nationality: German
Marital status: single

Education

1990 – 1994 St. Hedwig Grundschule, Kitzingen, Germany
1994 – 2003 Egbert-Gymnasium, Münsterschwarzach, Germany
2003 – 2008 Diploma study in physics,
Julius-Maximilians-Universität Würzburg, Germany
topic of Diploma thesis: *Untersuchung der
elektronischen Struktur von Ferromagnet-
Halbleiter-Hybridsystemen mittels
Photoelektronenspektroskopie*
Supervisor: Prof. Dr. Ralph Claessen
2008 – 2010 Ph.D. student at the Physikalisches Institut,
Julius-Maximilians-Universität Würzburg, Germany
Supervisor: Prof. Dr. Andrei Pimenov
2011 – 2013 Ph.D. student at the institute of solid state physics,
Vienna University of Technology
Supervisor: Prof. Dr. Andrei Pimenov

List of own publications

1. A. Schneider, A. Shuvaev, S. Engelbrecht, S. O. Demokritov and A. Pimenov, Electrically Excited Inverse Electron Spin Resonance in a Split-Ring Metamaterial Resonator, *Phys. Rev. Lett.* **103**, 103907 (2009)
2. S. Engelbrecht, M. Wunderlich, A. M. Shuvaev and A. Pimenov, Colossal optical activity of split-ring resonator arrays for millimeter waves, *Appl. Phys. Lett.* **97**, 081116 (2010)
3. Biaobing Jin, Caihong Zhang, Sebastian Engelbrecht, Andrei Pimenov, Jingbo Wu, Qinyin Xu, Chunhai Cao, Jian Chen, Weiwei Xu, Lin Kang and Peiheng Wu, Low loss and magnetic field-tunable superconducting terahertz metamaterial, *Opt. Exp.* **18**, 17504 (2010)
4. A. M. Shuvaev, S. Engelbrecht, M. Wunderlich, A. Schneider and A. Pimenov, Strong dynamic magnetoelectric coupling in metamaterial, *Eur. Phys. J. B* **79**, 163-167 (2011)
5. S. Engelbrecht, A. M. Shuvaev, Y. Luo, V. Moshnyaga and A. Pimenov, Negative refraction in natural ferromagnetic metals, *Eur. Phys. Lett.* **95**, 37005 (2011)
6. S. Engelbrecht, A. M. Shuvaev, Ch. Kant, K. Unterrainer and A. Pimenov, Experimental determination of effective parameters in a layered metamaterial, *Phys. Rev. B* **85**, 235437 (2012)